



# รายงานวิจัยฉบับสมบูรณ์

**โครงการ** ปฏิกิริยาขจัดน้ำของเอทานอลเป็นเอทิลีนบนตัวเร่งปฏิกิริยากรดของแข็ง

Dehydration of ethanol to ethylene over solid acid catalysts

โดย

ศาสตราจารย์ คร. บรรเจิค จงสมจิตร

# รายงานวิจัยฉบับสมบูรณ์

**โครงการ** ปฏิกิริยาขจัดน้ำของเอทานอลเป็นเอทิลีนบนตัวเร่งปฏิกิริยากรคของแข็ง

Dehydration of ethanol to ethylene over solid acid catalysts

# ผู้วิจัย

ศาสตราจารย์ คร. บรรเจิค จงสมจิตร

ภาควิชาวิศวกรรมเคมี คณะวิศวกรรมศาสตร์

จุฬาลงกรณ์มหาวิทยาลัย

สนับสนุนโดยสำนักงานกองทุนสนับสนุนการวิจัยและจุฬาลงกรณ์มหาวิทยาลัย

(ความเห็นในรายงานนี้เป็นของผู้วิจัย สกว.และจุฬาลงกรณ์มหาวิทยาลัยไม่จำเป็นต้องเห็นด้วยเสมอไป)



Article

# **Desorption of Water from Distinct Step Types on a Curved Silver Crystal**

Jakrapan Janlamool <sup>1,2</sup>, Dima Bashlakov <sup>2</sup>, Otto Berg <sup>2</sup>, Piyasan Praserthdam <sup>1</sup>, Bunjerd Jongsomjit <sup>1</sup> and Ludo B. F. Juurlink <sup>2,\*</sup>

- <sup>1</sup> Center of Excellence on Catalysis and Catalytic Reaction Engineering, Department of Chemical Engineering, Faculty of Engineering, Chulalongkorn University, Bangkok 10330, Thailand
- <sup>2</sup> Leiden Institute of Chemistry, Leiden University, PO BOX 9502, 2300 RA Leiden, The Netherlands
- \* Author to whom correspondence should be addressed; E-Mail: l.juurlink@chem.leidenuniv.nl; Tel.: +31-71-527-421.

Received: 24 March 2014; in revised form: 28 May 2014 / Accepted: 30 June 2014 /

Published: 25 July 2014

**Abstract:** We have investigated the adsorption of  $H_2O$  onto the A and B type steps on an Ag single crystal by temperature programmed desorption. For this study, we have used a curved crystal exposing a continuous range of surface structures ranging from  $[5(111) \times (100)]$  via (111) to  $[5(111) \times (110)]$ . LEED and STM studies verify that the curvature of our sample results predominantly from monoatomic steps. The sample thus provides a continuous array of step densities for both step types. Desorption probed by spatially-resolved TPD of multilayers of  $H_2O$  shows no dependence on the exact substrate structure and thus confirms the absence of thermal gradients during temperature ramps. In the submonolayer regime, we observe a small and linear dependence of the desorption temperature on the A and B step density. We argue that such small differences are only observable by means of a single curved crystal, which thus establishes new experimental benchmarks for theoretical calculation of chemically accurate binding energies. We propose an origin of the observed behavior based on a "two state" desorption model.

Keywords: silver; water; adsorption; single crystal; steps; surface science

#### 1. Introduction

The kinetics of many heterogeneously catalyzed reactions depend strongly on the structure and size of transition metal particles [1]. In recent years, theoretical studies have begun to unravel the origin of such structure sensitivity [2,3]. Particle size dependence often stems from the occurrence of particular arrangements of surface atoms. These clusters critically lower the activation barrier for dissociation of a small molecule or the assembly of an intermediate from surface-bound species. Amongst others, ammonia synthesis over Ru and methanol synthesis over Cu/ZnO have been shown to depend on particular configurations of atoms at monoatomic steps occurring at the surface of catalyst particles [4,5].

Besides using grown [6] or deposited (e.g., [7,8]) catalytic particles on metal oxide substrates, fundamental experimental investigations of heterogeneous catalysis often employ flat, well polished, single crystal metal surfaces. On low Miller index surfaces, the coordination number of surface atoms is maximized. To investigate the influence of surface sites with lower coordination, defects can be added either by choosing a high Miller index surface plane, by intentionally sputtering the surface without subsequent annealing, or by adding fresh but incomplete metal layers, e.g., by vapor deposition. On the other hand, it was recognized several decades ago that curved single crystal samples may provide benefits to experimental studies probing chemical and physical phenomena that depend on surface structure [9-15]. The presence of a range of locally uniform steps and kinks on a single sample circumvents common sources of sample-to-sample heterogeneity, such as different levels of contamination or differences in the accuracy of temperature measurement. Also, it simplifies experimental procedures as the breaking of vacuum or repetitive loading of samples is reduced to an absolute minimum. Nonetheless, the total number of studies employing partially curved or fully cylindrical single crystals in surface science and catalysis remains very low. We expect that this is due, at least in part, to new experimental challenges: limited ability to map the exact surface structure, limited spatial resolution of various surface science probes, metallurgical reconstructions and step bunching which relax local surface energy, difficulties growing large single crystal metal boules, and the lack of polishing techniques that yield a finish comparable to flat single crystal surfaces.

Recently, interest in curved samples for physical and chemical studies probing structure sensitivity has revived [16–18]. Using Scanning Tunneling Microscopy (STM) and Angle-Resolved Photoemission Spectroscopy (ARPES), Ortega and co-workers showed that faceting and step bunching were present on a curved Au sample at particular angles close to the (111) plane [19], but not present on similar Ag and Cu samples. The stepped lattice was found to be more unstable for Cu than for Ag [20]. We recently employed a cylindrical Ni single crystal, together with supersonic molecular beam techniques, to map the reactivity dependence toward hydrogen dissociation of various step densities, step and terraces types, and for a wide range of impact energies [16]. Low energy electron diffraction (LEED) studies of our Ni sample suggest that monoatomic steps cover a large part of the circumference of the cylinder [21]. Sykes and Gellman recently began to employ a series of dome shaped Cu single crystals for STM [17,22] and were able to relate surface structure to oxidation kinetics by means of Auger Electron Spectroscopy (AES) [17].

Here, we employ a curved Ag single crystal that was prepared by a new polishing technique to investigate the surface structure dependence of water adsorption/desorption. Details about the structure and preparation of this sample can be found in the experimental section. For hydrophilic metals and

low Miller index surfaces, the sizeable literature available on the H<sub>2</sub>O-surface interaction has been reviewed in great detail [23–25]. Fewer studies have focused on stepped and hydrophobic surfaces. In recent studies, steps have been shown to exert unexpected influences on water adsorption. For example, we and others have found that water preferentially decorates Pt step sites prior to wetting terraces [26,27]. The most common step types separating (111) terraces, *i.e.*, the A or (100) and B or (110) step types, have now been shown to have different binding energies for H<sub>2</sub>O [28]. They also differ in their tendency to form OH in coadsorption with oxygen [29] and have different behavior in coadsorption with H (or D) atoms [27]. Whereas coadsorption with hydrogen in the presence of the B step type is not very different from the (111) terrace, the A step type induces hydrophobicity and reduced H-D exchange reactivity for fully hydrogenated Pt surfaces. This behavior remains unaltered over a (111) terrace length variation of four to eight atoms [30].

A clear influence of step structure may be expected when there is a small energetic difference between the adsorbate-surface and adsorbate-adsorbate interaction. In these cases, the exact atomic structure of the substrate may just "tip the scale". For hydrophobic metal surfaces, this influence of steps may be expected to be smaller. Zeroth-order desorption kinetics from Ag(111) and Ag(100) observed by Klaua and Madey led to the conclusion that these surfaces are hydrophobic [31]. They found a desorption enthalpy near the sublimation energy of ice and attributed it to a weakened H<sub>2</sub>O-metal interaction compared with, e.g., Pt [31,32]. As Ag is in general a rather non-reactive metal, potential influences of low-level contamination of oxygen—which may influence water structures significantly [33,34]—are also easily avoided. A study of water adsorption on a curved Ag sample therefore tests our ability to measure small differences in the binding of molecules to different surface structures. In the present study, we first characterize the step density as a function of cylindrical azimuth; we then show that the binding energy difference of (111) terraces interrupted by A vs. B step sites is indeed very small, but observable when using a curved single crystal sample. Finally, we consider a possible origin for the small shift in peak desorption temperature observed in spatially-resolved temperature programmed desorption (TPD) studies at submonolayer coverages.

#### 2. Results and Discussion

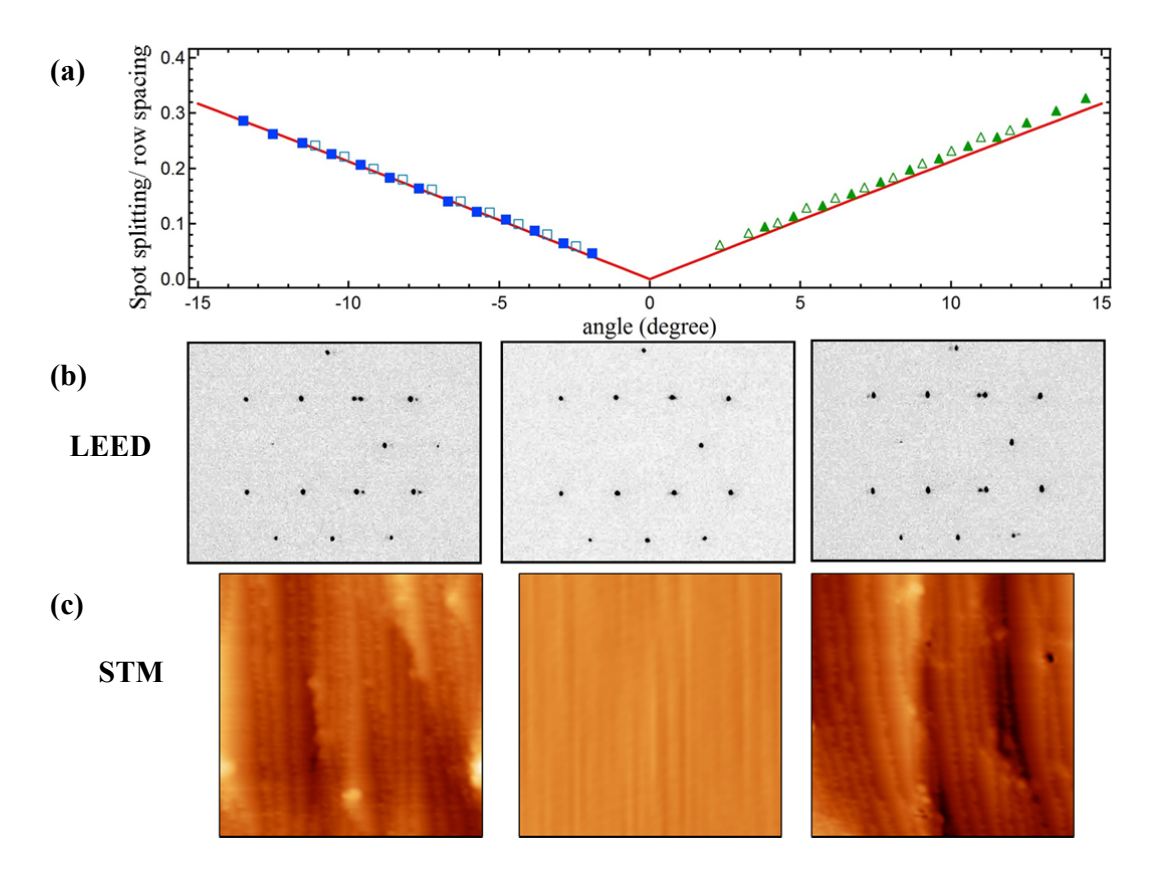
Figure 1 summarizes results from LEED and STM studies. Figure 1a shows the spot-splitting/row-spacing ratio as a function of azimuthal position from LEED patterns that were recorded while translating the crystal normal to the impacting electron beam. We simultaneously adjust the crystal's position to maintain a constant LEED-to-sample distance. Figure 1b shows representative LEED patterns. As explained by Henzler [35], diffraction from the stepped structure peaks at regularly spaced angles,  $\Delta \varphi$ , depending only on the terrace width (Na + g) and the step height (d) (see also graphical illustration in the Experimental section:

$$\Delta \varphi = \lambda / [(Na + g)\cos\varphi - d\sin\varphi]$$
 (1)

For the same number of terrace atoms, N, the spot-splitting/row-spacing ratio for the A type step (at negative angles) is slightly smaller than for the B type step (at positive angles). The difference is a consequence of the different value of the horizontal offset (g) between the exposed Ag lattice of successive terraces. The ratio has been calculated for a large number of stepped structures with integer

N terrace atoms by van Hove and Somorjai, who also suggested the [N(terrace type) × (step type)] nomenclature [36]. When expressed in terms of angular position on a cylindrical crystal, their tabulated values (for structures that are exposed on our Ag crystal) are a linear function of azimuthal angle. In Figure 1a we plot this function (solid red lines) as described in our studies of a cylindrical Ni single crystal [21] together with two data sets of the experimentally determined ratio (solid and open symbols). The coincidence of the experimental data with predictions of the Henzler model indicates that our curved surface yields the expected average local step density at any position away from the (111) center. Furthermore, as explained in detail in ref [21], one can also verify that steps are truly monoatomic by determining the electron energies at which the (0,0) beam shows singlets and doublets. We have performed this analysis at various azimuthal positions and find that the curvature of the crystal can only be explained by the predominance of monoatomic steps. The same conclusion was drawn by Ortega and coworkers for their very similar curved Ag single crystal [18].

**Figure 1.** (a) Spot-splitting/row-spacing ratio as a function of azimuthal angle; open *vs.* closed symbols represent two data sets collected on different days, red solid lines indicate expected values; (b) Images of color-inverted LEED patterns taken at  $-1.5 \text{ mm } (-5.7^{\circ}, \text{ left})$ , 0.00 mm (0°, middle), and +1.5 mm (+5.7°, right) from the crystal center; (c) STM images (50 × 50 nm²) taken at  $-1.6 \text{ mm } (-6.1^{\circ}, \text{ left})$ , 0.00 mm (0°, middle), and +1.6 mm (+6.1°, right) from the crystal center.

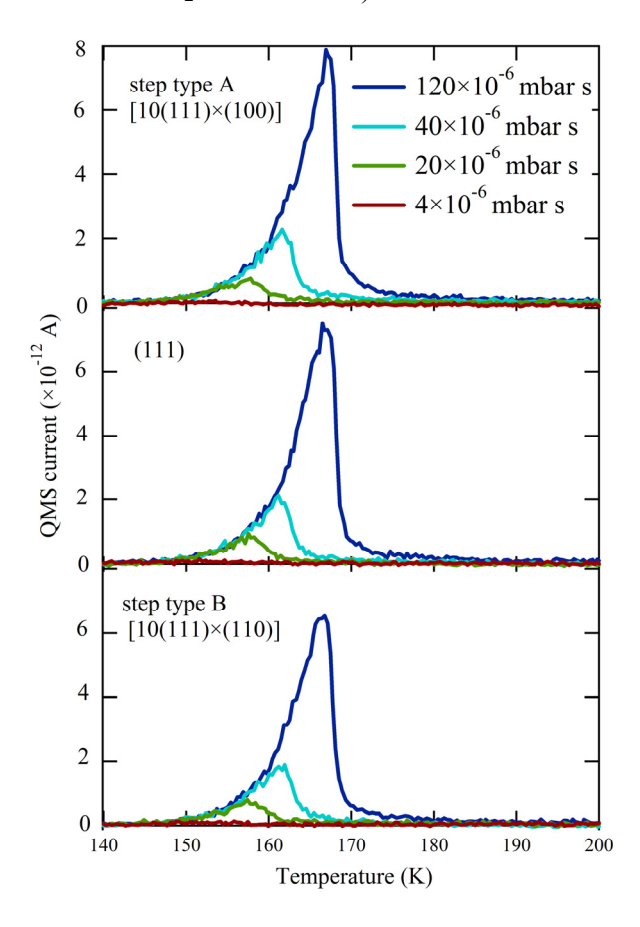


Our STM data, taken later in the UHV-STM apparatus, corroborate these findings. Typical images of  $\sim 50 \times 50 \text{ nm}^2$  are shown in Figure 1c. The middle image shows a large and flat (111) area found near the middle of the crystal. The other images show large areas dominated by monoatomic steps.

Protrusions appearing as white and black spots cover <2% of the surface area. They have an apparent height on the order of 1 nm and remain unidentified, as we detect no elements other than Ag in AES spectra. These protrusions could not be removed by extensive sputtering-annealing or oxidation-reduction cycles, which suggests that they are chemically inert remnants of the polishing process. They are uniformly scattered across the crystal. Although they may influence adsorption/desorption of molecules located in their vicinity, they cannot explain trends as described below for water desorption.

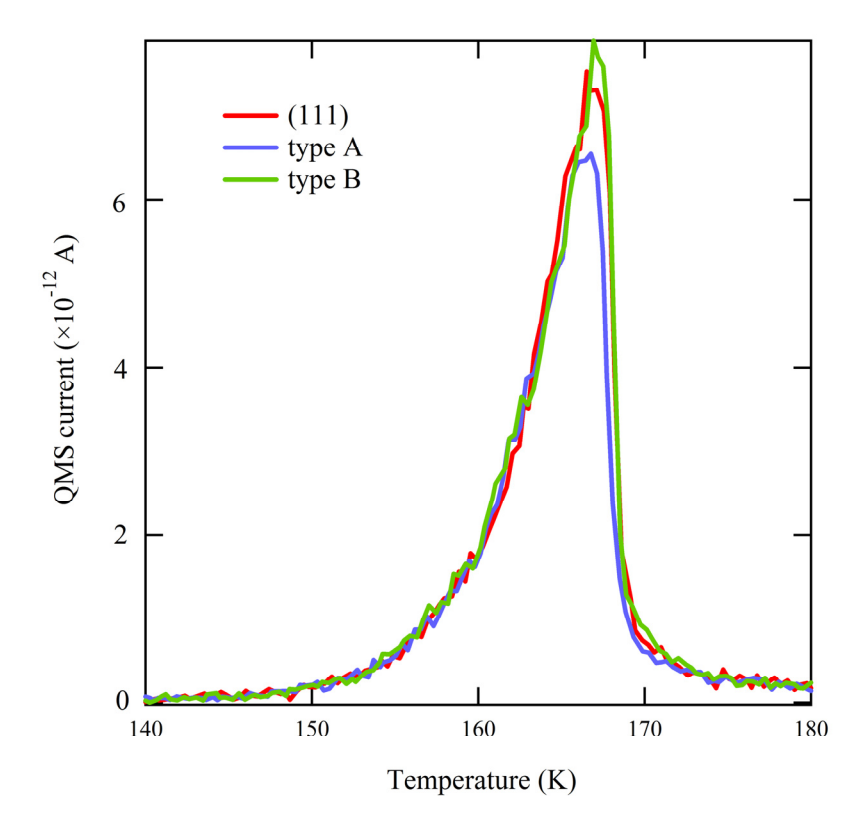
Figure 2 shows three series of H<sub>2</sub>O TPD spectra obtained with the QMS canister at three different positions over the crystal. The surface structure centered at the QMS opening is indicated. For each series, we changed both exposure time and dosing pressure of the H<sub>2</sub>O/He mixture to vary the total exposure 30-fold. The results for the (111) plane (middle panel) are consistent with previous studies [25,31,37,38]. A single desorption feature is observed at all coverages, with overlapping leading edges. This behavior is typical for zeroth-order desorption kinetics and is often interpreted to indicate water desorption from a hydrophobic surface. It is not possible to determine the absolute amount of desorbing water from the integrated QMS response without a separate reference. Therefore we recorded the QMS response for a monolayer of water desorbing from Pt(533) [27] under the same experimental conditions (*i.e.*, crystal-to-QMS aperture distance and QMS settings). On these grounds, the largest traces shown in Figure 2 correspond to the desorption of 2 ML (monolayers).

**Figure 2.** TPD spectra obtained at three separate locations— $[10(111) \times (100)]$ (top), (111) (middle), and  $[10(111) \times (110)]$ (bottom)—for increasing exposures to H<sub>2</sub>O (colored traces, expressed in relative dose of the H<sub>2</sub>O/He mixture).



Apparently, water desorption in the near-monolayer regime is not affected by the presence of A or B type steps; all traces in Figure 2 from comparable doses are identical. When comparing the onsets of multilayered water desorption for identical amounts of adsorbed H<sub>2</sub>O (Figure 3), the traces overlap perfectly. Since water desorption in the multilayer regime is independent of the underlying metal surface structure, this result allows us to conclude that there is no measurable temperature gradient present during the TPD ramp across the curved surface. This conclusion is crucial when we focus on desorption of very small quantities of water.

**Figure 3.** Comparison of the onset of desorption of  $\sim$ 2 ML H<sub>2</sub>O from highly stepped surfaces (types A and B) and flat Ag(111).



Thermal desorption spectra for 0.06–0.08 ML  $H_2O$  are shown in Figure 4 for (111) (left and right bottom traces) and various average terrace widths separated by A (left) and B (right) type steps. A small shift in the peak desorption temperature as a function of step density is apparent when comparing TPD traces for each type of step. To facilitate comparison, the temperature of maximum flux from Ag(111) is indicated. We fit each desorption profile using a single Gaussian function and determine the peak's amplitude (A), width ( $\Delta T$ ), and peak desorption temperature ( $T_p$ ). The fits are shown in Figure 4 as solid traces through the data.

The values of the three fitting parameters are plotted vs. step density in Figure 5. The uncertainties as determined by the fitting procedure are shown as error bars. The desorption amplitude (A) and width ( $\Delta T$ ) are nearly constant. No clear trend with step density is observed. The peak desorption temperature ( $T_p$ ), however, depends significantly on step density over the entire range for both A and B. Translating the crystal over +/-3 mm results in a shift of ~1.5 K for the A step type and ~3.5 K for the

B step type. Over this range, the central surface structure from which desorption is probed changes from approximately  $[6(111) \times (100)]$  to  $[6(111) \times (110)]$ . The temperature shift appears to be proportional to step density. Linear fits are shown as dashed lines. These individual fits suggest that  $T_p$  for the "infinite" (111) plane is  $152.2 \pm 0.1$  K and  $152.1 \pm 0.2$  K, as determined from the A and B steps respectively. The slopes are  $19.7 \pm 1.8$  K × Å and  $42.4 \pm 4.4$  K × Å. Considering the uncertainty of the best-fit parameters and the negligible temperature gradient across the crystal as determined from Figure 3, we conclude that the A and B type steps influence water desorption in an experimentally measurable and different manner. The B step type induces a peak temperature shift approximately twice as large as the A step type. We have attempted to relate this shift to the heat of adsorption from terraces and steps using various standard TPD analyses. However, the sensitivity of our data is limited by two experimental necessities: low  $H_2O$  coverage (to probe steps only) and narrow QMS aperture (to ensure maximal spatial resolution); unfortunately, the present signal-to-noise ratio does not allow us to extract reliable adsorption-enthalpy values.

**Figure 4.** Series of spatially-resolved TPD spectra for 0.06–0.08 ML exposures to  $H_2O$  for the (left) A step type [N(111) × (100)] and (right) B step type [N(111) × (110)]. Solid lines are fits to the data using Gaussian functions.

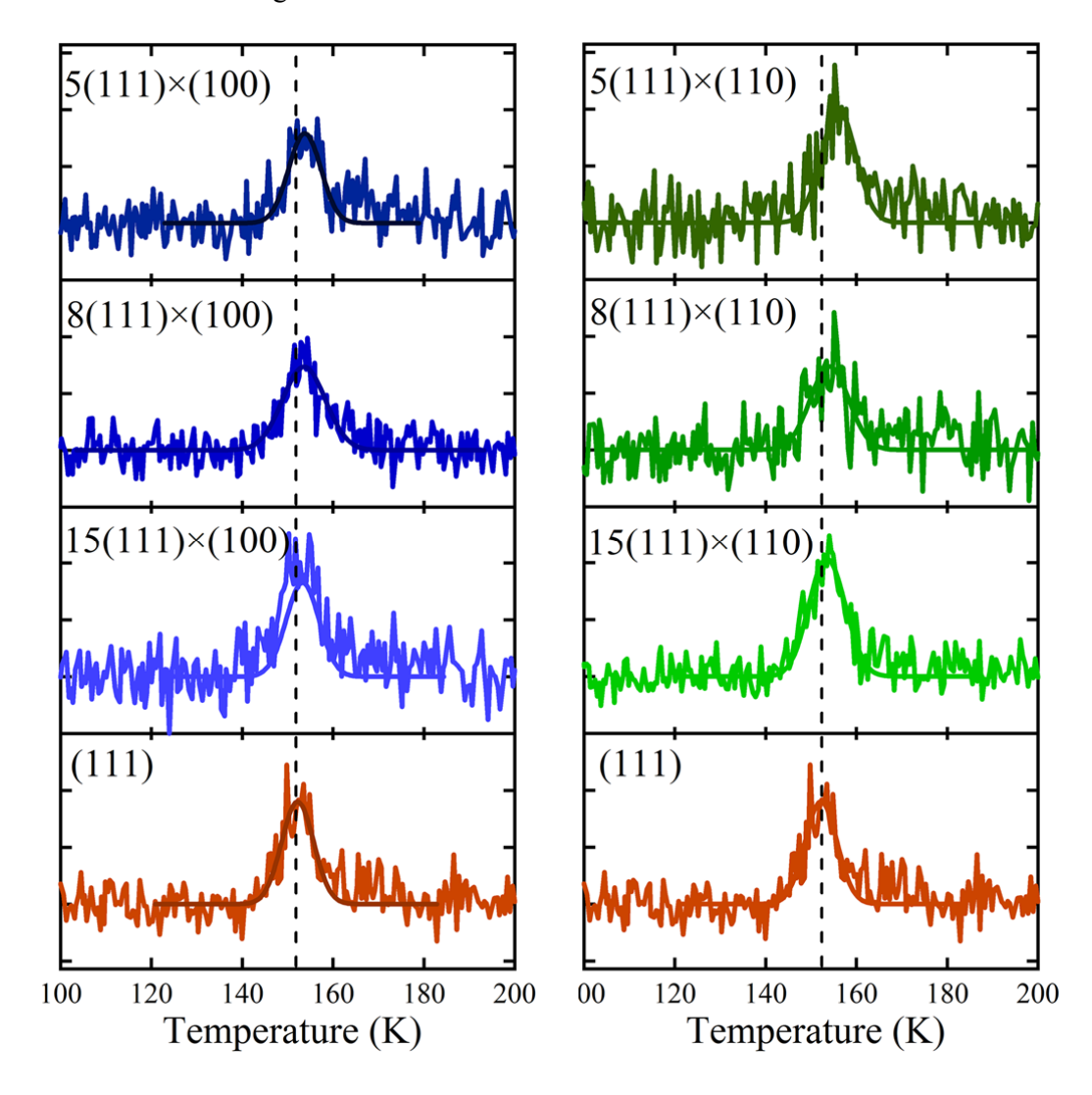
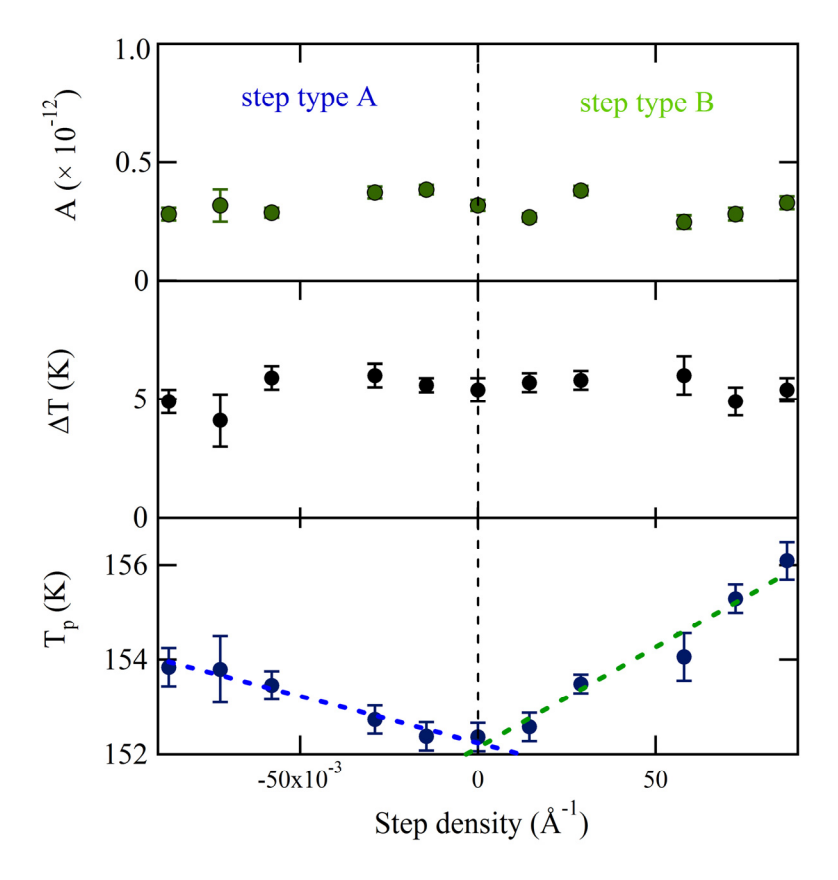


**Figure 5.** Amplitude (A), peak width ( $\Delta T$ ) and peak temperature ( $T_p$ ) determined from fitting spatially-resolved TPD spectra with Gaussian functions.



The results presented here are noteworthy for two reasons. First, the peak temperature shift is small but significant. To our knowledge, this is the first time that a characteristic change in TPD features of this magnitude has been attributed to surface structure. The difference is so small that it would be difficult to determine using multiple flat single crystals. At least 2 or 3 samples with widely varying step densities, of both step types, and an Ag(111) surface would be required to establish this trend. Even then, random sample-to-sample temperature measurement error (caused by irreproducible mounting of samples and thermocouples) is likely to dominate the intrinsically lower random error of a single sample measured multiple times, as here. This point also warns against comparison of results obtained using various (flat or curved) samples when studying adsorption/desorption behavior for systems that may be very sensitive to defect concentrations, or show only small changes with substrate structure or co-adsorbate coverage. Second, considering the shape and near invariance in peak width, it is not immediately obvious how a linear dependence of a peak desorption temperature on step density for adsorbates in the submonolayer regime is to be interpreted. To our knowledge, such a phenomenon has also not been reported before.

To guide our consideration of possible origins for the observed desorption temperature dependence, we first summarize the results of previous publications on the adsorption of water to Ag(111) and related surfaces. The first report of water desorption from Ag(111) by Klaua and Madey [31] shows a single peak with a desorption maximum shifting from 175 K to higher temperatures with increased dosing. In line with zeroth-order desorption kinetics, the leading edges of all traces overlap. Close

inspection of their TPD data shows the onset of desorption at ~141 K. This is in excellent agreement with our results for Ag(111) at very low water coverages, as shown in Figure 4. The same analysis for their desorption data from Ag(100) suggests an onset near 145 K. The first desorption data from Ag(110) by Stuve, Madix and Sexton [39] unfortunately shows a non-flat baseline prior to the desorption, hence these data do not allow us to extract the onset temperature. In a later publication, the onset appears ~140 K for 0.06 ML of water [38]. None of these surfaces showed any evidence for long-range ordering of water molecules by LEED or Electron Stimulated Desorption in Ion Angular Distributions (ESDIAD). The desorption features were interpreted to indicate either dissolving of water clusters in the submonolayer regime and/or sublimation from three-dimensional crystallites. For all these substrates, the intermolecular forces were apparently greater than the interaction of water with the Ag substrate. Multilayered features simply form as a consequence of an increased chance for water molecules to impinge onto two-dimensional ice clusters with increasing exposure and the absence of a dominant driving force to wet the substrate.

In a more recent series of experiments that imaged water on Ag(111) using low temperature STM in the submonolayer regime, Morgenstern and coworkers found single protrusions for water dosed at 70 K [40,41]. These protrusions were interpreted as cyclic water hexamers. Larger stable clusters consisting of heptamers, octamers, and nonamers are also observed when water is dosed at 17 K [42]. The hexamers are buckled, with alternating H-bond lengths as a consequence of a competition between H<sub>2</sub>O's simultaneous tendency to bond with the substrate and act as a hydrogen bond acceptor. At the higher dosing temperature, hexamers mostly conglomerate in large water-covered patches without long-range order [40,41]. An oscillatory distance distribution between water hexamers is caused by electronic surface states [43]. Interestingly, water clusters of different apparent heights were also found along the upper edge of steps even for otherwise uncovered terraces [40,41]. The height variation suggests a variation in cluster size and/or form, and a high barrier for reorientation after water molecules adsorb to the step edge. For Pt(111) [26], similar behavior was observed.

Preferential adsorption to step edges is generally attributed to the Smoluchowski effect [44]: A smoothing of the electronic cloud at a sharp edge lowers electron density at the upper edge. This electronic redistribution was originally inferred from a dependence of the work function of metals on surface structure. However, scanning tunneling spectroscopy (STS) measurements by Avouris *et al.* visualized the local density of states (LDOS) at step edges of Au(111) and Ag(111) [45]. On the upper side, the density of unoccupied states increased at the expense of such states at the lower part of the edge. The associated dipole oriented parallel to the surface was predicted to strongly affect adsorption of molecules. Recently, different types of steps on an Ag(111) surface were also shown by STS to affect the local electronic structure in markedly different ways, indicating that all steps are not equal [46].

Water's electron donating capacity may result in stronger binding to the upper edge. The STM results for water clusters bound to step edges on Ag(111) [40,41] and Pt(111) [26] confirm that steps are the preferred adsorption sites. They also show that diffusion is fast at the dosing temperature, and occurs over distances at least comparable to the terrace widths generally observed for a (111) plane on the time scale of the measurements. A computational study by Scipioni *et al.* finds that the adsorption energy for the water monomer to the B step type is 0.20 eV [47]. This is indeed slightly higher than the 0.18 eV found for the atop site on Ag(111) [32,48]. A comparative study of single water molecules

binding to the A and B step types of Pt(111) did not find an explanation for the experimental result [49]. If the adsorption energy is in fact greater at steps, a shift to higher desorption temperatures is to be expected from surfaces with a greater step density. In so far as different step geometries also have different binding energies, surfaces with comparable densities of different step types will also have different desorption temperatures. Whether or not this is observable is a matter of experimental resolution.

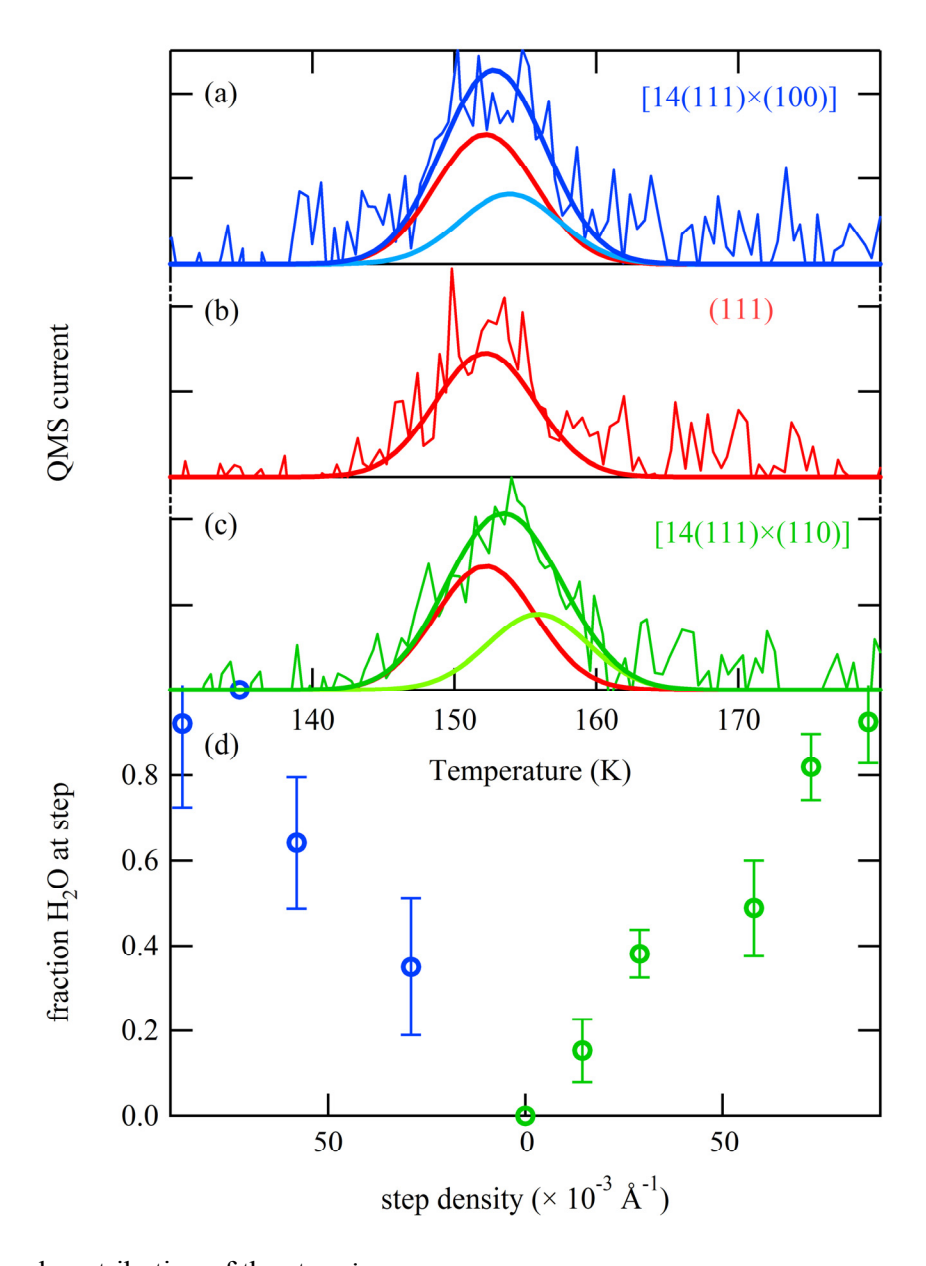
In order to quantify the expected magnitude of such step-dependent TPD shifts, we suggest a simple "two-state model" to explain our results. The two states represent water molecules bound either at a terrace or a step. From all water dosed onto the surface, some fraction finds itself adsorbed as part of cyclic hexamers at (111) terrace sites, whereas the remainder is trapped at a step with a higher binding energy. The sum of these fractions equals 0.06–0.08 ML for the results shown in Figure 4. In the case of a very high step density, nearly all of the water molecules will be bound to a step. When the step density is very low—*i.e.*, close to the center of the crystal—most water will be bound in large water clusters at terraces. Furthermore, we assume that water's binding energy for each fraction is independent of its relative occupancy. This binding energy is governed by the dissolution of the local water structure, which is expected to be different for terraces and steps. Considering our spatial resolution, on either side of the center of the crystal the mass spectrometer's response will be a linear combination of only two contributions, *i.e.*, a contribution from the (111) terraces and a contribution from either the A or the B step type. Desorption of low coverages of water can be modeled accurately with Gaussian line shapes. The integrated signal must represent the total amount of water that was initially adsorbed and which varies only little between the various traces in Figure 4.

QMA intensity = 
$$A^{terraces} \cdot \exp\left(-\left(\frac{T - T_0^{terrace}}{\Delta T^{terrace}}\right)^2\right) + A^{step} \cdot \exp\left(-\left(\frac{T - T_0^{step}}{\Delta T^{step}}\right)^2\right)$$
 (2)

$$\int_{100}^{200} \text{QMA intensity } dT = 0.06-0.08 \text{ ML}$$
 (3)

Values for  $T_0^{terrace}$  and  $T_0^{step}$  are determined from Figure 5. The near absence of steps at the central (111) part of our crystal ensures that most of the 0.06–0.08 ML H<sub>2</sub>O will be condensed as water hexamers, hence we use 152.2 K for  $T_0^{terrace}$ . To determine  $T_0^{step}$  for the A and B step types we take into consideration that a water hexamer spans three atomic rows. We estimate that for a 4-atom wide terrace, these hexamers cannot exist without being anchored to the step edge. Thus, we use the step density of the [4(111) × (100)] and [4(111) × (110)] planes and the linear fits in Figure 5 to estimate  $T_0^{step}$  for desorption from the A and B step types. These are 153.9 K and 155.9 K, respectively. Note that these values would hardly change if we would choose any other value close to N = 4. For all terrace and step desorption peaks we assume a Gaussian width ( $\Delta T^{terrace}$  and  $\Delta T^{step}$ ) of 5.0 K, as Figure 5 suggests this to be an accurate value for both extremes. We now fit the sum of the two Gaussian contributions on either side of the middle of the crystal to our data and extract the relative amplitudes for the terrace and step contributions,  $A^{terrace}$  and  $A^{step}$ . The contributions by the terrace-bound hexamers (red) and steps (green and blue), as well as the total desorption intensity, are shown in Figure 6a–c for three surface structures.

**Figure 6.** (a–c) Deconvolution of TPD features from three different surface structures into contributions from (111)-bound hexamers and water clusters bound to A (blue) and B (green) type step edges. (d) Fractional contribution of steps to the total observed desorption as obtained for a two-state model.



The fractional contribution of the step, *i.e.*,:

$$\frac{\int_{100}^{200} A^{step} dT}{\int_{100}^{200} A^{terrace} dT + \int_{100}^{200} A^{step} dT}$$
(4)

to the total desorption intensity in this two-state desorption model is shown in Figure 6d. The linearity of the step contribution on either side of (111) indicates that the model is self-consistent and fits our data well.

# 3. Experimental Section

To allow for easy variation of step type and step density, we use an Ag single crystal with a well-polished curved surface. The curvature is in principle due to atomic steps separating terraces (Figure 7a); faceting and step bunching have been observed for curved Pt [15], Au [19] and Ni [21] samples, but not Ag. Consider a cylinder of FCC crystal with its axis along the [-110] direction. Our sample is a partial slice normal to the axis, with a [111] vector radially bisecting 31° of azimuth (thus exposing Ag(111) at the apex, as in Figure 7). To one side of the apex are (100) steps (type A) running parallel to the axis, increasing in density with increasing azimuthal angle. To the other side are (110) steps (type B). Whereas the A step type consists of a square arrangement, the B step type consists of a rectangular arrangement of atoms. A Laue back reflection study indicates that our crystal's normal is not exactly the [111] direction. It is tilted by ~0.6° in the [110] direction and ~0.3° in the [011] direction. These deviations cause the "infinite" (111) plane to be slightly off the center of the crystal's curvature. In addition, the crystal is azimuthally rotated by ~1°. This causes a non-straight average step direction and thus a small difference in the number of R vs. S-type kinks.

**Figure 7.** (a) Schematic drawing of a curved FCC metal single crystal with [111] centered at the apex; (b) Schematic drawing of the atomic arrangements of the A and B step types, which run parallel to the cylindrical axis (normal to the page) and separate the (111) terraces (top view).

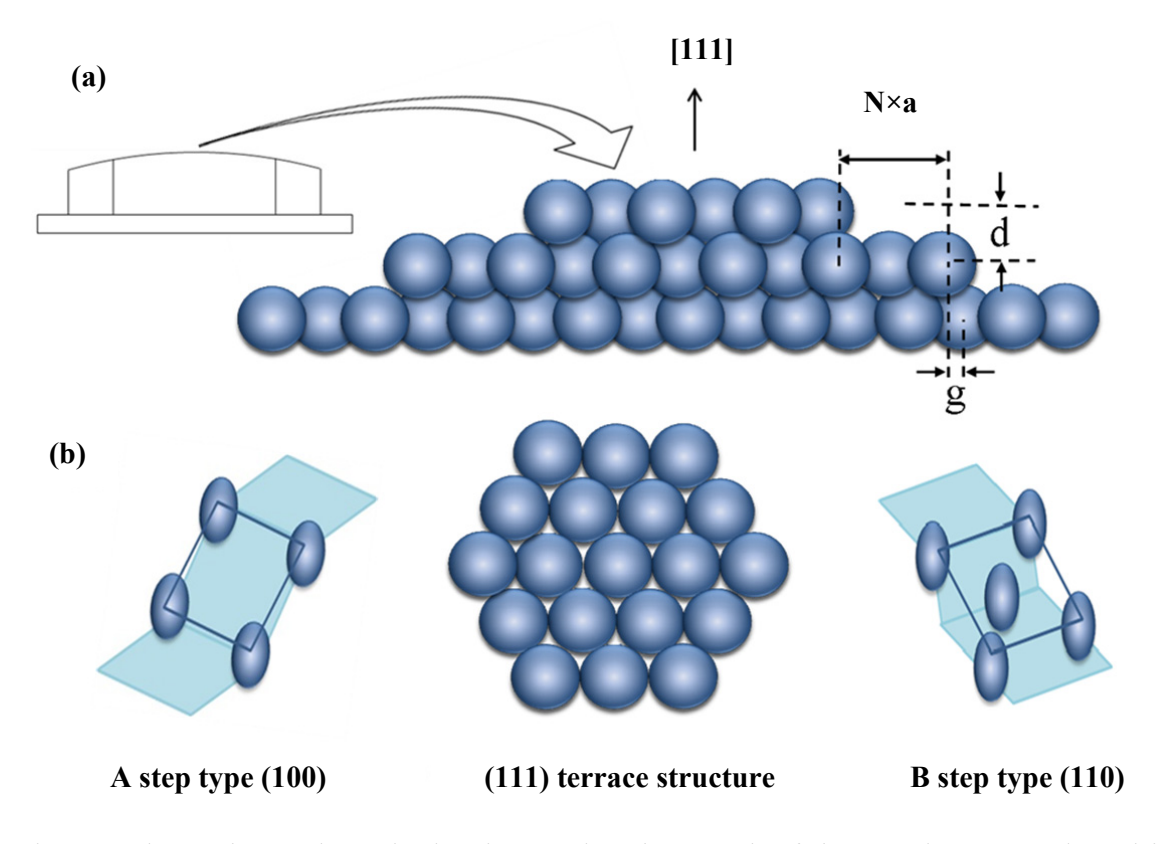
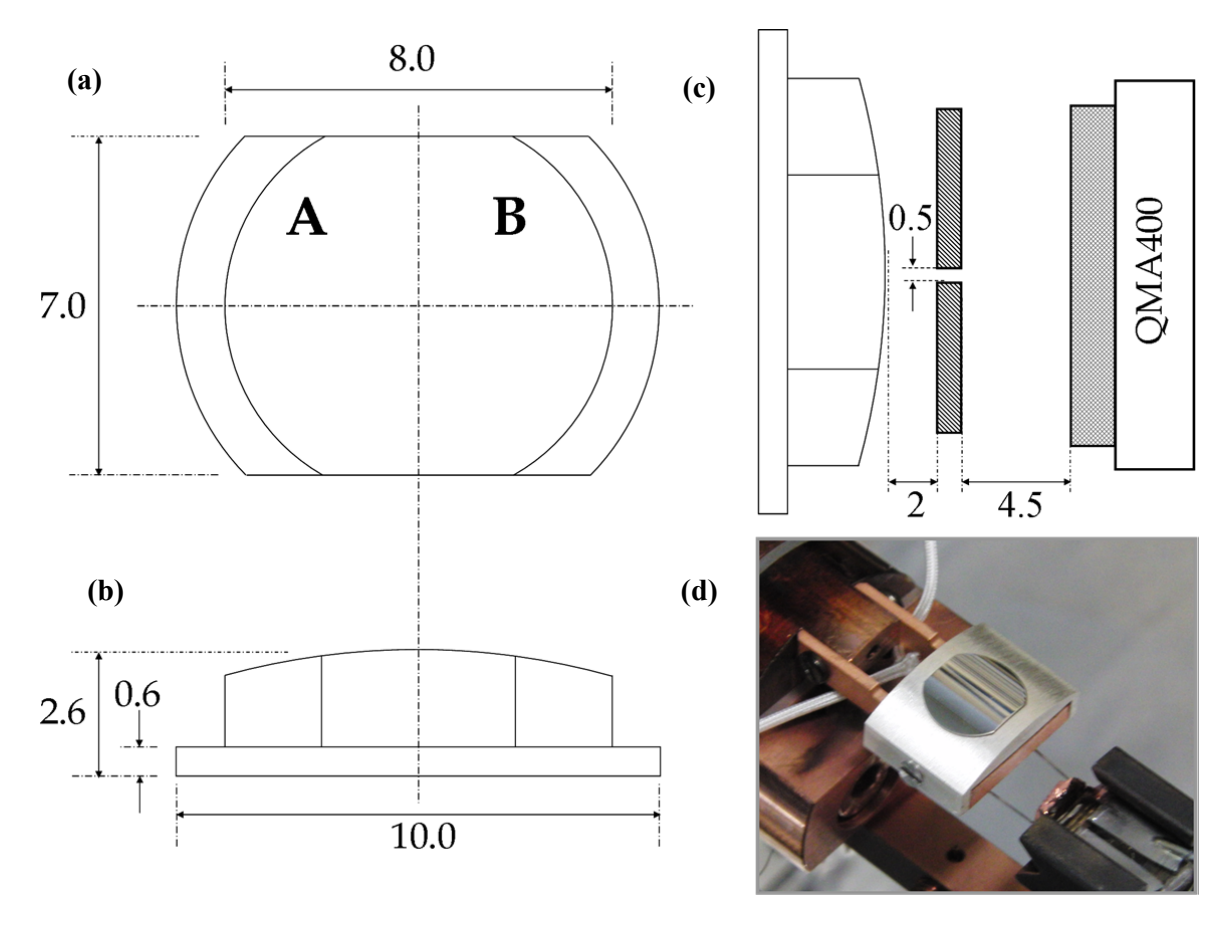


Figure 8 shows three schematic drawings and a photograph of the actual Ag crystal used in our studies. The surface is curved and polished only on its top side. It may be considered a  $31^{\circ}$  section of a 30 mm diameter cylinder. With this angle, the surface structures range from approximately [5(111)  $\times$ 

(100)] on the outer left side (front view) via (111) near the middle to  $[5(111) \times (110)]$  on the outer right side. The initial crystal was spark eroded from an Ag boule. It was circular, 10 mm in diameter and  $\sim 3$  mm thick. At the edge, a 1 mm wide ring was removed to leave a 0.6 mm thick flange and 8 mm diameter top surface. The sides were removed making it 7 mm wide. The curvature on the top of the crystal was initially created by spark erosion and sanding. The crystal was subsequently polished in an automated, custom built polishing machine (Surface Preparation Laboratory, Zaandam, The Netherlands).

**Figure 8.** Schematic drawings (dimensions in mm) of the curved Ag crystal (a) front view with step type indication (b) bottom view (c) edge view of crystal in front of the differentially pumped QMS (d) Photograph of the crystal with retaining Ag cap.



At its 1 mm wide flange, the crystal is held by a polycrystalline Ag cap onto a Cu base plate by two screws (Figure 8d). This assembly is connected with two solid Cu leads extending from the base plate to a bath cryostat. It is electrically isolated using AlN blocks (not visible in the picture). The cryostat is inserted into the ultrahigh vacuum (UHV) chamber through an x, y, z, 9 manipulator. Behind the base plate, a filament from a commercial light bulb (Osram, Capelle a/d IJssel, The Netherlands) enables uniform heating of the base plate and crystal. The filament is spring loaded at its glass base. Heating is performed either radiatively or by electron bombardment using a positive voltage on the crystal assembly while the filament is grounded. A type-K thermocouple is inserted into the side of the Ag polycrystalline cap. For temperature control, we use a PID controller with an internal ice point reference (Eurotherm 2416, Ashburn, VA, USA).

The crystal assembly was initially held in a home-built UHV surface science chamber for cleaning and surface structure determination using LEED. This system has a base pressure of 3  $\times$  10<sup>-10</sup> mbar and contains, amongst others, a sputter gun (IS 40C1, Prevac, Rogów, Poland), a QMS (Prisma 200, Pfeiffer Vacuum GmbH, Aßlar, Germany), and LEED optics (RVL2000/8/R, LK Technologies, Bloomington, IN, USA). The crystal was cleaned by sputtering-annealing cycles. We sputter using Ar<sup>+</sup> (6.0 Messer, Moerdijk, The Netherlands) at 600 V and 2  $\mu$ A while rotating the crystal 2° per minute, and anneal at 675 K for 10 min. LEED studies were performed with the electron beam impinging along [111] at all locations along the curved surface. The surface was translated normal to the impinging electron beam.

Subsequently, the crystal assembly was moved to a second home-built UHV chamber with a base pressure of 9 × 10<sup>-11</sup> mbar for spatially-resolved TPD studies. Here, a Baltzers QMA400 head is kept in a differentially pumped canister that connects to the main UHV chamber via a  $0.5 \times 5 \text{ mm}^2$ rectangular slot (Figure 8b). The curved crystal is positioned ~2 mm from this orifice for TPD studies. It is translated laterally to monitor desorption from different surface structures in separate experiments. We have modelled the geometric effects on the mass spectrometer's instrument function for various desorption profiles. We find that, in the worst-case scenario of a broad cosine distribution, the spatial resolution is limited by the angular width of this distribution (rather than the angular width of the slit) to 3.1 mm (FWHM). Under these conditions we will detect some desorption (~10%) from the center of the crystal when performing TPD experiments at the edge of the crystal's curvature. When desorption is more strongly directed along the local surface normal, spatial resolution increases. H<sub>2</sub>O (Millipore, 18.2 M $\Omega$ ) was dosed onto the Ag sample at 86 K using a home-built 10 mm diameter capillary array doser at a distance large enough to ensure a uniform flux across the entire cleaned surface. The water was degassed by multiple freeze-pump-thaw cycles and backfilled with 1.1 bar He (6N, Air Products, Amsterdam, The Netherlands) prior to experiments. The H<sub>2</sub>O/He mixture was generally dosed onto the crystal for different durations at a fixed pressure of  $1 \times 10^{-7}$  mbar in the UHV chamber, as determined by an uncalibrated cold cathode gauge. Co-dosing with He allows us to dose H<sub>2</sub>O reproducibly, as the co-dosed He yields a large and accurately determined pressure change. Subsequent TPD experiments were performed at 1.0 K/s while monitoring m/z = 18. We have verified by TPD that the cold sample did not accumulate CO (m/z = 28) to measurable amounts prior to or during the experiment. LEED (LK Technologies RVL2000/8/R) was regularly used to verify the structure of the bare Ag surface, while AES was used to verify cleanliness (ESA 100, Staib Instruments, Langenbach, Germany).

Finally, the crystal's surface was also studied using scanning tunnelling microscopy (STM). Here, we employ a commercial Omicron UHV system containing separate preparation and analysis chambers. The latter has a base pressure of  $2 \times 10^{-10}$  mbar and contains a variable temperature STM. We redesigned the sample holder such that the entire polished surface could be imaged, while the holder still fit inside the analysis chamber's sample carousel. Parts of the sample holder in proximity to the sample's polished surface were covered by an Ag foil to prevent cross-contamination of the sample during sputtering. Tungsten STM tips were prepared by electrochemical etching in NaOH using DC current. Under UHV conditions, tip treatment also included heating the tip apex with a 100–500  $\mu$ A electron emission current to remove tungsten oxide and tip stabilisation by applying 2–3 V pulses wile scanning. We used AES (VG 100AX hemispherical analyzer in combination with a LEG-63 electron gun) and LEED (VG RVL900) regularly to verify cleanliness and long-range surface order. AES

spectra never showed any sign of adsorbed oxygen,  $O_{ads}$ , on any of the stepped (111) surfaces, even after prolonged exposure ( $\sim 10^3$  mbar  $\times$  s) to  $O_2$  at room temperature.

#### 4. Conclusions

We have presented a study of water desorption from a curved single crystal surface. We find a shift in the desorption temperature for very small coverages that we believe originates from small differences in the dissolution and consecutive desorption energies of water clusters bound to the (111) terrace and the upper edge of steps. The stronger shift for the B step type indicates a stronger binding to this (110) edge. We note that the same trend has been observed on Pt, where too the B type step induces a larger temperature shift than the A step type in desorption of the last water molecules [28]. This observation may hint at a more general rule regarding the bond strength of water to step edges, and a relation to the size of the Smolukowski effect at A and B step types for FCC metals.

Our study furthermore demonstrates major experimental advantages of using curved samples in surface science: In addition to the time saved by not swapping crystals, the random temperature-measurement error introduced by sample-to-sample variations in thermal contact is eliminated. With demonstrably low scatter of the temperature readings, we can find evidence for a very small difference in binding energy between water clusters at (111) terrace sites and the A and B step types on this noble metal. It is unlikely that such sensitivity could be achieved with a conventional study of multiple flat single crystals. Thus, our approach makes finer quantitative distinctions, which can in turn serve as benchmarks for theoretical calculation of binding energy differences between closely related adsorption sites.

## Acknowledgments

The Thailand Research Fund (TRF), Office of the Higher Education Commission (CHE), and the Leiden Institute of Chemistry are gratefully acknowledged for the financial support of this project. The authors also thank the Royal Golden Jubilee Ph.D. scholarship from TRF for N.P.

## **Author Contributions**

Conception, design of experiments: Jakrapan Janlamool, Dima Bashlakov, Otto Berg, and Ludo B.F. Juurlink. External guidance of Thai students: Piyasan Praserthdam, Bunjerd Jongsomjit.

# **Conflicts of Interest**

The authors declare no conflict of interest.

#### References

- 1. Somorjai, G.A. The structure sensitivity and insensitivity of catalytic reactions in light of the adsorbate induced dynamic restructuring of surfaces. *Catal. Lett.* **1990**, 7, 169–182.
- 2. Norskov, J.K.; Bligaard, T.; Hvolbaek, B.; Abild-Pedersen, F.; Chorkendorff, I.; Christensen, C.H. The nature of the active site in heterogeneous metal catalysis. *Chem. Soc. Rev.* **2008**, *37*, 2163–2171.

3. Van Santen, R.A. Complementary structure sensitive and insensitive catalytic relationships. *Acc. Chem. Res.* **2008**, *42*, 57–66.

- 4. Behrens, M.; Studt, F.; Kasatkin, I.; Kühl, S.; Hävecker, M.; Abild-Pedersen, F.; Zander, S.; Girgsdies, F.; Kurr, P.; Kniep, B.-L.; *et al.* The active site of methanol synthesis over Cu/ZnO/Al2O3 industrial catalysts. *Science* **2012**, *336*, 893–897.
- 5. Honkala, K.; Hellman, A.; Remediakis, I.N.; Logadottir, A.; Carlsson, A.; Dahl, S.; Christensen, C.H.; Norskov, J.K. Ammonia synthesis from first-principles calculations. *Science* **2005**, *307*, 555–558.
- 6. Schauermann, S.; Nilius, N.; Shaikhutdinov, S.; Freund, H.J. Nanoparticles for heterogeneous catalysis: New mechanistic insights. *Acc. Chem. Res.* **2013**, *46*, 1673–1681.
- 7. Fiordaliso, E.M.; Murphy, S.; Nielsen, R.M.; Dahl, S.; Chorkendorff, I. H-2 splitting on Pt, Ru and Rh nanoparticles supported on sputtered HOPG. *Surf. Sci.* **2012**, *606*, 263–272.
- 8. Strebel, C.; Murphy, S.; Nielsen, R.M.; Nielsen, J.H.; Chorkendorff, I. Probing the active sites for CO dissociation on ruthenium nanoparticles. *Phys. Chem. Chem. Phys.* **2012**, *14*, 8005–8012.
- 9. Armitage, A.F.; Woodruff, D.P.; Johnson, P.D. Crystallographic incident beam effects in quantitative Auger electron spectroscopy. *Surf. Sci.* **1980**, *100*, L483–L490.
- 10. Besocke, K.; Krahl-Urban, B.; Wagner, H. Dipole moments associated with edge atoms; A comparative study on stepped Pt, Au and W surfaces. *Surf. Sci.* **1977**, *68*, 39–46.
- 11. Gardiner, T.M.; Kramer, H.M.; Bauer, E. The surface structure of the <110> zone of tungsten: A LEED and work function study. *Surf. Sci.* **1981**, *112*, 181–196.
- 12. Hopster, H.; Ibach, H.; Comsa, G. Catalytic oxidation of carbon monoxide on stepped platinum(111) surfaces. *J. Catal.* **1977**, *46*, 37–48.
- 13. Moison, J.M.; Domange, J.L. Substrate steps/adsorbed layer interaction; selective effect on the possible epitaxial relationships: Case of the the S/Cu(111) system. *Surf. Sci.* **1977**, *69*, 336–348.
- 14. Pluis, B.; van der Gon, A.W.D.; Frenken, J.W.M.; van der Veen, J.F. Crystal-face dependence of surface melting. *Phys. Rev. Lett.* **1987**, *59*, 2678–2681.
- 15. Sander, M.; Imbihl, R.; Ertl, G., Kinetic oscillations in catalytic CO oxidation on a cylindrical Pt single crystal surface. *J. Chem. Phys.* **1992**, *97*, 5193–5204.
- 16. Hahn, C.; Shan, J.; Liu, Y.; Berg, O.; Kleijn, A.W.; Juurlink, L.B.F. Employing a cylindrical single crystal in gas-surface dynamics. *J. Chem. Phys.* **2012**, *136*, doi:10.1063/1.3692686.
- 17. Lawton, T.J.; Pushkarev, V.; Broitman, E.; Reinicker, A.; Sykes, E.C.H.; Gellman, A.J. Initial oxidation of Cu(hkl) surfaces vicinal to Cu(111): A high-throughput study of structure sensitivity. *J. Phys. Chem. C* **2012**, *116*, 16054–16062.
- 18. Ortega, J.E.; Corso, M.; Abd-el-Fattah, Z.M.; Goiri, E.A.; Schiller, F. Interplay between structure and electronic states in step arrays explored with curved surfaces. *Phys. Rev. B* **2011**, *83*, doi:http://dx.doi.org/10.1103/PhysRevB.83.085411.
- 19. Corso, M.; Schiller, F.; Fernandez, L.; Cordon, J.; Ortega, J.E. Electronic states in faceted Au(111) studied with curved crystal surfaces. *J. Phys. Condens. Matter* **2009**, *21*, doi:10.1088/0953-8984/21/35/353001.
- 20. Lobo-Checa, J.; Ortega, J.E.; Mascaraque, A.; Michel, E.G.; Krasovskii, E.E. Effect of photoelectron mean free path on the photoemission cross-section of Cu(111) and Ag(111) Shockley states. *Phys. Rev. B* **2011**, *84*, doi:http://dx.doi.org/10.1103/PhysRevB.84.245419.

21. Mom, R.V.; Hahn, C.; Jacobse, L.; Juurlink, L.B.F. LEED analysis of a nickel cylindrical single crystal. *Surf. Sci.* **2013**, *613*, 15–20.

- 22. De Alwis, A.; Holsclaw, B.; Pushkarev, V.V.; Reinicker, A.; Lawton, T.J.; Blecher, M.E.; Sykes, E.C.H.; Gellman, A.J. Surface structure spread single crystals (S<sub>4</sub>C): Preparation and characterization. *Surf. Sci.* **2013**, *608*, 80–87.
- 23. Henderson, M.A. The interaction of water with solid surfaces: Fundamental aspects revisited. *Surf. Sci. Rep.* **2002**, *46*, 1–308.
- 24. Hodgson, A.; Haq, S. Water adsorption and the wetting of metal surfaces. *Surf. Sci. Rep.* **2009**, *64*, 381–451.
- 25. Thiel, P.A.; Madey, T.E. The interaction of water with solid surfaces: Fundamental aspects. *Surf. Sci. Rep.* **1987**, *7*, 211–385.
- 26. Morgenstern, M.; Michely, T.; Comsa, G. Anisotropy in the adsorption of H<sub>2</sub>O at low coordination sites on Pt(111). *Phys. Rev. Lett.* **1996**, 77, 703–706.
- 27. Van der Niet, M.J.T.C.; Dominicus, I.; Koper, M.T.M.; Juurlink, L.B.F. Hydrophobic interactions between water and pre-adsorbed D on the stepped Pt(533) surface. *Phys. Chem. Chem. Phys.* **2008**, *10*, 7169–7179.
- 28. Van der Niet, M.J.T.C.; den Dunnen, A.; Juurlink, L.B.F.; Koper, M.T.M. The influence of step geometry on the desorption characteristics of O<sub>2</sub>, D<sub>2</sub>, and H<sub>2</sub>O from stepped Pt surfaces. *J. Chem. Phys.* **2010**, *132*, doi:10.1063/1.3407434...
- 29. Van der Niet, M.J.T.C.; den Dunnen, A.; Juurlink, L.B.F.; Koper, M.T.M. Co-adsorption of O and H<sub>2</sub>O on nanostructured platinum surfaces: Does OH form at steps? *Angew. Chem. Int. Ed.* **2010**, 49, 6572–6575.
- 30. Den Dunnen, A.; van der Niet, M.J.T.C.; Badan, C.; Koper, M.T.M.; Juurlink, L.B.F. Long-range influence of steps on water adsorption on clean and D-covered Pt surfaces. Leiden University, Leiden, The Netherlands. Unpublished work, 2014.
- 31. Klaua, M.; Madey, T.E. The adsorption of H<sub>2</sub>O on clean and oxygen-dosed silver single crystal surfaces. *Surf. Sci.* **1984**, *136*, L42–L50.
- 32. Ranea, V.A.; Michaelides, A.; Ramirez, R.; Verges, J.A.; de Andres, P.L.; King, D.A. Density functional theory study of the interaction of monomeric water with the Ag{111} surface. *Phys. Rev. B* **2004**, *69*, doi:10.1103/PhysRevB.69.205411.
- 33. Zimbitas, G.; Haq, S.; Hodgson, A. The structure and crystallization of thin water films on Pt(111). *J. Chem. Phys.* **2005**, *123*, doi:org/10.1063/1.2060691.
- 34. Zimbitas, G.; Hodgson, A. The morphology of thin water films on Pt(111) probed by chloroform adsorption. *Chem. Phys. Lett.* **2006**, *417*, 1–5.
- 35. Henzler, M. LEED-investigation of step arrays on cleaved germanium (111) surfaces. *Surf. Sci.* **1970**, *19*, 159–171.
- 36. Van Hove, M.A.; Somorjai, G.A. A new microfacet notation for high-Miller-index surfaces of cubic materials with terrace, step and kink structures. *Surf. Sci.* **1980**, *92*, 489–518.
- 37. Bange, K.; Madey, T.E.; Sass, J.K. Characterization of OH(ad) formation by reaction between H<sub>2</sub>O and O(ad) on Ag(110). *Surf. Sci.* **1985**, *152–153*, 550–558.

38. Bange, K.; Madey, T.E.; Sass, J.K.; Stuve, E.M. The adsorption of water and oxygen on Ag(110): A study of the interactions among water molecules, hydroxyl groups, and oxygen atoms. *Surf. Sci.* **1987**, *183*, 334–362.

- 39. Stuve, E.M.; Madix, R.J.; Sexton, B.A. The adsorption and reaction of H<sub>2</sub>O on clean and oxygen covered Ag(110). *Surf. Sci.* **1981**, *111*, 11–25.
- 40. Morgenstern, K. Scanning tunnelling microscopy investigation of water in submonolayer coverage on Ag(1 1 1). *Surf. Sci.* **2002**, *504*, 293–300.
- 41. Morgenstern, K.; Nieminen, J. Intermolecular bond length of ice on Ag(111). *Phys. Rev. Lett.* **2002**, *88*, doi:10.1103/PhysRevLett.88.066102.
- 42. Michaelides, A.; Morgenstern, K. Ice nanoclusters at hydrophobic metal surfaces. *Nat. Mater.* **2007**, *6*, 597–601.
- 43. Mehlhorn, M.; Simic-Milosevic, V.; Jaksch, S.; Scheier, P.; Morgenstern, K. The influence of the surface state onto the distance distribution of single molecules and small molecular clusters. *Surf. Sci.* **2010**, *604*, 1698–1704.
- 44. Smoluchowski, R. Anisotropy of the electronic work function of metals. *Phys. Rev.* **1941**, *60*, 661–674.
- 45. Avouris, P.; Lyo, I.W.; Molinasmata, P. STM studies of the interaction of surface-state electrons on metals with steps and adsorbates. *Chem. Phys. Lett.* **1995**, *240*, 423–428.
- 46. Heidorn, S.; Morgenstern, K. Spatial variation of the surface state onset close to three types of surface steps on Ag(111) studied by scanning tunnelling spectroscopy. *New J. Phys.* **2011**, *13*, doi:10.1088/1367-2630/13/3/033034.
- 47. Scipioni, R.; Donadio, D.; Ghiringhelli, L.M.; delle Site, L. Proton wires via one-dimensional water chains adsorbed on metallic steps. *J. Chem. Theory Comput.* **2011**, *7*, 2681–2684.
- 48. Michaelides, A.; Ranea, V.A.; de Andres, P.L.; King, D.A. General model for water monomer adsorption on close-packed transition and noble metal surfaces. *Phys. Rev. Lett.* **2003**, *90*, doi:org/10.1103/PhysRevLett.90.21610.
- 49. Kolb, M.J.; Calle-Vallejo, F.; Juurlink, L.B.F.; Koper, M.T.M. Density functional theory study of adsorption of H<sub>2</sub>O, H, O and OH on stepped platinum surfaces. *J. Chem. Phys.* **2014**, doi:10.1063/1.4869749.

Sample Availability: Not available.

© 2014 by the authors; licensee MDPI, Basel, Switzerland. This article is an open access article distributed under the terms and conditions of the Creative Commons Attribution license (http://creativecommons.org/licenses/by/3.0/).

FISEVIER

Contents lists available at ScienceDirect

# **Catalysis Communications**

journal homepage: www.elsevier.com/locate/catcom



#### Short communication

# Oxidative dehydrogenation of ethanol over AgLi–Al<sub>2</sub>O<sub>3</sub> catalysts containing different phases of alumina



Jakrapan Janlamool, Bunjerd Jongsomjit \*

Center of Excellence on Catalysis and Catalytic Reaction Engineering, Department of Chemical Engineering, Faculty of Engineering, Chulalongkorn University, Bangkok 10330, Thailand

#### ARTICLE INFO

Article history: Received 26 March 2015 Received in revised form 21 July 2015 Accepted 28 July 2015 Available online 4 August 2015

Keywords:
Oxidative dehydrogenation
Alumina
Ethanol
Silver
Lithium

#### ABSTRACT

Oxidative dehydrogenation of ethanol over the AgLi–Al $_2$ O $_3$  catalysts having different phase compositions of alumina was investigated. The pure gamma (CHI00), pure chi (CHI100) and equally mixed phases (CHI50) derived from the solvothermal synthesis can play important roles on the physicochemical properties of AgLi–Al $_2$ O $_3$  catalysts. Especially, the amount of weak basic sites, the oxidation state of Ag, and the reduction behaviors of catalysts are crucial in determining the ethanol conversion and product selectivity. It was found that increased amounts of weak basic sites and  $Ag_0^8$ <sup>+</sup> clusters enhanced the catalytic activity as seen for the AgLi–CHI50 catalyst.

© 2015 Elsevier B.V. All rights reserved.

#### 1. Introduction

At present, ethanol essentially derived from biomass via fermentation is a promising alternative feedstock to produce chemicals usually obtained from petroleum-based materials. Therefore, the transformation of ethanol to other valuable chemicals via catalytic reaction is very captivating. One of the most attractive reactions is oxidative dehydrogenation of alcohol to aldehydes and ketones, which plays a fundamental role in organic synthesis due to the versatility of the carbonyl group as a desirable block using preferential oxygen as oxidant [1,2]. It is known that the oxidative dehydrogenation of ethanol to acetaldehyde displays the presence of redox sites on the catalyst [3]. In addition, the formation of acetaldehyde has been performed on the wide basic catalysts. However, the dehydration of alcohols to alkenes/ether can be a side reaction during oxidative dehydrogenation on a solid acid catalyst at high temperature. Moreover, the oxidative degradation of carbon chain to carbon monoxide and carbon dioxide is also the main side reaction in oxidative dehydrogenation, especially at high temperature [4].

Today, heterogeneous catalysts for selective oxidation are often based on Cu [5], Au [6], and Pd [7,8]. However, the Ag-based catalysts have been attractively applied for a wide variety of oxidation application such as CO oxidation [9,10], toluene oxidation [11,12], formaldehyde oxidation [13,14], and selective reduction of NO [15] due to its low price. Among alkali metals, lithium is found to be the most attractive for being used as a promoter. For instance, the increase of Li<sub>2</sub>O content in iron catalysts can reduce the dehydration pathway due to the

 $\textit{E-mail address:} \ bunjerd.j@chula.ac.th \ (B.\ Jongsomjit).$ 

neutralization of a large fraction of surface acidity [16]. Hence, the combination of AgLi-based catalysts seems to be promising for oxidative dehydrogenation of alcohol to aldehydes and ketones. In addition, the nanocrystalline alumina having mixed  $\gamma$ - and  $\chi$ -crystalline phases can be prepared from the thermal decomposition of aluminium isopropoxide (AIP) in organic solvent [17]. Based on the previous study, mixed phase alumina can be employed as catalyst supports for CO oxidation [17] and propane oxidation [18].

This present study is aimed to investigate changes in catalytic behaviors of AgLi–Al<sub>2</sub>O<sub>3</sub> catalysts with different phases of alumina for oxidative dehydrogenation of ethanol. The alumina was synthesized by the solvothermal methods to obtain controllable different phases of alumina. Then, the AgLi–Al<sub>2</sub>O<sub>3</sub> catalysts were prepared via a simple coimpregnation method. The characteristics of catalysts were identified rigorously by means of CO<sub>2</sub>-TPD, UV–visible spectroscopy, TPR, and other techniques. The correlation between the characteristics and catalytic behaviors via oxidative dehydrogenation is discussed further.

#### 2. Experimental

2.1. Preparation of different phases of alumina and AgLi-Al<sub>2</sub>O<sub>3</sub> catalysts

The alumina having different phases was prepared by the solvothermal method as reported by Meephoka et al. [17]. By varying the synthesis solvent, the pure gamma (CHI00), pure chi (CHI100) and equally mixed phases (CHI50) of alumina were obtained as confirmed by the XRD measurement.

<sup>\*</sup> Corresponding author.

Then, the  $AgLi-Al_2O_3$  catalysts were prepared by the incipient wetness coimpregnation method using the mixture of aqueous solution of silver nitrate and lithium nitrate in order to obtain 4.7 wt.% of Ag and 0.7 wt.% of Li on the different phases of alumina. The final catalyst was calcined in air at 400 °C for 4 h. The catalysts are denoted as AgLi-CHI00, AgLi-CHI100, and AgLi-CHI50 upon different phase compositions present in alumina.

#### 2.2. Catalyst characterization

All catalyst precursors and final catalysts were characterized by several techniques as follows:

*X-ray diffraction (XRD)*: Bruker D8 Advance X-ray diffractometer with Cu- $K_{\alpha}$  radiation ( $\lambda = 1.54056$  Å) was used to determine the phase composition of catalysts.

 $N_2$  physisorption:  $N_2$  physisorption ( $N_2$  adsorption at -196 °C in a Micromeritics ASPS 2020) was performed to determine surface areas, pore size and pore volume of the different catalysts.

*UV*–*visible absorption spectroscopy*: the oxidation state of Ag was determined using UV–*visible absorption spectroscopy* (Perkin Elmer Lamda-650, wavelength of 200–600 nm with a step size at 1 nm).

Carbon dioxide temperature-programmed desorption ( $CO_2$ -TPD): the basicity of catalyst was determined by  $CO_2$ -TPD using a Micromeritics Chemisorp 2750. First, 0.10 g of the catalyst was pretreated at 500 °C with flowing of helium for 1 h. Then, the catalyst was saturated with pure  $CO_2$  at 30 °C. After saturation, the physisorbed  $CO_2$  was desorbed in a He flow. Then, the catalyst was heated from 30 to 500 °C with a heating rate of 10 °C/min. The effluent amount of  $CO_2$  was measured via thermal conductivity detector (TCD).

Temperature-programmed reduction (TPR): the reduction behavior of catalysts was evaluated by TPR. 0.1 g catalyst was used and pretreated at 250 °C under nitrogen flow for 1 h. The reduction profile was operated at temperature ramping to 500 °C with 10 °C/min during flowing of  $10\% H_2$  in Ar.

#### 2.3. Reaction test

Oxidative dehydrogenation of ethanol was performed to determine the catalytic activity and product selectivity of the different AgLi–Al $_2$ O $_3$  catalysts. Typically, 0.05 g of catalyst was used. The catalyst sample was pre-reduced in situ in flowing H $_2$  at 300 °C for 1 h prior to oxidative dehydrogenation. Ethanol was introduced into the reactor by bubbling Ar as a carrier gas through the saturator, while the saturator was kept at 45 °C to maintain the partial pressure of ethanol with WHSV of 8.4 ( $g_{ethanol} \cdot g_{cat}^{-1} \cdot h^{-1}$ ). The vaporized ethanol was mixed with oxygen feed before entering the reactor containing ethanol/oxygen molar ratio of 2. The product gas samples were analyzed by gas chromatography.

#### 3. Results and discussion

#### 3.1. Catalyst characterization

First, the desired different phases of alumina can be obtained as proven by XRD results (not shown). In fact, CHI00 exhibited the XRD patterns at  $2\theta$  degrees of 32~37, 39, 45, 61~and  $66^\circ$ , while CHI100 displayed the XRD peak at  $43^\circ$ . In addition, CHI50 exhibited the characteristic XRD patterns for both gamma and chi phases. The XRD patterns of different AgLi–Al $_2$ O $_3$  catalysts exhibited similar XRD patterns as seen from those without the presence of Ag and Li indicating well dispersion of Ag and Li. It revealed that in all catalysts the amounts of Ag were ranged between 4.7 and 4.8 wt.%, while Li contents were at 0.69 and 0.72 wt.% (ICP-OES). The surface area, pore volume and pore diameter

**Table 1**BET surface area, pore volume and pore diameter of prepared alumina and silver catalysts.

Catalysts	$A_{BET}$ $(m^2/g)$	V <sub>p</sub> (cm <sup>3</sup> /g)	D <sub>BJH</sub> (nm)
CHI00	257	0.84	8.27
AgLi-CHI00	158	0.39	7.28
CHI50	168	0.37	5.46
AgLi-CHI50	142	0.32	5.57
CHI100	137	0.55	10.42
AgLi-CHI100	109	0.42	9.21

of different  $AgLi-Al_2O_3$  catalysts obtained from the  $N_2$  physisorption are summarized in Table 1. The BET surface areas of alumina decreased from 257 to 137  $m^2/g$  with increased portion of chi phase, whereas the average pore diameter was rather similar for the different alumina samples. The pore size distribution confirmed isotherm assertion and mesoporous structure for all prepared alumina samples. The observed mesoporosity can be probably attributed to the voids from inter-connection between primary particles. It was found that the surface area of AgLi-CHI00 catalyst was much lower than that of alumina (CHI00), whereas the surface areas of AgLi-CHI50 and AgLi-CHI100 catalysts were not significantly changed. The decreased surface areas for  $AgLi-Al_2O_3$  catalysts were due to the pore blockage by the introduction of Ag and Li species.

#### 3.2. Oxidative dehydrogenation of ethanol

Oxidative dehydrogenation of ethanol over different AgLi-Al<sub>2</sub>O<sub>3</sub> catalysts was performed in order to determine the catalytic activity and product distribution. The reaction temperatures from 150 to 400 °C were studied. As shown in Fig. 1, the conversion apparently increased with increasing the reaction temperature in all catalysts. The complete conversion can be achieved at ca. 275 °C. However, to compare the catalytic activity, the ethanol conversion at 80% is considered for each catalyst. The temperature at which ethanol conversion reaches to 80% is designated as T<sub>80</sub>. At this temperature, the selectivity to acetaldehyde is high. When compared T<sub>80</sub> for all catalysts, it is shown that T<sub>80</sub> of AgLi–CHI50, AgLi-CHI00, and AgLi-CHI100 catalysts is 194, 215, and 238 °C, respectively. It indicates that the AgLi-CHI50 exhibited the highest catalytic activity, whereas the AgLi-CHI100 catalyst yields the lowest one. Acetaldehyde was a major product with the temperature up to ca. 225–250 °C as shown in Fig. 1. In addition, the fast decrease of acetaldehyde selectivity for the most active catalyst (AgLi-CHI50) was observed along with increased amounts of CO and CO<sub>2</sub>. In fact, it abruptly decreased with increased temperature (after 250 °C) due to the fast successive oxidative reaction of acetaldehyde to form CO and CO<sub>2</sub>. Thus, the suitable temperature to obtain high yield of acetaldehyde is less than ca. 250 °C. At this

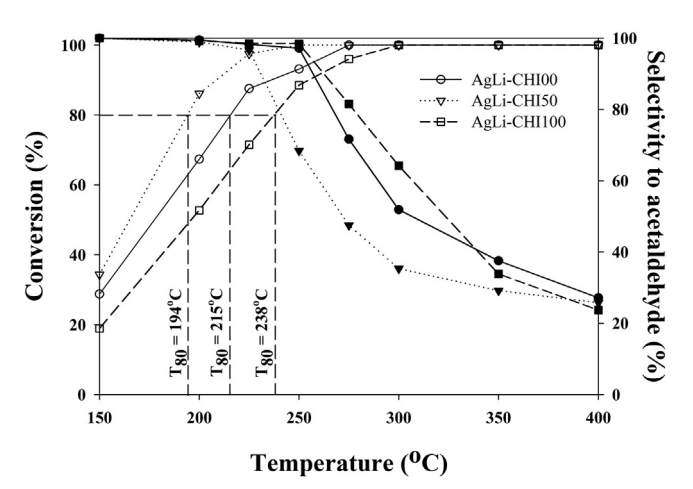


Fig. 1. Conversion and selectivity of catalysts.

stage, we can conclude that the different phase compositions of alumina can alter the catalytic properties of AgLi–Al $_2$ O $_3$  catalysts. In order to disclose a relation between the catalytic properties and distinct characteristics of catalyst such as basic sites, oxidation state of Ag species, and interaction between Ag species and alumina, more rigorous techniques are crucial.

It has been well known that the oxidative dehydrogenation of alcohols is a base-catalyzed reaction [19–21]. Thus, in order to determine the basicity of catalysts, CO<sub>2</sub>-TPD was performed. As shown in Fig. 2, it can be observed that all catalysts exhibited the CO<sub>2</sub>-TPD profiles at low temperature (ca. 100 °C). By deconvolution, the CO<sub>2</sub>-TPD peaks can be separated into two peaks, where the lower temperature peak occurred at ca. 100 °C and the higher temperature peak was around 200 to 300 °C. The CO<sub>2</sub>-TPD peak at low desorption temperature (ca. 90-100 °C) is attributed to the CO<sub>2</sub> species adsorbed on the weak basic site (OH groups) [22], whereas the medium (ca. 150 °C) and high (ca. 250 °C) desorption temperature peaks can be assigned to the CO<sub>2</sub> species interacting on the medium  $(M-O^{2-} pairs)$  and strong  $(O^{2-} ions)$ basic sites [23]. This indicated that all AgLi-Al<sub>2</sub>O<sub>3</sub> catalysts contained mostly the weak basic sites. By integrating the area below curves, it revealed that the amounts of total basic sites were in the order of AgLi-CHI50 (776  $\mu$ molCO<sub>2</sub>/g) > AgLi-CHI100 (641  $\mu$ molCO<sub>2</sub>/g) > AgLi-CHI00 (449 µmolCO<sub>2</sub>/g). It indicated that although the AgLi-CHI100 catalyst contained higher amount of total basic site than that of AgLi-CHI00 catalyst, the catalytic activity was lower. Thus, the catalytic activity should not totally depend on the total basic sites. When considering only the amounts of weak basic sites, it showed that they were in the order of CHI50 (665  $\mu$ molCO<sub>2</sub>/g) > CHI00 (384  $\mu$ molCO<sub>2</sub>/g) > CHI100 (234 µmolCO<sub>2</sub>/g), which were corresponding to the catalytic activity of catalysts. Hence, the presence of weak basic sites should play an important role on the base-catalyzed oxidative dehydrogenation. Besides the basicity of catalyst, the oxidation state of Ag essentially needs to be considered. The interaction of Ag oxide species with alumina probably has strong influence on the oxidation state of Ag oxide species during the reduction process. In order to elucidate this, the UV-visible spectroscopy was conducted for all catalysts. As seen in Fig. 3, the UVvisible spectra for silver-lithium catalysts exhibited the absorption bands around 210, 310 and 430 nm (except for the AgLi-CHI100 sample). According to the previous study [24–26], the absorption bands at ca. 200-250 and 280-315 nm were assigned to the charge transfer bands of Ag<sup>+</sup> and small charged Ag<sup> $\delta$ +</sup> clusters, respectively. The presence of absorption band at 410–460 nm corresponded to the metallic Ag<sup>0</sup> species. It can be observed that both AgLi-CHI00 and AgLi-CHI100 catalysts exhibited similar absorption bands at 210 nm indicating the presence of large amount of Ag<sup>+</sup> species. However, the observation of large amount of absorption bands around 310 nm ( $Ag_n^{\delta+}$  clusters) was

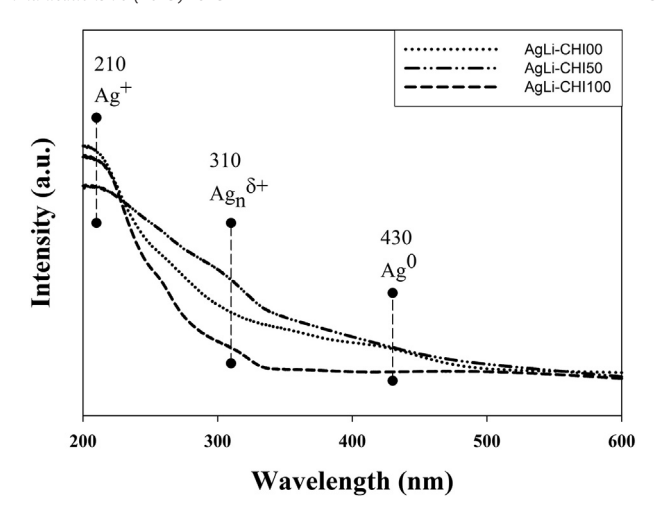


Fig. 3. UV-vis spectra of catalysts.

more pronounced for AgLi–CHI00 and AgLi–CHI50 catalysts. It is suggested that the presence of more  $Ag_n^{\delta+}$  clusters and metallic  $Ag^0$  species probably plays the crucial roles on the oxidative dehydrogenation. The amount of  $Ag_n^{\delta+}$  clusters apparently decreased in the order: AgLi–CHI50 > AgLi–CHI00 > AgLi–CHI100, which is related to the decreased activity. Previous studies also suggested that univalent  $Ag_n^{\delta+}$  ions are active states for partial oxidation of alcohol [24,27,28].

It is also interesting to determine the interaction between the Ag oxide species upon different phases of alumina. TPR is one of the most powerful techniques to evaluate such an interaction. As shown in Fig. 4, the AgLi-CHI100 catalyst exhibited instinct two strong reduction peaks, whereas the AgLi-CHI50 and AgLi-CH00 catalysts displayed one broad peak with shoulder and one narrow peak at low temperature (below 300 °C), respectively. The reduction peaks can be assigned to the overlap of two step reduction of Ag $^+$  to Ag $^{\delta\,+}$  (ca. 100 to 250 °C) and  $Ag_n^{\delta+}$  to  $Ag^0$  (ca. 250 to 330 °C). In fact, the TPR profiles for catalysts depend on various parameters such as the metal particle size distribution, metal-support interaction and porous structure resulting in different reduction behaviors [13]. However, the shift of reduction temperatures for catalysts in this study revealed that the presence of different phases of alumina also plays an important role for the reduction behavior of AgLi-Al<sub>2</sub>O<sub>3</sub> catalysts. It should be noted that due to the weak interaction between  $\mbox{\rm Ag}_n^{\delta\,+}$  species and alumina, the consecutive reduction from  $Ag_n^{\delta+}$  to  $Ag^0$  was observed at lower temperature as seen in the overlap of two step reduction for the AgLi-CHI50 and

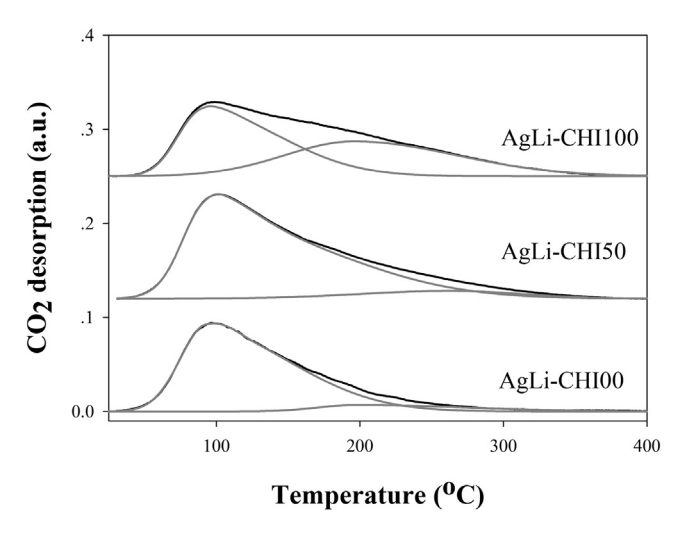


Fig. 2. CO<sub>2</sub>-TPD profiles of catalysts.

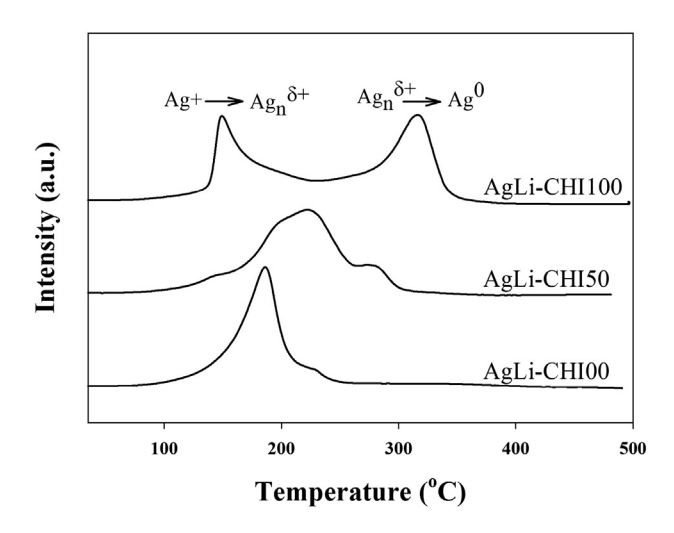
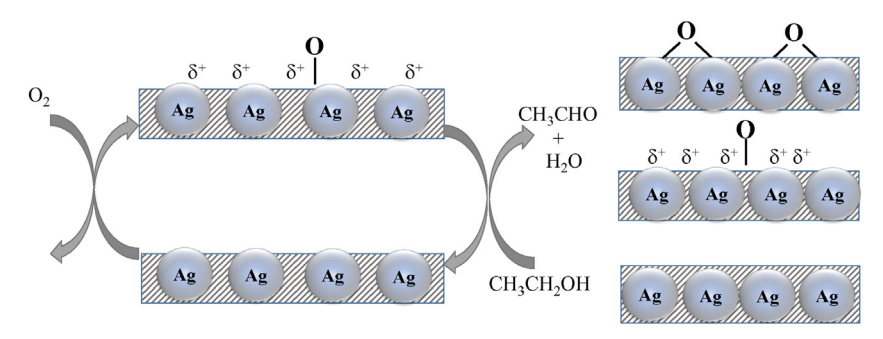


Fig. 4. TPR profiles of catalysts.



**Scheme 1.** A conceptual pathway for oxidative dehydrogenation.

AgLi–CH00 catalysts. Only AgLi–CH100 catalyst exhibited the further reduction of  $Ag_n^{\delta\,+}$  to  $Ag^0$  at higher temperature above 300 °C indicating the strong interaction resulting in lower activity. The active sites in the oxygen containing silver including the cycle of hydrogen extraction and the cycle of oxygen incorporation are shown in Scheme 1 where, oxygen is necessary to reoxidize the  $Ag^0$  to  $Ag_n^{\delta\,+}$  species, which is more active in dehydrogenation.

This is suggested that the presence of mixed chi and gamma phase in alumina can facilitate the reduction state of  $Ag^+$  species due to weaker interaction leading to increased catalytic activity for oxidative dehydrogenation. It appears that the combination of different characterization techniques such as  $CO_2$ –TPD, UV–visible spectroscopy and TPR can elucidate the change in catalytic activity of  $AgLi-Al_2O_3$  catalysts having different phase compositions of alumina. It should be noted that the amount of weak basic sites, the presence of  $Ag_n^{\delta+}$  clusters, and the interaction between Ag oxide species and alumina are crucial in determining the catalytic properties for oxidative dehydrogenation of ethanol.

#### 4. Conclusion

It reveals that the mixed phases of chi and gamma alumina in AgLi–CHI50 catalyst exhibit higher activity in oxidative dehydrogenation of ethanol than each phase alone. This can be attributed to the enhancement of weak basic sites,  $Ag_n^{\delta\,+}$  clusters, and moderate interaction of  $Ag_n^{\delta\,+}$  with alumina. With the catalysts employed, about 80% of ethanol conversion can be achieved at reaction temperature below 250 °C with high selectivity of acetaldehyde. However, increased reaction temperature from 250 to 400 °C pronouncedly causes an abrupt decrease in acetaldehyde selectivity due to the successive oxidation of acetaldehyde to CO and CO<sub>2</sub>.

#### Acknowledgment

The authors thank the Royal Golden Jubilee Ph.D. scholarship from the Thailand Research Fund (PHD52K0332, BRG5780009 and IRG5780014) and Office of the Higher Education Commission (CHE), Ratchadaphiseksomphot Endowment Fund (CU-56-654-AM) and the National Research Council of Thailand (NRCT) for the financial support of this project.

#### Appendix A. Supplementary data

Supplementary data to this article can be found online at http://dx. doi.org/10.1016/j.catcom.2015.07.020.

#### References

- R.A. Sheldon, J.K. Kochi, Metal-Catalyzed Oxidations of Organic Compounds, Academic Press, New York, 1981.
- [2] T.W. Campbell, J. Am. Chem. Soc. 86 (1964) 3404-3404.
- [3] C.R. Mistry, R.K. Mewada, V.K. Srivastava, R.V. Jasra, Characteristics of Oxidation and Oxidative Dehydrogenation Catalysts for Gas Phase Reactions: A Review, International Conference on Current Trends in Technology Institute of technology, Nirma University, Ahmedabad, 2011 1-6.
- [4] M. Kraus, I.G. Ertl, H. Knozinger, J. Weitkamp (Eds.), Handbook of Heterogeneous Catalysis, VCH, Weinheim, 1997.
- [5] C.P. Rodrigues, V.T.d. Silva, M. Schmal, Catal. Commun. 10 (2009) 1697–1701.
- 6] X.-M. Kong, L.-L. Shen, Catal. Commun. 24 (2012) 34–37.
- [7] H. Wang, W. Kong, W. Zhu, L. Wang, S. Yang, F. Liu, Catal. Commun. 50 (2014) 87–91.
- [8] K. Liu, X. Yan, P. Zou, Y. Wang, L. Dai, Catal. Commun. 58 (2015) 132–136.
- [9] Z. Qu, W. Huang, M. Cheng, X. Bao, J. Phys. Chem. B 109 (2005) 15842–15848.
- [10] X. Zhang, Z. Qu, X. Li, M. Wen, X. Quan, D. Ma, J. Wu, Sep. Purif. Technol. 72 (2010) 395–400.
- [11] Z. Qu, Y. Bu, Y. Qin, Y. Wang, Q. Fu, Appl. Catal. B Environ. 132–133 (2013) 353–362.
- [12] N. Li, F. Gaillard, Appl. Catal. B Environ. 88 (2009) 152-159.
- [13] D. Chen, Z. Qu, S. Shen, X. Li, Y. Shi, Y. Wang, Q. Fu, J. Wu, Catal. Today 175 (2011) 338–345.
- [14] T. Kharlamova, G. Mamontov, M. Salaev, V. Zaikovskii, G. Popova, V. Sobolev, A. Knyazev, O. Vodyankina, Appl. Catal. A Gen. 467 (2013) 519–529.
- [15] Y. Yu, X. Song, H. He, J. Catal. 271 (2010) 343-350.
- [16] E.A. El-Sharkawy, S.S. Al-Shihry, A.M. Youssef, Mater. Lett. 61 (2007) 2947–2951.
- [17] C. Meephoka, C. Chaisuk, P. Samparnpiboon, P. Praserthdam, Catal. Commun. 9 (2008) 546-550.
- [18] T. Glinrun, O. Mekasuwandumrong, J. Panpranot, C. Chaisuk, P. Praserthdam, React. Kinet. Mech. Catal. 100 (2010) 441–448.
- [19] W.-L. Dai, Y. Cao, L.-P. Ren, X.-L. Yang, J.-H. Xu, H.-X. Li, H.-Y. He, K.-N. Fan, J. Catal. 228 (2004) 80–91.
- [20] H. Nair, J.E. Gatt, J.T. Miller, C.D. Baertsch, J. Catal. 279 (2011) 144-154.
- [21] A.S. Blokhina, I.A. Kurzina, V.I. Sobolev, K.Y. Koltunov, G.V. Mamontov, O.V. Vodyankina, Kinet. Catal. 53 (2012) 477–481.
- [22] R. Shi, F. Wang, X. Mu, Y. Li, X. Huang, W. Shen, Catal. Commun. 11 (2009) 306–309.
- [23] J.I. Di Cosimo, V.K. Diez, M. Xu, E. Iglesia, C.R. Apesteguía, J. Catal. 178 (1998) 499–510.
- [24] A.N. Pestryakov, A.A. Davydov, Appl. Catal. A Gen. 120 (1994) 7-15.
- [25] A.N. Pestryakov, A.A. Davydov, J. Electron Spectrosc. Relat. Phenom. 74 (1995) 195–199.
- [26] N.E. Bogdanchikova, M.N. Dulin, A.A. Davydov, V.F. Anufrienko, React. Kinet. Catal. Lett. 41 (1990) 73–78.
- [27] A.N. Pestryakov, Catal. Today 28 (1996) 239–244.
- [28] A.N. Pestryakov, N.E. Bogdanchikova, A. Knop-Gericke, Catal. Today 91–92 (2004) 49–52.

Hindawi Publishing Corporation Journal of Nanomaterials Volume 2015, Article ID 519425, 11 pages http://dx.doi.org/10.1155/2015/519425



# Research Article

# A Comparative Study of Solvothermal and Sol-Gel-Derived Nanocrystalline Alumina Catalysts for Ethanol Dehydration

# Mingkwan Wannaborworn, Piyasan Praserthdam, and Bunjerd Jongsomjit

Center of Excellence on Catalysis and Catalytic Reaction Engineering, Department of Chemical Engineering, Faculty of Engineering, Chulalongkorn University, Bangkok 10330, Thailand

Correspondence should be addressed to Bunjerd Jongsomjit; bunjerd.j@chula.ac.th

Received 6 August 2015; Revised 2 November 2015; Accepted 12 November 2015

Academic Editor: Antonios Kelarakis

Copyright © 2015 Mingkwan Wannaborworn et al. This is an open access article distributed under the Creative Commons Attribution License, which permits unrestricted use, distribution, and reproduction in any medium, provided the original work is properly cited.

The ethanol dehydration to ethylene over alumina catalysts prepared by solvothermal and sol-gel methods was investigated. Also, a commercial alumina was used for comparison purposes. The results showed that the catalytic activity depends on the properties of catalyst derived from different preparation methods and reaction temperature. The alumina synthesized by solvothermal method exhibited the highest activity. This can be attributed to the higher surface area and larger amount of acid site, especially the ratio of weak/strong acid strength as determined by  $N_2$  physisorption and  $NH_3$ -TPD studies. The solvothermal-derived catalyst exhibited an excellent performance with complete ethanol conversion and 100% selectivity to ethylene at 350°C in comparison with other ones. In addition, we further studied the catalytic dehydration of alumina catalyst modified with Fe. The presence of 10 wt.% Fe decreased both conversion and ethylene selectivity. However, the acetaldehyde selectivity apparently increased. It was related to the dehydrogenation pathway that takes place on Fe species.

#### 1. Introduction

Nowadays, ethylene is one of the most important compounds for the petrochemical industry. It has been used as feedstock to produce many products such as polyethylene, polystyrene, vinyl chloride, and ethylene oxide, and, therefore, the global demand for ethylene is expected to increase with the continuous increasing of crude oil price [1, 2]. Ethylene is conventionally produced by thermal cracking of petroleum or natural gas. Since this process requires high temperature (750-900°C) and the natural resource is limited, much attention has been paid to find the alternative approach to produce ethylene. Recent studies have shown that one effective route by using biomass, especially bioethanol, is considered as the most promising way instead of using petroleum as feedstock. The ethanol dehydration provides many advantages such as lower operating temperature and green manufacturing of ethylene. Hence, the development of dehydration performance has been widely studied in both industry and academia [3-7]. The catalysts most commonly used for ethanol to ethylene are based on zeolite [8, 9], alumina [10, 11],

silica [12], and silica-alumina [13]. For HZM-5 zeolites, these catalysts possess smaller pore size and have high acid strength. Their properties cause coke deposition resulting in the deactivation of catalyst, so zeolites are inappropriate for dehydration [14, 15]. Among them, alumina is found as an efficient catalyst because of its high specific surface area, excellent thermal stability, and wide range of chemical properties, especially lower acid strength than zeolites [15, 16]. It is thus the most common catalyst used to produce ethylene.

Although several studies have been investigated on the relationship between the catalyst structures and performances in ethanol dehydration, an understanding on how the textural properties of catalyst would affect the catalytic activity has not yet been reached. Hosseini and Nikou [17] synthesized  $\gamma$ -alumina by coprecipitation method with four precipitants and used it as a catalyst for methanol dehydration. The results showed that catalyst prepared by ammonium carbonate showed higher catalytic activity compared to commercial catalyst despite having lower amount of acid sites. The high activity is related to the high surface area and pore volume of catalyst. Akarmazyan et al. [18]

investigated the methanol dehydration to dimethyl ether over commercial alumina with different physicochemical characteristics and found that the catalyst with smaller crystallite size exhibited higher catalytic activity, and it could be due to its large external surface area, thus facilitating reaction between reactant and active site. Therefore, the textural properties are important factors that need to be considered. In addition, many efforts have been made to improve the dehydration performance by adding some dopants such as titania, niobia, molybdenum oxide, and silica. Chen et al. [5] pointed out that an addition of TiO<sub>2</sub> onto alumina enhanced the ethanol conversion and ethylene selectivity. The yield of ethylene as high as 98.3% could be achieved for 10 wt.% TiO<sub>2</sub>/Al<sub>2</sub>O<sub>3</sub> catalysts at 440°C. The higher catalytic activity was consistent with the higher amount of moderate acid sites. Liu et al. [19] studied the dehydration of methanol to DME over modified  $\gamma$ -Al<sub>2</sub>O<sub>3</sub> catalysts. Results showed that Nb<sub>2</sub>O<sub>5</sub> contents significantly affect the catalytic performance of catalysts. The 10 wt.% of Nb<sub>2</sub>O<sub>5</sub> exhibited the highest activity in the low temperature due to its largest surface area. In another work by Yaripour et al. [20], the SiO<sub>2</sub> modification showed a promising way to increase a catalytic activity. Both yield and selectivity were the highest at 2 wt.% of silica, which was attributed to high surface area and high surface acidity, especially the highest weak to moderate acid site.

Recently, many investigations have been paid attention on the utilization of supported Fe catalysts. It is well known that Fe catalyst is active and often used in some important processes such as the catalytic decomposition of  $N_2O$  [21], conversion of natural gas to syn-gas [22], and the propane oxidative dehydrogenation [23]. So, in this work, we extend our study on how the Fe-modified alumina catalyst affects the catalytic activity for ethanol dehydration.

In this study, the catalytic activity of alumina catalyst prepared by solvothermal and sol-gel methods as well as commercial alumina for ethanol dehydration was investigated. The catalysts were characterized by means of XRD,  $\rm N_2$  physisorption, SEM/EDX, and NH<sub>3</sub>-TPD analyses.

## 2. Experimental

2.1. Catalyst Preparation. Alumina catalysts were synthesized according to the procedure reported previously [24, 25] and is described below.

2.1.1. Solvothermal Method. An amount of 25 g of aluminium isopropoxide (AIP) as a starting material was suspended in 100 mL of 1-butanol in a test tube and then placed in an autoclave. In the gap between the autoclave wall and test tube, 30 mL of 1-butanol was added. The autoclave was purged with nitrogen gas before heating up to 300°C and held at that temperature for 2 h. After the autoclave was cooled down to room temperature, the obtained powder was washed with methanol followed by centrifugation. Finally, the white powder product was dried at 120°C for 24 h and calcined in air at 600°C for 6 h.

2.1.2. Sol-Gel Method. The same volume of ethanol and deionized water was added to the flask. The solution was stirred under 20 rpm/min and heated to 80°C. After the solution was kept for 1 h, 15 g aluminum isopropoxide used as a precursor was added to the solution under continuous stirring. The hydrolysis step was carried out at 80°C by adding a certain volume of 10 M HCl (37%). The mixture was stirred at that temperature for 8 h. The obtained product was dried at 115°C for 24 h and further calcined in air at 550°C for 6 h to obtain white alumina catalyst.

2.2. Ethanol Dehydration Reaction. Dehydration of ethanol to ethylene was conducted in a glass fixed-bed reactor (length = 0.33 m and inner diameter = 7 mm). A glass reactor was placed into a temperature-programmed tubular furnace. All experiments were performed under atmospheric pressure and in the temperature range 200 to 400°C using a feed composition consisting of 99.95% ethanol. In a typical run, 0.05 g of alumina catalysts obtained from Sections 2.1.1 and 2.1.2 and commercial alumina (Fluka) was charged into the middle zone of reactor tube and pure ethanol as feed was stored in vaporizer. Prior to testing, the catalysts were activated at 200°C for 1 h under an argon gas flow. Ethanol was conveyed into reactor at an argon gas flow rate of 50 mL/min. The reaction was carried out at each temperature for 1 h. The dehydration products were analyzed by a gas chromatography (Shimadzu GC-14A) with a FID detector using DB-5 capillary column.

#### 2.3. Catalyst Characterization

2.3.1. X-Ray Diffraction (XRD). XRD was used to study the bulk crystalline phase of samples. The XRD pattern was performed by SIEMENS D5000 X-ray diffractometer with  $\text{CuK}_{\alpha}$  radiation. Those samples were scanned in the range of  $2\theta = 10-90$ .

2.3.2.  $N_2$ -Physisorption. The surface area and average pore volume of prepared catalysts were determined by Micromeritics ChemiSorb 2750 Pulse instrument. Measurement was performed at  $-196^{\circ}$ C and calculated according to the BET isotherm equation.

2.3.3. Scanning Electron Microscopy (SEM) and Energy Dispersive X-Ray Spectroscopy (EDX). Hitachi S-3400N model was used to determine the catalyst morphology. Their elemental distribution and composition over different catalysts were performed by Link Isis Series 300 program EDX.

2.3.4. Ammonia Temperature-Programmed Desorption ( $NH_3$ -TPD). The acid properties of all catalysts were determined by using Micromeritics ChemiSorb 2750 Pulse Chemisorption System. Under a helium gas flow, the Fe-modified and unmodified catalysts were pretreated at 550°C for 1 h. Then, the catalyst was saturated with 15%  $NH_3$ /He at 40°C for 30 min. After chemisorption step, a helium gas was flown over catalyst to remove any adsorbed molecules from catalyst active site from temperature of 40 to 500°C at heating rate

Catalyst	Surface area (m <sup>2</sup> /g)	Pore volume (cm <sup>3</sup> /g)	Pore diameter (nm)	Crystallite size (nm) <sup>a</sup>
Al-SV	215	0.770	9.33	3.78
Al-SG	152	0.221	3.46	4.78
Al-com	137	0.212	3.88	5.62

TABLE 1: Physical properties of alumina catalysts prepared by different methods.

<sup>&</sup>lt;sup>a</sup>Crystallite size of alumina: determined by XRD results using Scherrer equation.

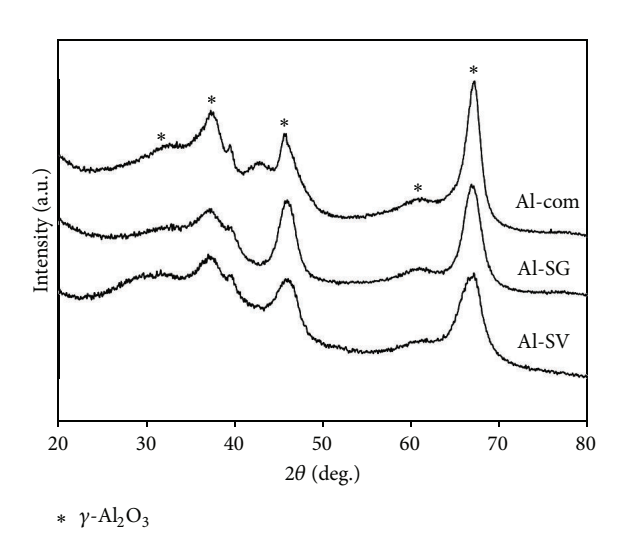


FIGURE 1: XRD patterns of different catalysts.

 $10^{\circ}$  C/min. The NH $_3$  TPD profile is a plot of the TCD signal as a function of temperature to report the amount of ammonia, which is related to catalyst acidity.

2.3.5. Thermogravimetric Analysis (TGA). TGA was performed using a TA Instrument SDT Q600 analyzer (USA). The samples of 10-20 mg and a temperature range between 30 and  $400^{\circ}\text{C}$  at  $2^{\circ}\text{C}$  min<sup>-1</sup> were used in the operation with N<sub>2</sub> UHP carrier gas.

#### 3. Results and Discussion

3.1. Catalyst Characterization. The XRD patterns of all samples are shown in Figure 1. It can be seen that the characteristic peaks at  $2\theta=37,\,46,\,61,\,$  and 67 indicating typically  $\gamma$ -phase of alumina [18, 33]. The XRD pattern of alumina synthesized by solvothermal (Al-SV) method was broad, because the crystallite sizes were very small, while the catalyst prepared by sol-gel method (Al-SG) and commercial alumina (Al-com) exhibited sharp peaks due to the presence of large crystallite size. The average crystallite size of the catalysts was calculated using Scherrer equation and shown in Table 1. The average crystallite size of alumina prepared by solvothermal method (Al-SV) was the smallest.

Figure 2 shows the nitrogen adsorption/desorption isotherms of alumina catalysts. All samples exhibited type IV isotherms, indicating they are mesoporous materials. For AlSV, the sample presented hysteresis loop of type H1, occurring at higher relative pressure ( $P/P_0 = 0.7$  to 0.9) compared with

other catalysts. It indicates larger mesopores and broad pore size distribution with uniform cylindrical shapes. Meanwhile, the isotherm for sol-gel-derived catalyst showed quite different pattern. Two inflection points and hysteresis loop moved toward lower pressure were observed. This suggests that lower porosity and cylindrical mesopores were expected for Al-SG. For Al-com, the isotherm was similar to that for Al-SG, but with slightly decreased BET surface area and pore volume [18, 34]. The observations are consistent with the value of surface area and sample porosity as shown in Table 1, in which the pore volume of Al-SV, Al-SG, and Al-com was 0.770, 0.221, and 0.212 cm<sup>3</sup>/g, respectively. The surface area of Al-SV was the highest, while the Al-com had the lowest surface area. Also, it was in accordance with those obtained from XRD analysis, where the samples with smaller crystallites exhibit higher surface area. The catalyst with small crystallite size may possess higher catalytic activity, because more active sites on large external surface area are easily reacted with reactants

The pore size distribution (PSD) calculated by BJH method is shown in Figure 3. The Al-SV sample exhibited a bimodal pore size distribution, where pore diameter was in the ranges of 7–9 nm and 23–25 nm. For Al-SG and Al-com catalysts, the samples have a narrow pore size distribution with an average pore diameter around 3 nm, confirming the pore size distribution in the mesoporous range. It can be seen that the calculated pore size distribution was in good agreement with  $\rm N_2$  isotherm as mentioned above. This finding suggests the difference in porous nature greatly affected by preparation method (sol-gel and solvothermal).

To examine the catalyst morphology, SEM technique was performed. The SEM micrographs of different catalysts are shown in Figure 4. For those catalysts synthesized by solvothermal method, agglomeration of primary particles exhibited the porous shape, where the Al-SG and Al-com catalysts consisted of agglomerated particles with primarily irregular shape. The proposed different morphology of alumina obtained from the solvothermal and sol-gel methods is illustrated in Scheme 1.

Considering the distribution of surface acidity and the strength of acid sites in different alumina catalysts,  $\rm NH_3$ -TPD was examined. Although  $\rm NH_3$ -TPD technique has some drawbacks [1], it is fast, simple, and frequently employed method to evaluate the catalyst acidity. The typical  $\rm NH_3$ -TPD profile for catalysts is shown in Figure 5. It can be seen that there were two types of acidic sites for Al-SV, Al-SG, and Alcom. The first peak observed at lower temperature ( $\approx\!250^{\circ}\rm C$ ) was due to the desorption of ammonia chemisorbed at the weak to moderate acid sites, while the higher temperature peak centered at  $400^{\circ}\rm C$  was related to the acid site with high

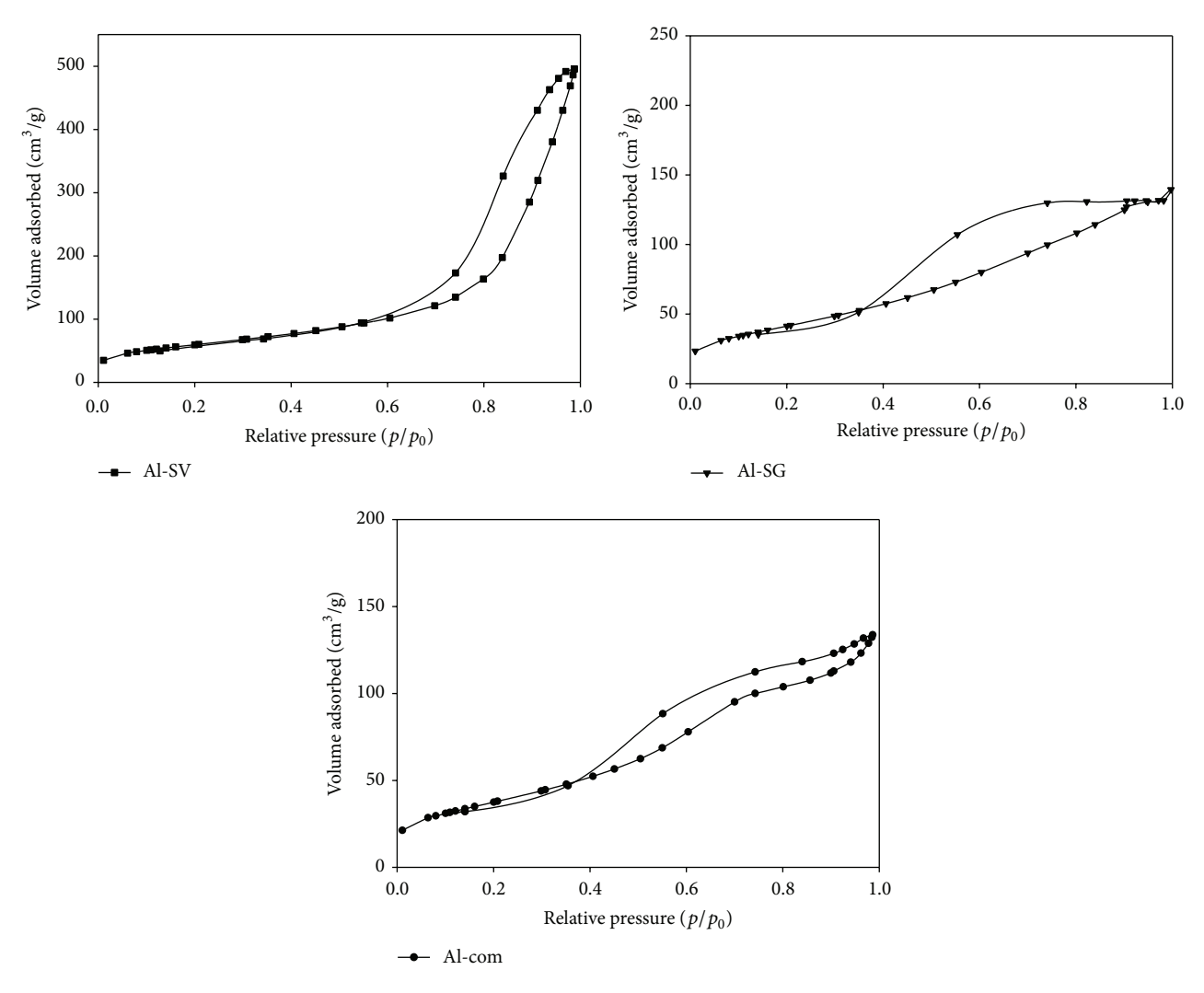


FIGURE 2: Nitrogen adsorption/desorption isotherms of different alumina catalysts.

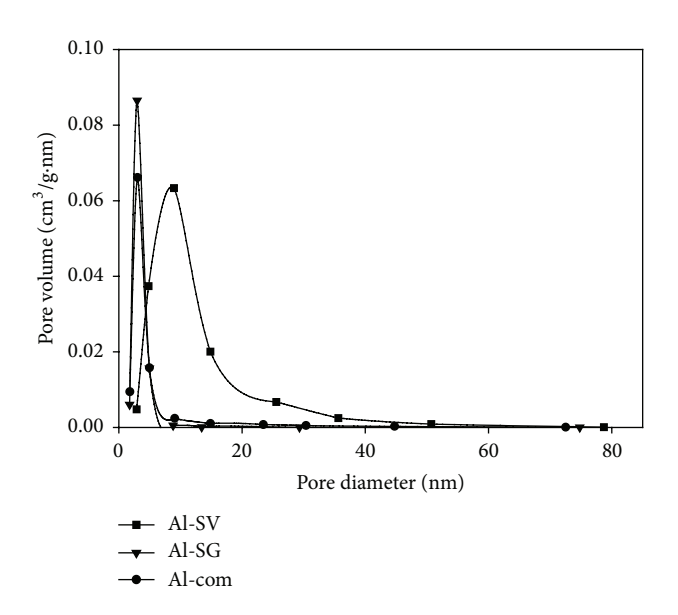


FIGURE 3: BJH pore size distribution of different alumina catalysts.

strength [35]. The amount of acid sites was determined from NH<sub>3</sub>-TPD curve by deconvolution according to the Gauss curve fitting method. The results are provided in Table 2, which demonstrated that the amount of strong acid site was higher than weak to moderate acid sites for all catalysts. The Al-SV has the highest amount of weak to moderate acid sites compared to Al-SG and Al-com. According to Chen et al. [5], higher ethylene selectivity of  $\text{TiO}_2/\gamma\text{-Al}_2\text{O}_3$  catalysts is consistent with the higher acidity. Thus, the difference in catalytic performance of these catalysts depending on the acid amount will be discussed further.

## 3.2. Catalytic Performance of Ethanol Dehydration

Effect of Reaction Temperatures. In order to study the effect of reaction temperatures on the conversion of ethanol and selectivities to ethylene, diethyl ether, and acetaldehyde, the dehydration was examined over the Al-SV catalyst in the temperature range from 200 to 400°C. As known, the product distribution of ethanol dehydration strongly depends on



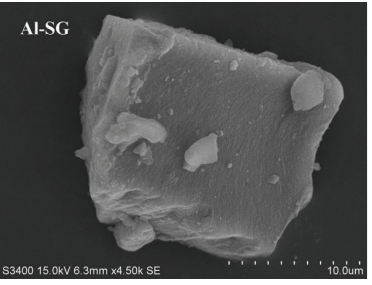
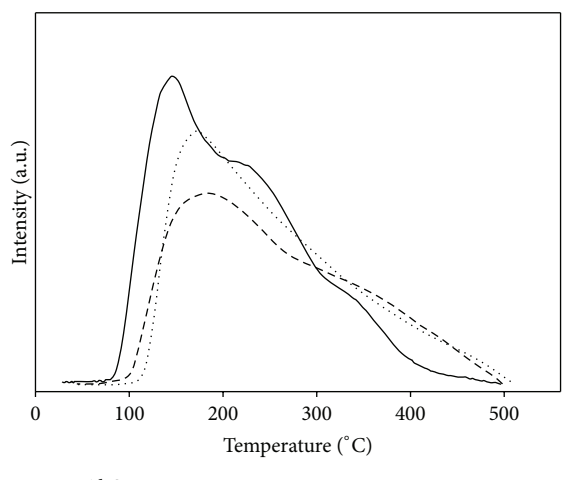




FIGURE 4: SEM images of different catalysts.



— Al-SV ····· Al-SG --- Al-com

FIGURE 5: NH<sub>3</sub>-TPD profile of the different alumina catalysts.

TABLE 2: NH<sub>3</sub>-TPD results of different alumina catalysts.

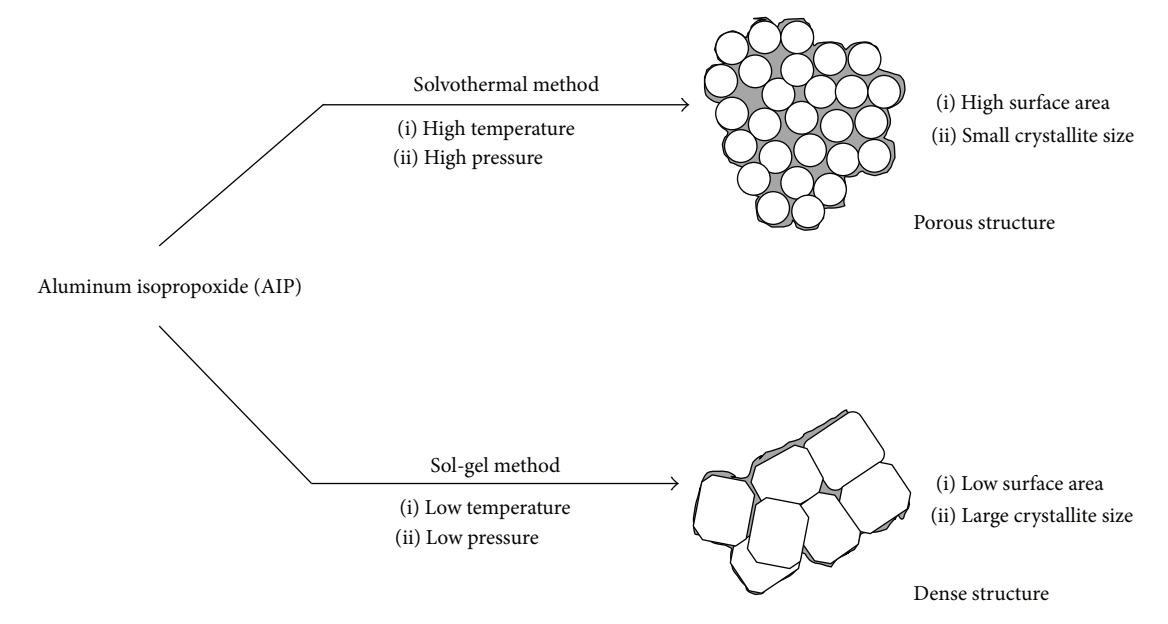
Catalyst	Number of acid sites (µmol NH <sub>3</sub> /g catalyst)					
	Weak to moderate	Strong	Weak/strong	Total		
Al-SV	360	441	0.82	801		
Al-SG	235	386	0.61	621		
Al-com	256	442	0.58	698		

the reaction temperatures. Low temperatures favor the diethyl ether production, while the ethylene formation occurs at high temperature. It is evident from Figure 6 that the conversion increased with an increase in the reaction temperature. The Al-SV exhibited the highest conversion and ethylene selectivity of 100% at 350°C and kept constant at 400°C. The enhanced catalytic activity is related to the reaction pathway. Generally, for ethylene production through ethanol dehydration, there are two competitive pathways during reaction. The main path involves the formation of ethylene. This reaction occurring via intramolecular is endothermic. The second one, inter-molecular dehydration to diethyl ether, is exothermic [5, 15, 26]. The results of activity test in Figure 6 show that when increasing the reaction temperature, the selectivity to ethylene continuously increased,

whereas the decrease in diethyl ether selectivity was evident over selected catalyst. Chen et al. [5] suggested that at low temperature, not only do the catalysts have poor activities, but also the selectivity of ethylene is low due to a large amount of ethanol that was converted to diethyl ether product. In this research, the reaction temperature of 350°C was selected as the optimum temperature.

Effect of Preparation Methods. In order to investigate the influence of preparation methods on ethanol dehydration, alumina synthesized by solvothermal and sol-gel methods as well as commercial catalysts was studied. The conversion of ethanol over all catalysts is presented in Figure 7. The conversion was found to be in the order Al-SV > Al-SG > Al-com. The Al-SV showed the best performance for dehydration, giving complete conversion at 350°C compared to the other ones. From results of NH<sub>3</sub>-TPD analysis, it seems that there is a relationship between the activity and the ratio of weak acid sites to strong acid sites of alumina catalysts. The sample possessing high ratio of weak to strong acid sites exhibited high catalytic performance on dehydration. The higher activity of Al-SV can be attributed to its higher surface area and higher amount surface acid sites, especially the highest ratio of weak/strong acid strength. Similar trend was found by Hosseini and Nikou [17]; catalyst with high surface area exhibited high activity due to more active sites on large surface area directly to be exposed to ethanol reactant. Xin et al. [1] also reported that the ethanol conversion to ethylene is mainly related to the weak to moderate acid site, while the side reaction such as oligomerization, dehydrocyclization, and the reaction producing higher olefin compounds occurred on the strong acid strength.

In addition, it is generally accepted that ethanol dehydration is an acid-catalyzed reaction. Either Brönsted acid site or Lewis acid site is believed to play an important role in catalytic activity. Different reaction mechanisms of ethanol to ethylene involved the acid sites. One ethanol molecule initially adsorbs on the Brönsted acid site of catalyst and then forms an ethoxide surface species. Subsequently, the ethoxide undergoes deprotonation, losing a proton to Brönsted acid site and forming the ethylene product. On the other hand, the reaction between ethoxide and another ethanol molecule yields diethyl ether (side product). These observations deduced the ethylene selectivity mainly contributed to the Brönsted acidic site [1, 36, 37]. In order to support active



SCHEME 1: Proposed different morphology of alumina obtained from the solvothermal and sol-gel methods.

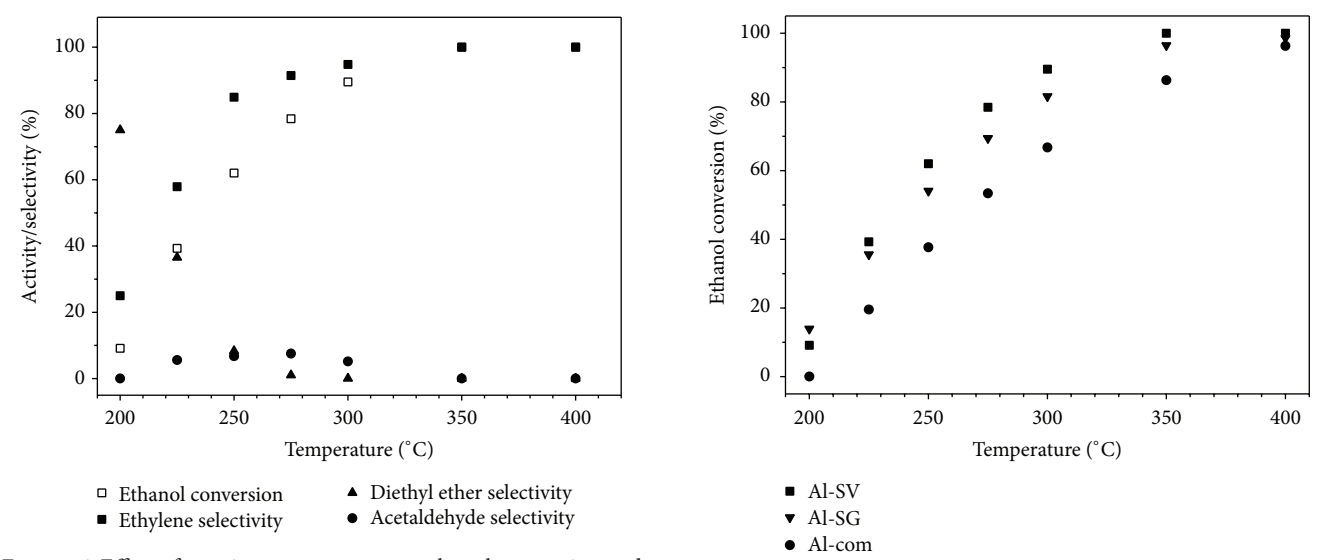


FIGURE 6: Effect of reaction temperature on ethanol conversion and product selectivity over the Al-SV catalyst (reaction condition:  $T=200-400^{\circ}$ C, WHSV =  $8.4~\rm h^{-1}$ , and catalyst weight =  $50~\rm mg$ ).

FIGURE 7: The conversion of ethanol over different alumina catalysts (reaction condition:  $T = 200-400^{\circ}$  C, WHSV =  $8.4 \,\mathrm{h}^{-1}$ , and catalyst weight =  $50 \,\mathrm{mg}$ ).

Brönsted acidic sites, the dehydration of ethanol over pure siliceous silicate-1 was investigated [1]. They reported that a very low activity with ethanol conversion around 2% was observed. Since the sample consists mainly of Si-OH, there is not Al atom in framework. Therefore, it clearly suggested that the Brönsted acid sites play a crucial role in the ethanol conversion and the formation of ethylene. However, Pan et al. [38] observed the opposite trend with the Lewis acid site. They inferred that the near absence of the acidic Brönsted and the presence of strong Lewis site apparently enhanced the ethylene selectivity. In fact, it should be noted that the NH $_3$ -TPD does not provide the nature of surface Brönsted

and Lewis acid site on catalyst surface. Thus, in this study, the types of acidic site (Brönsted or Lewis sites) are not further discussed here. However, it is generally accepted that the ethanol conversion to ethylene occurs on weak acid sites, while the oligomerization and the alcohol transformation to higher hydrocarbon correspond to strong acid strength [39, 40].

From the product selectivity presented in Figures 8, 9, and 10, it was obvious that the Al-SV was able to dehydrate ethanol to ethylene with 100% selectivity, while at 350°C ethylene selectivity was only 87% and 65% for Al-SG and Al-com, respectively. Table 3 summarizes the catalytic ability

Catalyst	Surface area (m²/g)	Amount of catalyst	Space velocity (h <sup>-1</sup> )	Reaction temperature (°C)	Ethylene yield (%)	References
Al-SV	215	0.05 g	WHSV 8.4	250-350	53-100	This work
H-ZSM-5 (Si/Al = 28)	425	0.2 g	WHSV 0.422	200	9-13	[1]
$TiO_2/\gamma$ - $Al_2O_3$	187	1.15 mL	LHSV 26-104	360-550	91–99	[5]
Mn-SAPO-34	473	2.0 g	WHSV 2.0	340	97.8	[26]
$H_3PO_4\cdot 12WO_3\cdot xH_2O$	104	10 g	WHSV 1.0	250	68	[27]
Tungstophosphoric acid/MCM-41	183	0.2 g	WHSV 2.9	300	97.9	[28]
P/H-ZSM-5 (Si/Al = 12.18)	160	1.5 g	WHSV 3.0	280-440	31–100	[29]
$Ag_3PW_{12}O_{40}\cdot 3H_2O$	n.a.	0.5 mL	GHSV 6000	220	99.2	[30]
$Fe_2O_3$	40	10 mL	LHSV 2.85	500	63.4	[31]

3.0 mL

3.0 mL

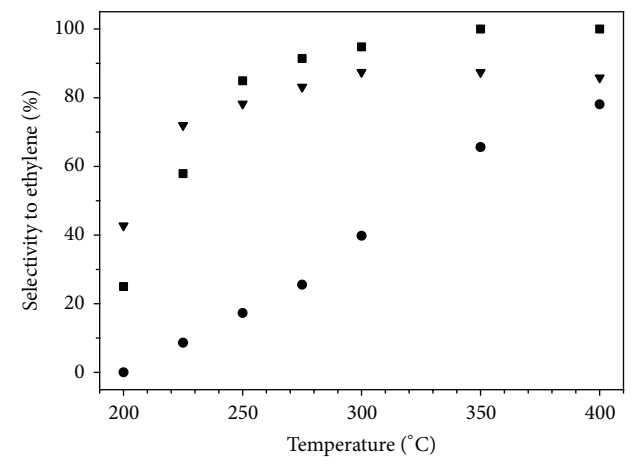
LHSV 3.0

LHSV 3.0

TABLE 3: Summary of catalysts for ethylene synthesis and their catalytic ability.

Commercial Al<sub>2</sub>O<sub>3</sub>

H-ZSM-5 (Si/Al = 25)



190

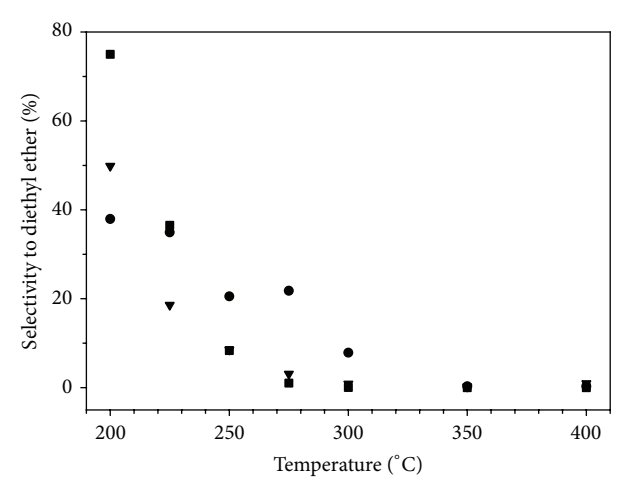
295

- Al-SV
- ▼ Al-SG
- Al-com

FIGURE 8: The selectivity of ethylene over different alumina catalysts (reaction condition:  $T=200-400^{\circ}$  C, WHSV =  $8.4~\rm h^{-1}$ , and catalyst weight =  $50~\rm mg$ ).

for ethanol dehydration to ethylene over various catalysts reported so far. It was obvious that Al-SV is comparable to those of typical and modified catalysts. Thus, the Al-SV is expected to be applied for the ethanol dehydration to ethylene.

To study the amount of coke deposition on catalyst after reaction, TGA measurement was performed. As seen in Figure 11, the weight loss below 150°C was attributed to the removal of physically adsorbed water. The weight loss at higher temperature (200–800°C) was attributed to the burning of coke deposited on the used sample surface. It was observed that the amount of coke present on various catalysts was in the order of Al-SV (4.0 wt.%) > Al-SG (3.9 wt.%) > Al-com (2.6 wt.%), corresponding to the amount of acidity as determined by NH $_3$ -TPD analysis.



450

450

[32]

[32]

78.1

93.6

- Al-SV
- ▼ Al-SG
- Al-com

FIGURE 9: The selectivity of diethyl ether over different alumina catalysts (reaction condition:  $T = 200-400^{\circ}$  C, WHSV =  $8.4 \, h^{-1}$ , and catalyst weight =  $50 \, \text{mg}$ ).

Accordingly, the textural and acidic properties, the amount of acidic sites, and distribution of acid strength as well as the reaction temperature are important parameters that influenced the catalytic activity. It is thus recommended that alumina catalyst prepared by solvothermal method (Al-SV) was the most suitable catalyst for using in the production of ethylene from ethanol and 350°C was selected as the optimum temperature.

In addition, we extend our study on how the Fe-modified alumina catalyst affects the catalytic activity for ethanol dehydration. We selected solvothermal alumina impregnated with Fe as a catalyst and denoted it as Fe/Al-SV.

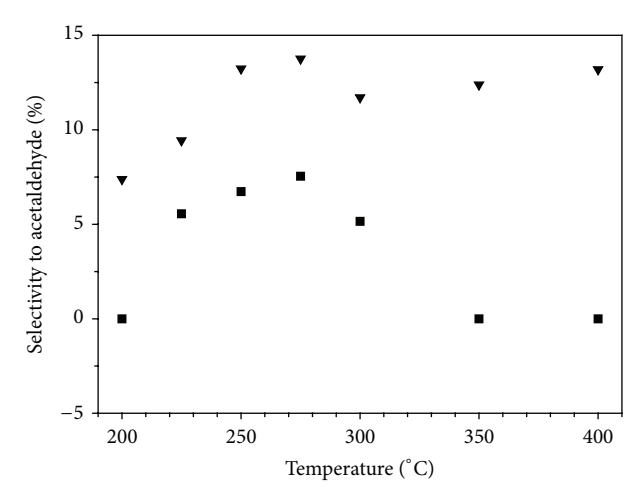
The XRD pattern exhibited the presence of Fe characterized by peaks at 24°, 33°, 35.5°, 49°, 54°, and 62°. The average crystallite size calculated by Scherrer equation was 4.43 nm.

<sup>\*</sup>n.a. = not applicable.

Sample	Number of acid sites (µmol NH <sub>3</sub> /g catalyst)		Ethanol conversion <sup>a</sup> (%)	Selectivity <sup>a</sup> (%)		
	Weak to moderate	Strong	Ethanol conversion (70)	Ethylene	Diethyl ether	Acetaldehyde
Al-SV	360	441	100.0	100.0	0.0	0.0
Fe/Al-SV	281	1147	75.2	45.6	2.1	52.3

TABLE 4: NH<sub>3</sub>-TPD data and catalytic activity of Fe-modified alumina catalyst.

 $<sup>^{</sup>a}T = 350^{\circ}\text{C}, P = 1 \text{ atm}.$ 



- Al-SV
- ▼ Al-SG
- Al-com

FIGURE 10: The selectivity of acetaldehyde over different alumina catalysts (reaction condition:  $T = 200-400^{\circ}$  C, WHSV =  $8.4 \, h^{-1}$ , and catalyst weight =  $50 \, \text{mg}$ ).

The crystallite size increased after modified with Fe. For the BET surface areas, it can be observed that the addition of Fe leads to a decrease in the surface area. The result changes from 215 to  $145 \, \text{m}^2/\text{g}$ , which is due to the pore blockage with Fe. It is consistent with pore size distribution results that it showed a slight shift of pore diameter to small size obtained for Fe/Al-SV.

For  $\mathrm{NH_3}$ -TPD results, after the introduction of Fe onto alumina catalyst, the first peak of  $\mathrm{NH_3}$ -TPD slightly shifted to higher temperature, while the second peak became broader. It suggested that the weak to moderate acid sites were decreased, but the amount of strong acid strength was increased. The results were probably due to the changes made by alternation of some strong acidic sites to the weak to moderate ones in modified catalysts [20]. A similar result was carried out by Li et al. [41], which reported that the presence of  $\mathrm{Mn^{4+}}$  in molecular sieve catalyst caused the higher strong acidity, but lower weak acid site.

Table 4 displays the catalytic dehydration of Al-SV and Fe/Al-SV catalysts under the optimized reaction temperature ( $T=350^{\circ}$ C). It is evident that the activity of Al-SV is higher than Fe-modified catalyst, which is in good agreement with the results of N<sub>2</sub> adsorption-desorption and NH<sub>3</sub>-TPD techniques. The Al-SV has high surface area and possesses large amount of weak to moderate acid sites. This shows

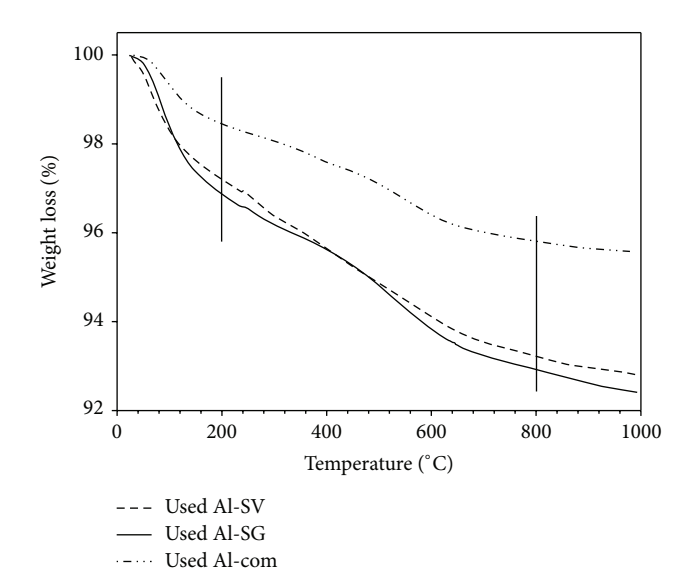
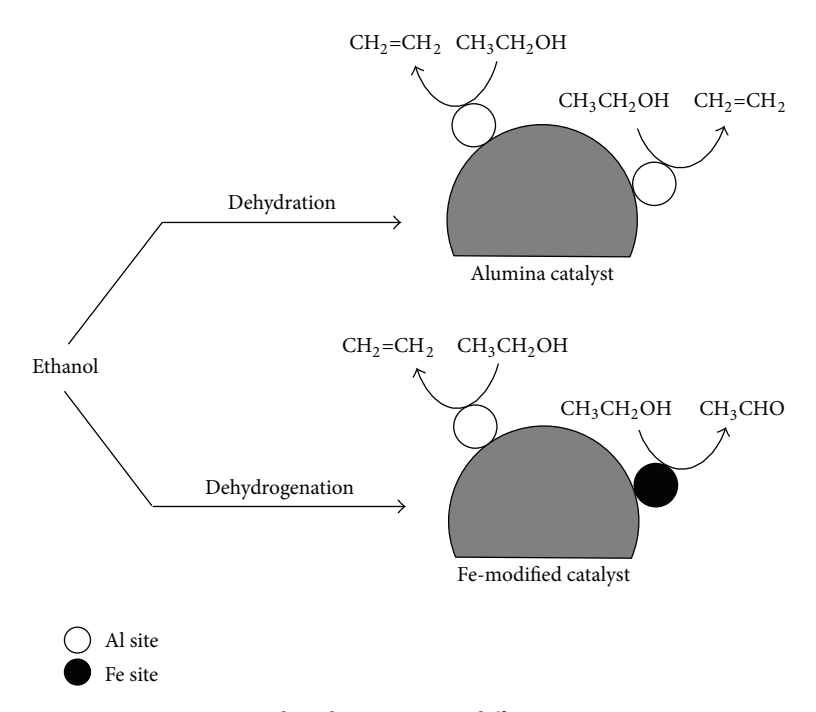


FIGURE 11: TGA curves of the different alumina catalysts.

the importance of textural property and distribution of acid sites as well as the amount of acid site in catalysts. Interestingly, the Fe/Al-SV showed higher selectivity to acetaldehyde compared to unmodified one. An improvement in acetaldehyde selectivity is related to the dehydrogenation pathway promoted by Fe. According to the work done by Li et al. [41], they found that the formation of acetaldehyde over MnO<sub>x</sub>/molecular sieve catalyst involves (i) the adsorption of ethanol on manganese cations as Lewis acid sites forming ethoxide species; (ii) hydrogen atom of ethoxide abstraction by lattice oxygen and forming acetaldehyde product; (iii) a reoxidation process at metal site and the replenishment of lattice oxygen vacancies to complete catalytic cycle. Also, Michorczyk et al. [42] revealed that the dehydrogenation of propane proceeded via oxidative pathway over catalyst. Propane is oxidized to propene by lattice oxygen from the iron oxide phase (Fe<sub>2</sub>O<sub>3</sub> or Fe<sub>3</sub>O<sub>4</sub>). However, in the oxygenfree experiment, acetaldehyde was found to a small extent because of the limited supply of oxygen. Based on these results and previous studies, a plausible reaction for the formation of acetaldehyde is proposed in Scheme 2.

Although the addition of Fe decreased the ethylene selectivity, the enhanced selectivity to acetaldehyde, which is a valuable compound in petrochemical industry, was obtained. The results in this research suggested a new chance to produce acetaldehyde. The ethanol reaction on alumina catalyst with and without Fe modification is demonstrated in Scheme 3.

SCHEME 2: Proposed reaction for acetaldehyde formation over Fe-modified catalyst.



SCHEME 3: Ethanol reaction over different active sites.

# 4. Conclusion

The catalytic performance for ethanol dehydration over alumina catalysts prepared by solvothermal and sol-gel methods as well as commercial catalyst was investigated. It revealed that solvothermal-derived alumina showed the highest catalytic activity among other ones because it has the highest surface area and highest ratio of weak acid sites to strong acid sites. From  $N_2$  adsorption-desorption and  $NH_3$ -TPD results, it can be concluded that these textural and

acidic properties significantly affect catalytic dehydration. In addition, in the part of Fe modification, the Fe loading was found to improve the acetaldehyde selectivity. It is due to the ethanol dehydrogenation over Fe species.

# **Conflict of Interests**

The authors declare that there is no conflict of interests regarding the publication of this paper.

# Acknowledgments

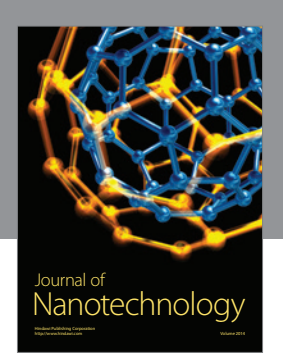
The authors thank the Thailand Research Fund (BRG5780009 and IRG5780014), National Research University Project, Ratchadaphiseksomphot Endowment Fund (2015) of CU (CU-58-027-AM), and the National Research Council of Thailand (NRCT) for the financial support of this project. They also would like to thank Postdoctoral Scholarship for supporting this research.

## References

- [1] H. Xin, X. Li, Y. Fang et al., "Catalytic dehydration of ethanol over post-treated ZSM-5 zeolites," *Journal of Catalysis*, vol. 312, pp. 204–215, 2014.
- [2] E. Aghaei and M. Haghighi, "Effect of crystallization time on properties and catalytic performance of nanostructured SAPO-34 molecular sieve synthesized at high temperatures for conversion of methanol to light olefins," *Powder Technology*, vol. 269, pp. 358–370, 2015.
- [3] K. Ramesh, L. M. Hui, Y.-F. Han, and A. Borgna, "Structure and reactivity of phosphorous modified H-ZSM-5 catalysts for ethanol dehydration," *Catalysis Communications*, vol. 10, no. 5, pp. 567–571, 2009.
- [4] D. Varisli, T. Dogu, and G. Dogu, "Ethylene and diethyl-ether production by dehydration reaction of ethanol over different heteropolyacid catalysts," *Chemical Engineering Science*, vol. 62, no. 18–20, pp. 5349–5352, 2007.
- [5] G. Chen, S. Li, F. Jiao, and Q. Yuan, "Catalytic dehydration of bioethanol to ethylene over TiO<sub>2</sub>/γ-Al<sub>2</sub>O<sub>3</sub> catalysts in microchannel reactors," *Catalysis Today*, vol. 125, no. 1-2, pp. 111–119, 2007.
- [6] L.-P. Wu, X.-J. Li, Z.-H. Yuan, and Y. Chen, "The fabrication of TiO<sub>2</sub>-supported zeolite with core/shell heterostructure for ethanol dehydration to ethylene," *Catalysis Communications*, vol. 11, no. 1, pp. 67–70, 2009.
- [7] M. Mokhtar, S. N. Basahel, and T. T. Ali, "Ethanol to hydrocarbons using silver substituted polyoxometalates: physicochemical and catalytic study," *Journal of Industrial and Engineering Chemistry*, vol. 20, no. 1, pp. 46–53, 2014.
- [8] J. Bi, X. Guo, M. Liu, and X. Wang, "High effective dehydration of bio-ethanol into ethylene over nanoscale HZSM-5 zeolite catalysts," *Catalysis Today*, vol. 149, no. 1-2, pp. 143–147, 2010.
- [9] Y. Han, C. Lu, D. Xu, Y. Zhang, Y. Hu, and H. Huang, "Molybdenum oxide modified HZSM-5 catalyst: surface acidity and catalytic performance for the dehydration of aqueous ethanol," Applied Catalysis A: General, vol. 396, no. 1-2, pp. 8–13, 2011.
- [10] E. A. El-Katatny, S. A. Halawy, M. A. Mohamed, and M. I. Zaki, "Recovery of ethene-selective  ${\rm FeO}_x/{\rm Al_2O_3}$  ethanol dehydration catalyst from industrial chemical wastes," *Applied Catalysis A: General*, vol. 199, no. 1, pp. 83–92, 2000.
- [11] S. Alamolhoda, M. Kazemeini, A. Zaherian, and M. R. Zakerinasab, "Reaction kinetics determination and neural networks modeling of methanol dehydration over nano γ-Al<sub>2</sub>O<sub>3</sub> catalyst," *Journal of Industrial and Engineering Chemistry*, vol. 18, no. 6, pp. 2059–2068, 2012.
- [12] Y. Matsumura, K. Hashimoto, and S. Yoshida, "Selective dehydrogenation of ethanol over highly dehydrated silica," *Journal of Catalysis*, vol. 117, no. 1, pp. 135–143, 1989.
- [13] R. Takahashi, S. Sato, T. Sodesawa, K. Arai, and M. Yabuki, "Effect of diffusion in catalytic dehydration of alcohol over

- silica-alumina with continuous macropores," *Journal of Catalysis*, vol. 229, no. 1, pp. 24–29, 2005.
- [14] A. T. Aguayo, A. G. Gayubo, A. Atutxa, M. Olazar, and J. Bilbao, "Catalyst deactivation by coke in the transformation of aqueous ethanol into hydrocarbons. Kinetic modeling and acidity deterioration of the catalyst," *Industrial & Engineering Chemistry Research*, vol. 41, no. 17, pp. 4216–4224, 2002.
- [15] Q. Sheng, K. Ling, Z. Li, and L. Zhao, "Effect of steam treatment on catalytic performance of HZSM-5 catalyst for ethanol dehydration to ethylene," *Fuel Processing Technology*, vol. 110, pp. 73– 78, 2013.
- [16] G. Moradi, F. Yaripour, H. Abbasian, and M. Rahmanzadeh, "Intrinsic reaction rate and the effects of operating conditions in dimethyl ether synthesis from methanol dehydration," *Korean Journal of Chemical Engineering*, vol. 27, no. 5, pp. 1435–1440, 2010.
- [17] S. Y. Hosseini and M. R. K. Nikou, "Investigation of different precipitating agents effects on performance of γ-Al<sub>2</sub>O<sub>3</sub> nanocatalysts for methanol dehydration to dimethyl ether," *Journal of Industrial and Engineering Chemistry*, vol. 20, no. 6, pp. 4421– 4428, 2014.
- [18] S. S. Akarmazyan, P. Panagiotopoulou, A. Kambolis, C. Papadopoulou, and D. I. Kondarides, "Methanol dehydration to dimethylether over Al<sub>2</sub>O<sub>3</sub> catalysts," *Applied Catalysis B: Environmental*, vol. 145, pp. 136–148, 2014.
- [19] D. Liu, C. Yao, J. Zhang, D. Fang, and D. Chen, "Catalytic dehydration of methanol to dimethyl ether over modified  $\gamma$ -Al<sub>2</sub>O<sub>3</sub> catalyst," *Fuel*, vol. 90, no. 5, pp. 1738–1742, 2011.
- [20] F. Yaripour, Z. Shariatinia, S. Sahebdelfar, and A. Irandoukht, "The effects of synthesis operation conditions on the properties of modified  $\gamma$ -alumina nanocatalysts in methanol dehydration to dimethyl ether using factorial experimental design," *Fuel*, vol. 139, pp. 40–50, 2015.
- [21] G. Moretti, G. Fierro, G. Ferraris, G. B. Andreozzi, and V. Naticchioni, "N<sub>2</sub>O decomposition over [Fe]-MFI catalysts: influence of the FexOy nuclearity and the presence of framework aluminum on the catalytic activity," *Journal of Catalysis*, vol. 318, pp. 1–13, 2014.
- [22] K. Aasberg-Petersen, I. Dybkjær, C. V. Ovesen, N. C. Schjødt, J. Sehested, and S. G. Thomsen, "Natural gas to synthesis gas catalysts and catalytic processes," *Journal of Natural Gas Science and Engineering*, vol. 3, no. 2, pp. 423–459, 2011.
- [23] J. Pérez-Ramírez and A. Gallardo-Llamas, "Impact of the preparation method and iron impurities in Fe-ZSM-5 zeolites for propylene production via oxidative dehydrogenation of propane with N<sub>2</sub>O," Applied Catalysis A: General, vol. 279, no. 1-2, pp. 117–123, 2005.
- [24] M. S. M. Yusoff and M. Muslimin, "Synthesis of alumina using the solvothermal method," *Malaysian Journal of Analytical Sciences*, vol. 11, no. 1, pp. 262–268, 2007.
- [25] S. Saha, "Preparation of alumina by sol-gel process, its structures and properties," *Journal of Sol-Gel Science and Technology*, vol. 3, no. 2, pp. 117–126, 1994.
- [26] Y. Chen, Y. Wu, L. Tao et al., "Dehydration reaction of bioethanol to ethylene over modified SAPO catalysts," *Journal of Industrial and Engineering Chemistry*, vol. 16, no. 5, pp. 717–722, 2010.
- [27] V. V. Bokade and G. D. Yadav, "Heteropolyacid supported on montmorillonite catalyst for dehydration of dilute bio-ethanol," *Applied Clay Science*, vol. 53, no. 2, pp. 263–271, 2011.
- [28] A. Ciftci, D. Varisli, K. Cem Tokay, N. Asli Sezgi, and T. Dogu, "Dimethyl ether, diethyl ether & ethylene from alcohols over

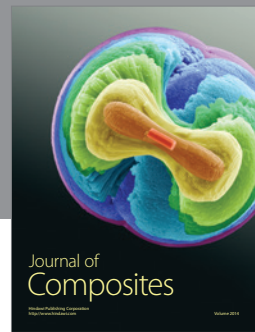
- tungstophosphoric acid based mesoporous catalysts," *Chemical Engineering Journal*, vol. 207-208, pp. 85–93, 2012.
- [29] D. Zhang, R. Wang, and X. Yang, "Effect of P content on the catalytic performance of P-modified HZSM-5 catalysts in dehydration of ethanol to ethylene," *Catalysis Letters*, vol. 124, no. 3-4, pp. 384–391, 2008.
- [30] J. Gurgul, M. Zimowska, D. Mucha, R. P. Socha, and L. Matachowski, "The influence of surface composition of  ${\rm Ag_3PM_{12}O_{40}}$  and  ${\rm Ag_3PMo_{12}O_{40}}$  salts on their catalytic activity in dehydration of ethanol," *Journal of Molecular Catalysis A: Chemical*, vol. 351, pp. 1–10, 2011.
- [31] T. Zaki, "Catalytic dehydration of ethanol using transition metal oxide catalysts," *Journal of Colloid and Interface Science*, vol. 284, no. 2, pp. 606–613, 2005.
- [32] X. Zhang, R. Wang, X. Yang, and F. Zhang, "Comparison of four catalysts in the catalytic dehydration of ethanol to ethylene," *Microporous and Mesoporous Materials*, vol. 116, no. 1–3, pp. 210–215, 2008.
- [33] J. Khom-in, P. Praserthdam, J. Panpranot, and O. Mekasuwandumrong, "Dehydration of methanol to dimethyl ether over nanocrystalline  $Al_2O_3$  with mixed  $\gamma$  and  $\chi$ -crystalline phases," *Catalysis Communications*, vol. 9, no. 10, pp. 1955–1958, 2008.
- [34] G. Leofanti, M. Padovan, G. Tozzola, and B. Venturelli, "Surface area and pore texture of catalysts," *Catalysis Today*, vol. 41, no. 1–3, pp. 207–219, 1998.
- [35] X. Liu, W.-Z. Lang, L.-L. Long, C.-L. Hu, L.-F. Chu, and Y.-J. Guo, "Improved catalytic performance in propane dehydrogenation of PtSn/γ-Al<sub>2</sub>O<sub>3</sub> catalysts by doping indium," *Chemical Engineering Journal*, vol. 247, pp. 183–192, 2014.
- [36] W. R. Moser, R. W. Thompson, C.-C. Chiang, and H. Tong, "Silicon-rich H-ZSM-5 catalyzed conversion of aqueous ethanol to ethylene," *Journal of Catalysis*, vol. 117, no. 1, pp. 19–32, 1989.
- [37] L. Silvester, J.-F. Lamonier, J. Faye et al., "Reactivity of ethanol over hydroxyapatite-based Ca-enriched catalysts with various carbonate contents," *Catalysis Science & Technology*, vol. 5, pp. 2994–3006, 2015.
- [38] Q. Pan, A. Ramanathan, W. Kirk Snavely, R. V. Chaudhari, and B. Subramaniam, "Intrinsic kinetics of ethanol dehydration over Lewis acidic ordered mesoporous silicate, Zr-KIT-6," *Topics in Catalysis*, vol. 57, pp. 1407–1411, 2014.
- [39] K. K. Ramasamy and Y. Wang, "Catalyst activity comparison of alcohols over zeolites," *Journal of Energy Chemistry*, vol. 22, no. 1, pp. 65–71, 2013.
- [40] M. Zhang and Y. Yu, "Dehydration of ethanol to ethylene," Industrial & Engineering Chemistry Research, vol. 52, no. 28, pp. 9505–9514, 2013.
- [41] J. Li, R. Wang, and J. Hao, "Role of lattice oxygen and lewis acid on ethanol oxidation over OMS-2 catalyst," *The Journal of Physical Chemistry C*, vol. 114, no. 23, pp. 10544–10550, 2010.
- [42] P. Michorczyk, P. Kuśtrowski, L. Chmielarz, and J. Ogonowski, "Influence of redox properties on the activity of iron oxide catalysts in dehydrogenation of propane with CO<sub>2</sub>," *Reaction Kinetics and Catalysis Letters*, vol. 82, no. 1, pp. 121–130, 2004.









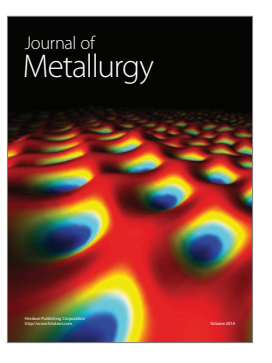


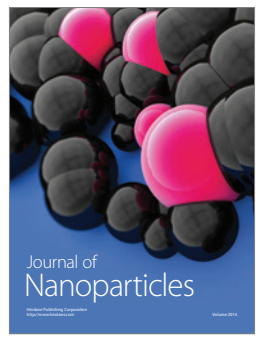


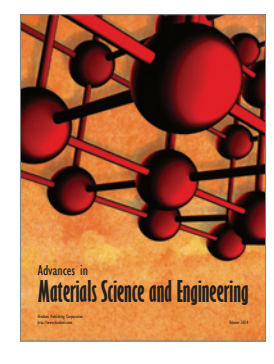




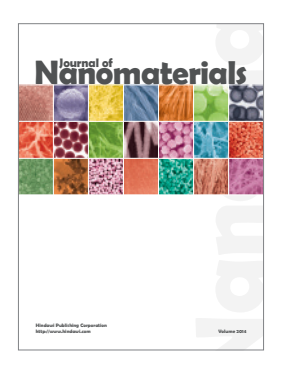
Submit your manuscripts at http://www.hindawi.com









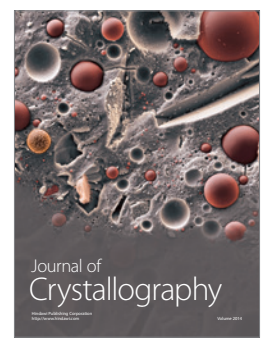


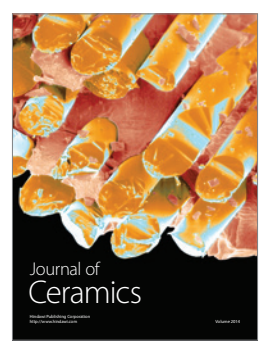














# ENGINEERING JOURNAL

Article

# A Comparative Study of Different Al-Based Solid Acid Catalysts for Catalytic Dehydration of Ethanol

# Tanutporn Kamsuwan and Bunjerd Jongsomjit\*

Center of Excellence on Catalysis and Catalytic Reaction Engineering, Department of Chemical Engineering, Faculty of Engineering, Chulalongkorn University, Bangkok 10330, Thailand \*E-mail: bunjerd.j@chula.ac.th (Corresponding author)

**Abstract.** In this present study, the catalytic dehydration of ethanol over three different Al-based solid acid catalysts including H-beta zeolite (HBZ), modified H-beta zeolite with γ-Al<sub>2</sub>O<sub>3</sub> (Al-HBZ) and mixed γ- χ phase of Al<sub>2</sub>O<sub>3</sub> (M-Al) catalysts was investigated. The ethanol dehydration reaction was performed at temperature range of 200 to 400°C. It revealed that all catalysts exhibited higher ethanol conversion with increased temperatures. At low temperatures (ca. 200 to 250°C), diethyl ether (DEE) was obtained as a major product for all catalysts. However, with increased temperatures (ca. 300 to 400°C), ethylene was a major product. Among all catalysts, HBZ exhibited the highest ethanol conversion giving the ethylene yield of 99.4% at 400°C. This can be attributed to the largest amount of weak acid sites present in HBZ, which is related to the Brønsted acid. It should be mentioned that HBZ also rendered the highest catalytic activity for every reaction temperature. As the results, HBZ catalyst is promising to produce ethylene and DEE from ethanol, which is considered as cleaner technology.

**Keywords:** Ethylene; diethyl ether; ethanol dehydration; Al-based catalyst; zeolite.

**ENGINEERING JOURNAL** Volume 20 Issue 3

Received 18 September 2015 Accepted 6 January 2016 Published 19 August 2016 Online at http://www.engj.org/ DOI:10.4186/ej.2016.20.3.63

#### 1. Introduction

Ethylene is an important chemical in petrochemical industries, which is the most widely used as feedstock to produce ethylene oxide (EO) and polymers such as polyethylene (PE), polyethylene terephthalate (PET), and polyvinylchloride (PVC) [1–3]. At present, ethylene is mainly produced by thermal cracking of petroleum-based products such as naphtha. This process consumes intensive high energy generating large amounts of CO<sub>2</sub> greenhouse gas emissions. Therefore, the catalytic dehydration of ethanol to ethylene is an alternative promising way to obtain the reduction of CO<sub>2</sub> emission, low production cost and energy consumption [3, 4] since it is cleaner technology than the conventional process. There are many solid acid catalysts used for ethanol dehydration to ethylene, which are efficient in catalyzing the dehydration of ethanol. These catalysts include the supported phosphoric acid, alumina, silica-alumina, heteropolyacid catalysts and zeolites [5, 6]. Furthermore, different transition metal catalysts such as titanium oxides, magnesium oxides, cobalt oxides, chromium oxide and silver salt of tungstophosphoric acid [7, 8] were also investigated for the catalytic dehydration of ethanol. The catalytic activity for dehydration of ethanol could be correlated to the number of strong Brønsted acid sites in catalyst [9].

In recent years, alumina (Al<sub>2</sub>O<sub>3</sub>) and zeolites (alumino-silicate materials) have been used as solid acid catalysts for ethanol dehydration. H-ZSM-5 zeolite has a good performance at lower reaction temperature having higher ethylene yield, but it easily deactivates by coke formation during the reaction due to its smaller pore size and strong acidic properties[5, 10]. Using alumina and/or other types of zeolite or modified H-ZSM-5 as catalysts instead of H-ZSM-5 should be preferred to avoid the coke formation during the process of ethanol dehydration [11-13]. The physicochemical properties of alumina catalysts depend on the methods of preparation and calcination conditions. There are many methods to synthesize alumina catalysts such as solvothermal synthesis, sol-gel synthesis, flame spray pyrolysis, precipitation, emulsion evaporation, microwave synthesis, hydrothermal synthesis and heat treatment of aluminium hydroxides such as boehmite and gibbsite. The solvothermal and sol-gel methods are commonly used for synthesis of alumina [14]. The γ-Al<sub>2</sub>O<sub>3</sub> and mixed γ-χ phase Al<sub>2</sub>O<sub>3</sub> catalysts were also investigated for this reaction because they exhibit high thermal stability, fine particle size, high surface area, inhibit side reaction and high acidity, which is enough to produce ethylene via ethanol dehydration. It was also found that crystal structures, grain sizes and morphologies can be controlled by process conditions such as solute concentration, reaction temperature, reaction time and the type of solvent [14, 15]. However, there have been no reports of the ethanol dehydration to ethylene over H-beta zeolite (HBZ), which is microporous zeolite having high surface area, high thermal stability and high acidity. Moreover, H-beta zeolite exhibits larger pore size than H-ZSM-5. Hence, it is expected to produce hydrocarbon with less coke deposition due to higher diffusivity in the pore [16].

In this work, we report the characteristics and catalytic properties of different Al-based catalysts including HBZ, modified H-beta zeolite with γ-Al<sub>2</sub>O<sub>3</sub> (Al-HBZ) and mixed γ-χ phase Al<sub>2</sub>O<sub>3</sub> (M-Al) catalysts over the catalytic ethanol dehydration. The catalysts were characterized using various techniques such as X-ray diffraction (XRD), N<sub>2</sub>physisorption, scanning electron microscopy (SEM) and energy dispersive X-ray spectroscopy (EDX), and temperature-programmed desorption of ammonia (NH<sub>3</sub>-TPD). The catalytic properties were measure towards the gas-phase ethanol dehydration using a fixed-bed flow microreactor to measure the ethanol conversion and product distribution.

# 2. Experimental

#### 2.1. Materials

The commercial HBZ used in this study was purchased from Tosoh Corporation. The typical structure of HBZ is shown in Scheme 1. Aluminium isopropoxide: AIP (98% from Sigma-Aldrich chemical company, Inc.), toluene (99% Merck Company Ltd.), 1-butanol (99% Merck company Ltd.), methanol (Merck company Ltd.), ethanol (99.99% Merck company Ltd.), ultra-high purity nitrogen gas [99.99% Linde (Thailand) Public Company Ltd.], hydrochloric acid (37.7% hydrochloric acid from Sigma-Aldrich chemical company, Inc.) were employed.

Scheme 1. Typical structure of H-beta zeolite (HBZ) [17].

# 2.2. Preparation of Al-based Catalysts

Besides the HBZ catalyst, other two Al-based catalysts were used and prepared from different methods. The mixed γ-χ Al<sub>2</sub>O<sub>3</sub> (M-Al) was prepared by the solvothermal method as reported by Janlamool and Jongsomjit [18]. The modified H-beta zeolite with γ-Al<sub>2</sub>O<sub>3</sub>(Al-HBZ) was prepared by the modified sol-gel method. First, aluminium isopropoxide precursor was hydrolyzed in solution of ethanol and deionized water with volume ratio of 1:1 by stirring at 80°C for 1 h and then at 90°C for 15 minutes. After that, the HBZ was added into the solution with HBZ to Al weight ratio of 1:3. Subsequently, hydrochloric acid was added to the solution, which was stirred at 90°C for 10 h with the controlled pH of 2.5. After this step, the product became viscous. The formed gel was dried overnight at 110°C and calcined at 550°C under air flow for 2 h to obtain the Al-HBZ catalyst.

# 2.3. Catalyst Characterization

All catalysts were characterized by several techniques as follows:

X-ray diffraction (XRD): XRD was performed to determine the bulk crystalline phases of sample. It was conducted using a SIEMENS D-5000 X-ray diffractometer with  $CuK_{\alpha}$  ( $\lambda$  = 1.54439 Å). The spectra were scanned at a rate of 2.4° min<sup>-1</sup> in the range of 2 theta = 10 to 90°.

N<sub>2</sub>physisorption: Measurement of BET surface area, average pore diameter and pore size distribution were determined by N<sub>2</sub>physisorption using a Micromeritics ASAP 2000 automated system.

Temperature-programmed desorption of ammonia (NH<sub>3</sub>-TPD): The acid properties of catalysts were investigated by NH<sub>3</sub>-TPD using Micromeritics Chemisorb 2750 pulse chemisorption system.

Scanning electron microscopy (SEM) and energy dispersive X-ray spectroscopy (EDX): SEM and EDX were used to investigate the morphology and elemental distribution of catalysts, respectively using Hitashi mode S-3400N. Micrographs were taken at the accelerating voltage of 30 kV and magnification ranging from 1,000 to 10,000 and the resolution of 3 nm. The SEM was operated using the secondary scattering electron (SE) mode. EDX was performed using Apollo X Silicon Drift Detector Series by EDAX. Before the SEM observation, the sample was conductive to prevent charging by coating with platinum particle under the ion sputtering device.

#### 2.4. Reaction Test

The dehydration of ethanol was carried out in a fixed-bed continuous flow microreactor made from a borosilicate glass with an inside diameter of 0.7 cm and length of 33 cm. The reaction system is shown in Scheme 2. In the experiment, 0.01 g of packed quartz wool and 0.05 g of catalyst were loaded into the reactor. Then, the catalyst was pretreated in argon (60ml/min) at 200°C for 1 h under atmospheric pressure. The liquid ethanol was vaporized in a flowing of argon by controlled injection with a single syringe pump at a constant flow rate of ethanol 1.45 ml/h [WHSV = 22.9 (gethanolgcat<sup>-1</sup>) h<sup>-1</sup>]. The reaction was carried out at temperature ranging from 200 to 400°C by feeding the vaporized ethanol into the reactor. The reaction was carried out at each temperature for 1 h. The products were analyzed by a Shimadzu GC8A gas chromatograph with flame ionization detector (FID) using capillary column (DB-5). Nitrogen (pressure of 260 kPa) was used as carrier gas in GC using the temperature of injector and detector at 150°C

#### 2.5. Calculation

In this work, the ethanol conversion ( $X_{EtOH}$ ), ethylene selectivity ( $S_E$ ), diethyl ether selectivity ( $S_{DEE}$ ), ethylene yield (Y<sub>E</sub>) and diethyl ether yield (Y<sub>DEE</sub>) are defined as follows:

$$X_{EtOH} = \frac{n_{EtOH,0} - n_{EtOH,1}}{n_{EtOH,0}} \times 100$$
 (1)

$$S_{E} = \frac{n_{E,1}}{\sum n_{i,1}} \times 100 \tag{2}$$

$$X_{EtOH} = \frac{n_{EtOH,0} - n_{EtOH,1}}{n_{EtOH,0}} \times 100$$

$$S_{E} = \frac{n_{E,1}}{\sum n_{i,1}} \times 100$$

$$S_{DEE} = \frac{2n_{DEE,1}}{\sum n_{i,1}} \times 100$$

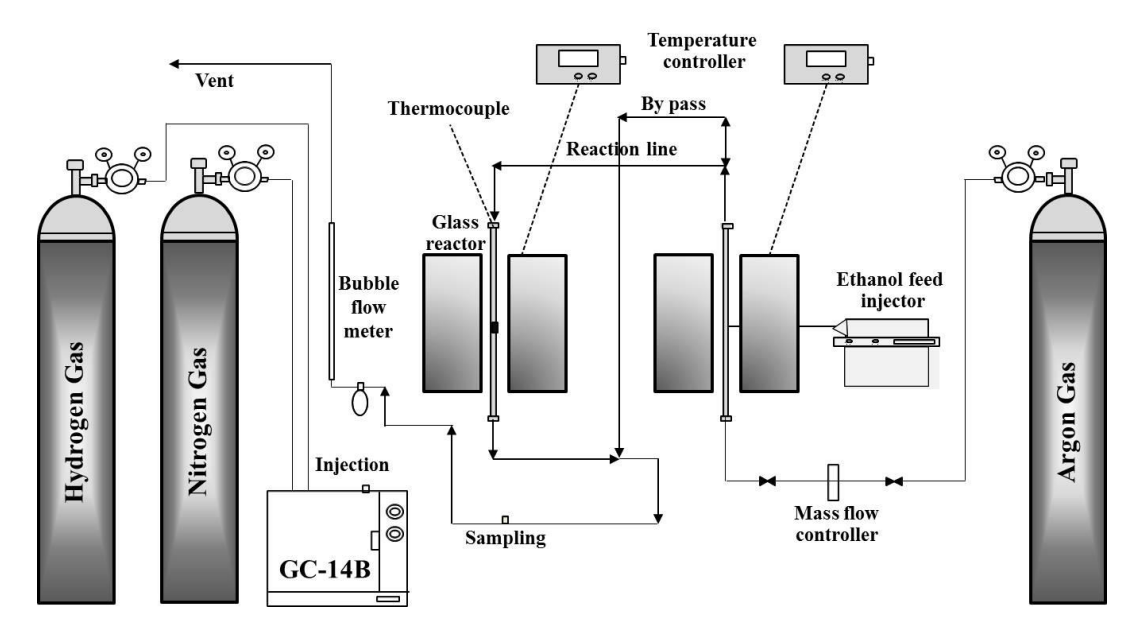
$$Y_{E} = \frac{S_{E} \times X_{EtOH}}{100}$$

$$Y_{DEE} = \frac{S_{DEE} \times X_{EtOH}}{100}$$
(5)

$$Y_{E} = \frac{\overline{S_{E} \times X_{EtOH}}}{100}$$
 (4)

$$Y_{\text{DEE}} = \frac{S_{\text{DEE}} \times X_{\text{EtOH}}}{100} \tag{5}$$

where netoh,0 and netoh,1 are defined as the molar flow rate (mmol/min) of ethanol in feed and in products, respectively;  $n_{E,1}$ ,  $n_{DEE,1}$ , and  $\sum n_{i,1}$  are defined as the molar flow rate of ethylene, diethyl ether and total products, respectively [4, 19].



Scheme 2. Ethanol reaction system.

# **Results and Discussion**

# 3.1. Catalyst Characterization

The XRD patterns of different catalysts are shown in Fig. 1. The specific sharp peaks of HBZ catalyst consist of 2θ at 14.6and 22.4° [16, 20]. The characteristic peaks of pure γ-Al<sub>2</sub>O<sub>3</sub> are 46 and 67°[18]. When adding γ-Al<sub>2</sub>O<sub>3</sub> into HBZ to obtain the Al-HBZ catalyst, XRD peaks were appeared at 14.6, 22.4 (HBZ), 46 and 67° (γ-Al<sub>2</sub>O<sub>3</sub>). It indicated that the main structure of HBZ did not alter with Al addition. It was appeared that the intensity of characteristic peak (22.4°) for HBZ decreased with Al addition suggesting that the lower crystallinity of Al-HBZ was obtained. For the M-Al catalyst, the XRD peaks were appeared at 43, 46and 67°, which can be assigned to the presence of  $\gamma$ -Al<sub>2</sub>O<sub>3</sub> (46and 67°) coupled with  $\chi$ - Al<sub>2</sub>O<sub>3</sub> (43°) as also reported by Janlamoon and Jongsomjit [18].

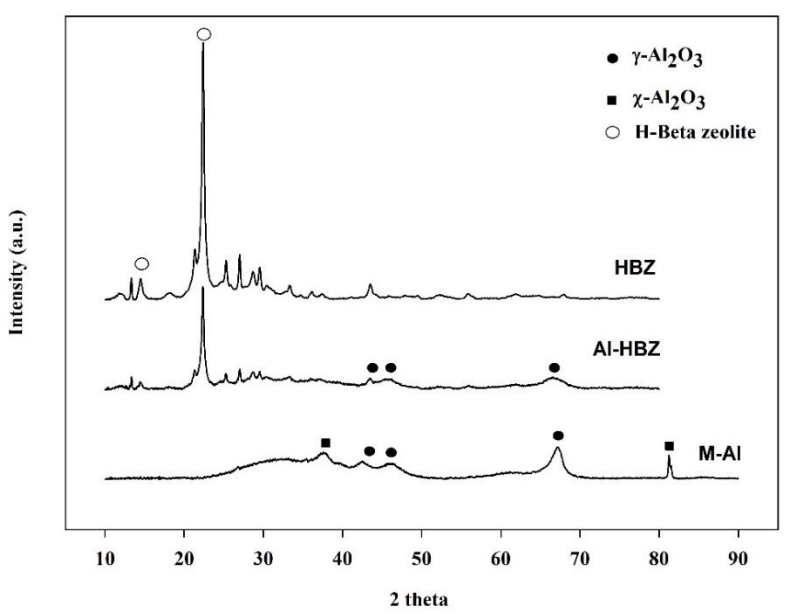


Fig. 1. XRD patterns of all catalysts.

The BET surface area (S<sub>BET</sub>) of catalysts is listed in Table 1. The HBZ catalyst exhibits the largest surface area of 522 m<sup>2</sup>/g. With Al addition, the decreased surface area (306 m<sup>2</sup>/g) was evident for the Al-HBZ catalyst due to the pore blockage of Al in HBZ. The surface area of M-Al catalyst was 195 m<sup>2</sup>/g. The large surface area helps more opportunities for reactants to contact and react, which would adjust the catalytic activity for ethanol dehydration [4].

Table 1. Properties of catalysts.

Catalyat	Pore size	BET Surface		desorption ol NH3/g)	Total acidity
Catalyst	(nm)	Area S <sub>BET</sub> (m <sup>2</sup> /g)	Weak	Medium to strong	(μmol NH3/g)
HBZ	2.2	521.6	844.8	672.5	1517.3
Al-HBZ	3.4	305.9	813.3	731.6	1544.9
M-Al	9.0	195.4	268.7	510.0	778.6

The  $N_2$  adsorption-desorption isotherms for all catalysts are shown in Fig. 2. The pore structure of HBZ exhibited the characteristic of microporous structure according to type I classified by IUPAC (International Union of Pure and Applied Chemistry). After the introduction of Al to obtain Al-HBZ, the characteristic of type I was still observed. However, a small hysteresis loop also occurred at  $P/P_o$  around 0.4 to 0.8 indicating the presence of a small portion of mesoporous structure regarding type IV with introduction of Al. This is corresponding to the decreased surface area of Al-HBZ compared to HBZ. The M-Al showed the pore structure of mesoporous material according to type IV indicating the lowest surface area among other two catalysts.

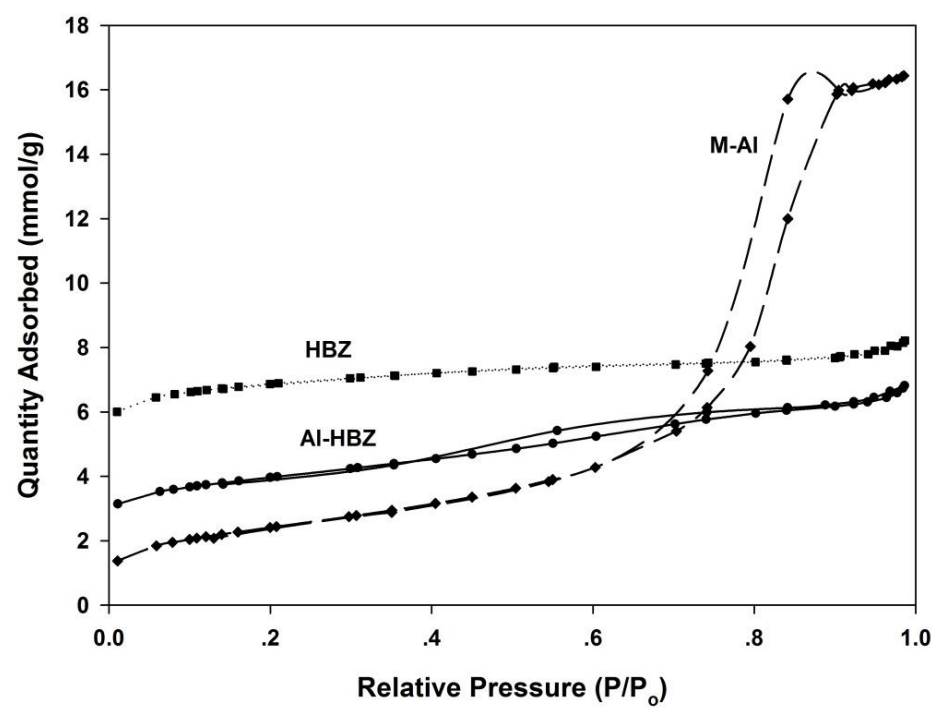


Fig. 2. The N<sub>2</sub> adsorption-desorption isotherms for all catalysts.

Figure 3 shows the pore size distribution of catalysts, which are related to the pore structure as discussed from Fig. 2. The average pore size (Table 1) of HBZ was ca.2 nm (micropore). The average pore size of M-Al was ca.9 nm (mesopore), whereas the Al-HBZ exhibited mainly microporous structure with only a small portion of mesoporous structure as also mentioned above. The difference in pore size diameter and S<sub>BET</sub> affected the observed productivity in this reaction because the small pore size and high S<sub>BET</sub> may decrease higher hydrocarbon and byproducts leading to increasing of main product selectivity and ethanol conversion. Moreover, the high S<sub>BET</sub> would affect to the increased catalytic activity for ethanol dehydration [4].

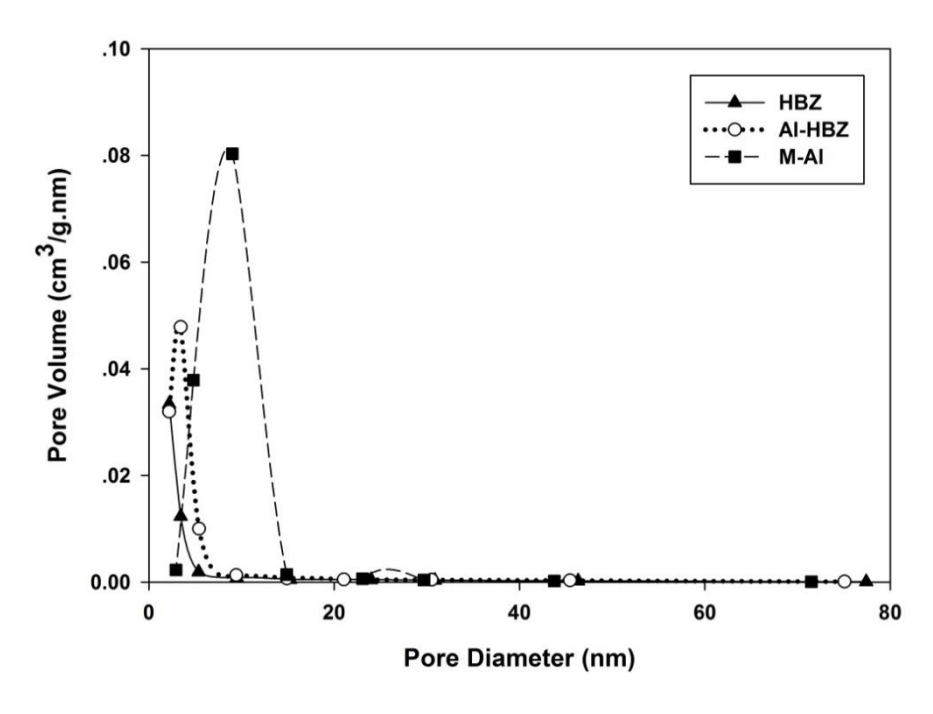


Fig. 3. Pore size distribution for all catalysts.

The morphology of catalysts was determined by SEM as shown in Fig. 4. It can be observed that morphologies of both HBZ and Al-HBZ were similar spheroidal, but Al-HBZ had a rougher surface than HBZ due to Al deposition. The M-Al showed different morphology with more roughness.

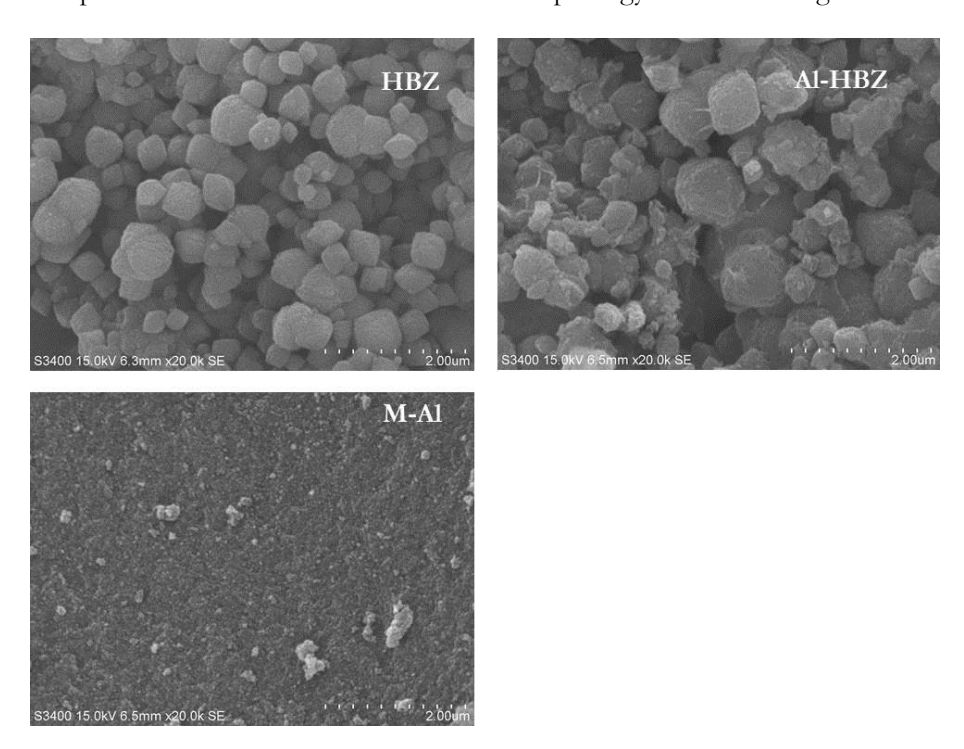


Fig. 4. SEM images of all catalysts.

The EDX analysis was used to quantitatively measure the amounts of elemental composition on the catalyst surface. The results are illustrated in Table 2. It revealed the chemical composition of each catalyst. The amounts of Al present at surface were in the range of M-Al > Al-HBZ > HBZ, which were reasonable. In other words, the Si/Al ratio of HBZ was the highest. The decreased Si/Al ratio is perhaps related to the decrease in weak acid sites, but increased strong acid sites as well as increased total acidity [21]. Thus, the acid properties of catalysts were determined using NH<sub>3</sub>-TPD.

Table 2. Elemental composition obtained from EDX.

	Element						
Catalyst		% Weight			% Atom	_	
	Al	Si	0	Si/Al	Al	Si	0
HBZ	3.26	44.95	51.78	13.79	2.44	32.28	65.28
Al-HBZ	32.1	22.59	45.31	0.70	24.55	16.67	58.68
M-Al	61.06	-	38.94	-	48.18	-	51.82

The NH<sub>3</sub>-TPD profiles (Fig. 5) of all catalysts were similar consisting of two groups of desorption peaks. The desorption peaks at low temperature below 250°C are assigned to weak acid sites, whereas those above 400°C are strong acid sites. The number of acid site on catalyst can be calculated by integration of desorption area of ammonia according to the Gauss curve fitting method. The amount of acidity of catalysts is also displayed in Table 1. It was found that HBZ had the highest amount of weak acid sites. The addition of Al into HBZ resulted in decreased amount of weak acid site, but increased moderate to strong acid sites as well as total acidity. This can be attributed to the addition of Al possibly alter the acid distribution with different Si/Al ratios of catalysts [21]. Furthermore, the slight difference in total acidity of HBZ and Al-HBZ perhaps results from only slightly different Si/Al ratios. However, the addition of alumina into H-beta zeolite may result in slightly increased amount of medium to strong acid site [22]. However, the amount of weak acid site, moderate to strong acid site and total acid site of M-Al were the

lowest among other two catalysts. It was reported that the weak acid site is essential for the catalytic dehydration of ethanol to ethylene [4, 5, 22, 23]. Thus, the presence of large amount of weak acid would be beneficial to enhance the catalytic activity.

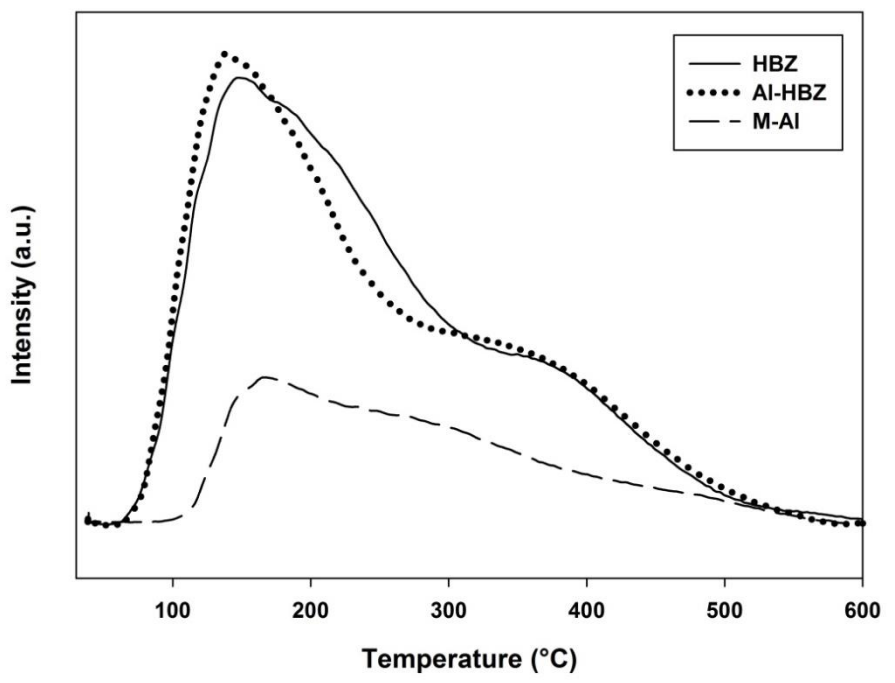


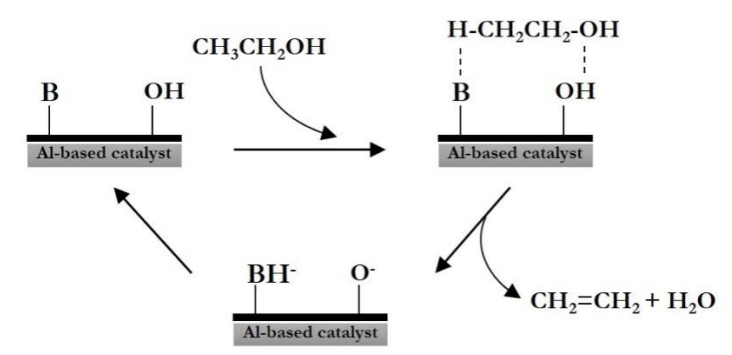
Fig. 5. NH<sub>3</sub>-TPD profiles of all catalysts.

# 3.2. Catalytic Properties

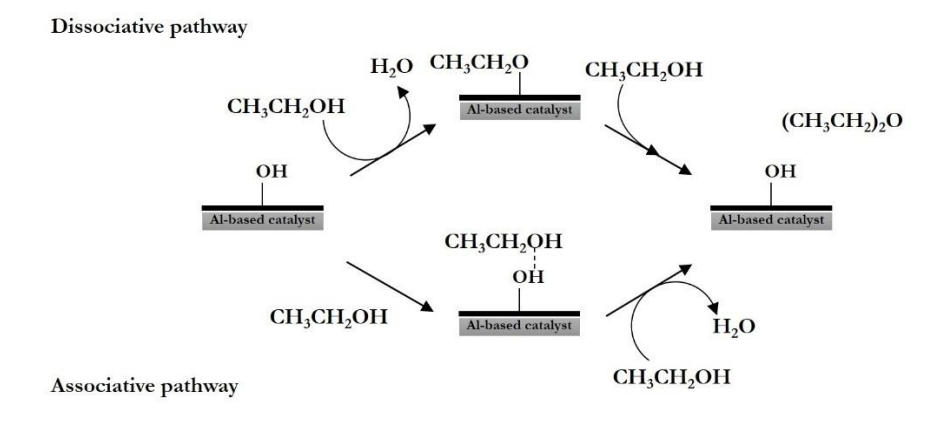
It is known that ethanol dehydration reaction has two competitive ways occurred [4] as follows:

$$C_2H_5OH \rightarrow C_2H_4 + H_2O$$
 +44.9 kJ/mol (6)  
 $2C_2H_5OH \rightarrow C_2H_5OC_2H_5 + H_2O$  -25.1 kJ/mol (7)

The first reaction (6) is dehydration of ethanol to ethylene (endothermic reaction), while the second one (7) is side reaction to produce DEE (exothermic reaction). DEE is produced in significant quantities at low temperature. However, ethylene is obtained via ethanol dehydration at high temperatures. The Mechanism of dehydration reaction to ethylene and DEE is shown in Schemes 3 and 4, respectively. Figure 6 shows the ethanol conversion at temperature range of 200 to 400°C. Ethanol conversion apparently increased with increased temperature. It was found that the HBZ exhibited the highest conversion of ethanol among other two catalysts for all reaction temperature. This can be attributed to the large amount of weak acid sites present in HBZ catalyst. The ethanol conversion for Al-HBZ and M-Al was found to have a similar trend with that of HBZ, where the conversion increased with increasing reaction temperature. However, the conversion obtained from HBZ was the highest.



Scheme 3. Ethanol dehydration to ethylene at base (B) and Brønsted acid(OH) catalyst sites [24].



Scheme 4. Ethanol dehydration to DEE [24].

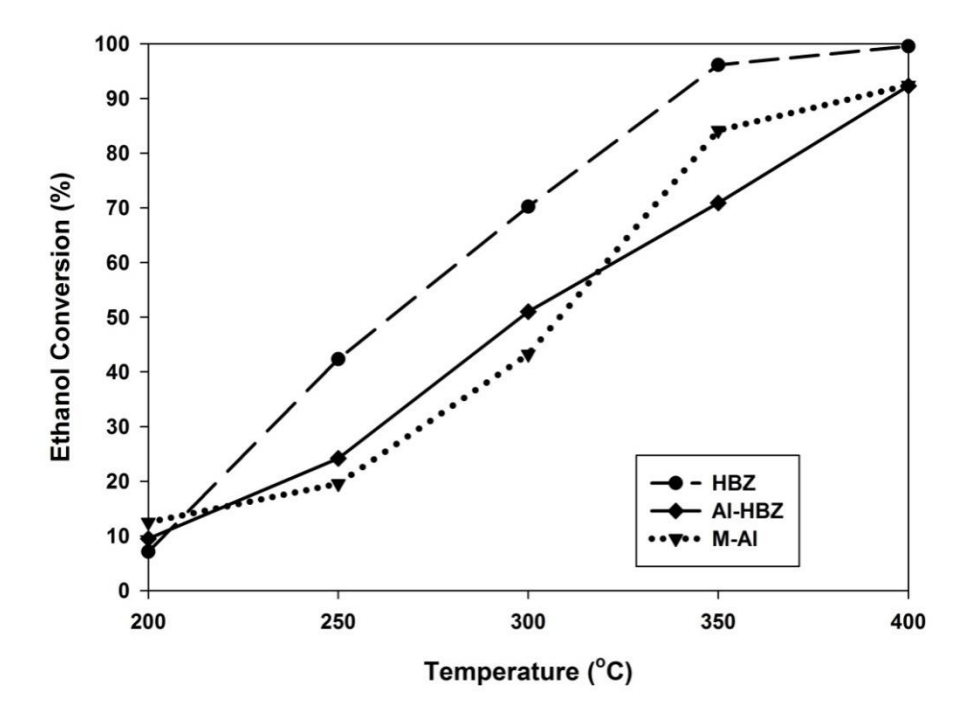


Fig. 6. Ethanol conversion for all catalysts.

The ethylene selectivity of catalysts is shown in Fig. 7. For all catalysts, the ethylene selectivity increased with increasing reaction temperature. The HBZ catalyst produced more ethylene than other two catalysts. However, at 400°C, the selectivity to ethylene for all catalysts was almost equal.

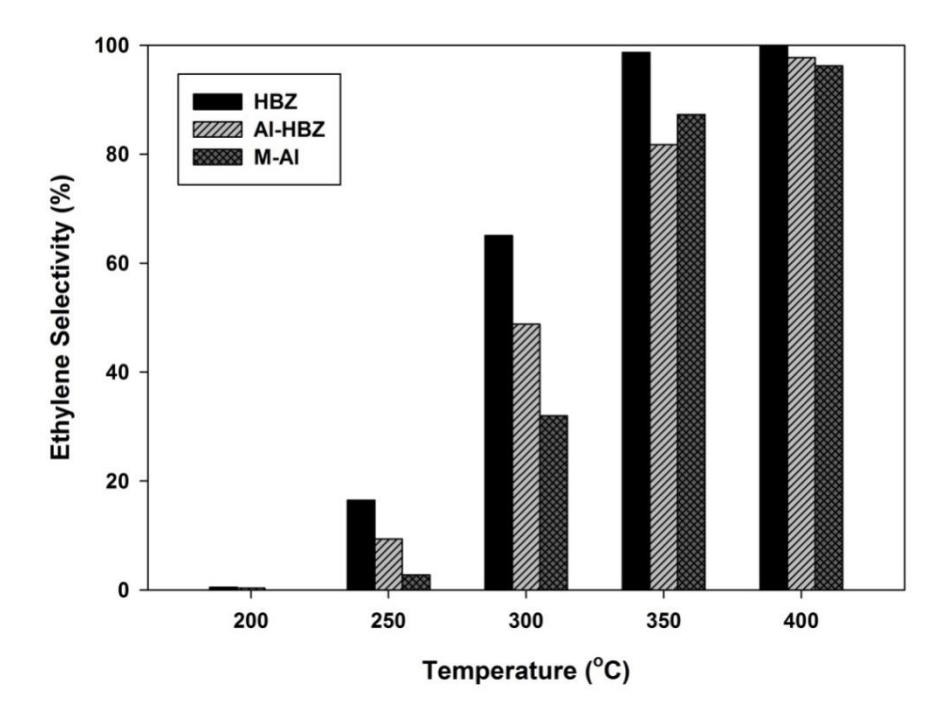


Fig. 7. Ethylene selectivity for all catalysts.

Besides ethylene, DEE is also obtained, especially at low reaction temperature. The DEE selectivity is shown in Fig. 8. It can be observed that at 200°C, all catalysts produced only DEE. However, at this temperature, the ethanol conversion was extremely low. Hence, the DEE yield (product of ethanol conversion and DEE selectivity) was quite low. It was found that the M-Al catalyst exhibited slightly higher DEE selectivity than other two catalysts.

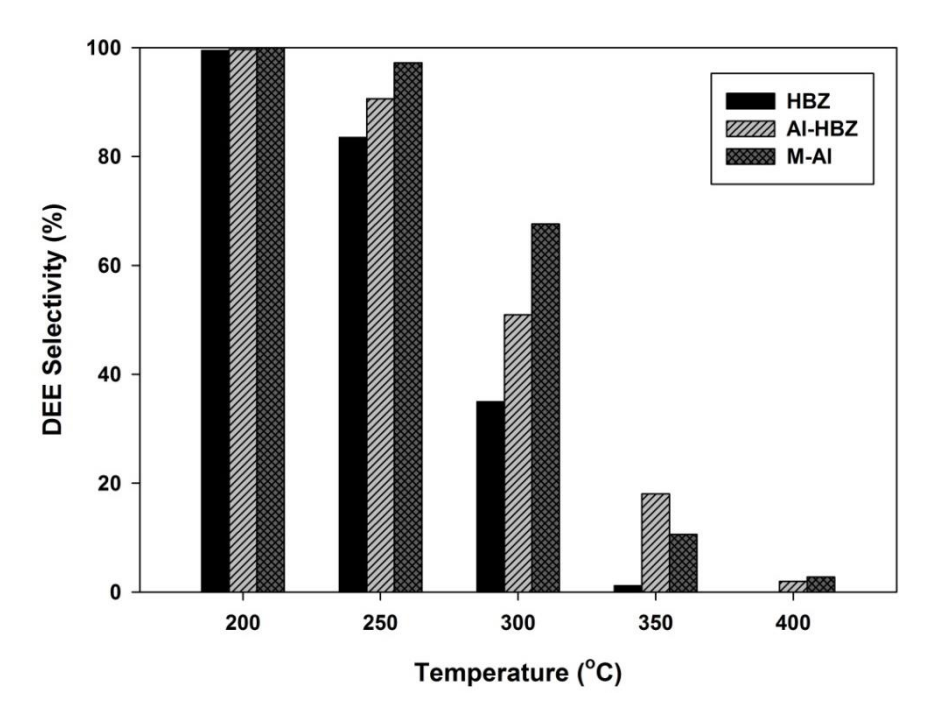


Fig. 8. DEE selectivity for all catalysts.

In order to compare the product yields obtained from catalysts. The product yields were calculated at different temperatures as shown in Table 3. Considering for ethylene selectivity, the highest ethylene yield

was obtained at 400°C indicating that high catalytic activity as well as ethanol conversion is the highest when compared with low temperature reaction. The increase in ethanol conversion results in increased product yield. At 400°C, the ethylene yield increased in the range of HBZ > Al-HBZ > M-Al. The DEE selectivity is also interesting. It can be observed that the highest DEE yield (35.3%) was obtained from the HBZ catalyst at 250°C. The low DEE yield was caused by low conversion. In order to improve the DEE yield, the chemical promoter is perhaps necessary. Chen et al. studied the addition of some chemical promoters to improve the catalytic dehydration. The chemical promoters used for this reaction such as titania, niobia, molybdenum oxide and silica were investigated [19, 25–27].

Table 3. Product yield of all catalysts

0 . 1 .		Ethy	lene yield	1 (%)			DI	EE yield (	(%)	
Catalyst	200 °C	250 °C	300 °C	350 °C	400 °C	200 °C	250 °C	300 °C	350 °C	400 °C
HBZ	0.0	7.0	45.7	94.8	99.4	7.1	35.3	24.5	1.1	0.0
Al-HBZ	0.0	2.3	24.9	57.9	90.2	9.5	21.9	26.0	12.8	1.8
M-Al	0.0	0.5	13.8	73.4	88.9	12.5	19.0	29.2	8.9	2.5

Table 4. Comparison of catalysts for ethylene synthesis and their catalytic ability.

Catalyst	Surface area (m²/g)	Reaction temperature (°C)	Ethanol conversion (%)	Ethylene selectivity (%)	Ref.
HBZ	522	200-400	7-100	1-100	This work
Al-HBZ	306	200-400	9-92	0-98	This work
M-Al	195	200-400	12-92	0-96	This work
H-ZSM-5	366	400	99	10	[13]
20HP-ZSM-5	74	250-450	25-100	3-98	[13]
$\gamma$ -Al <sub>2</sub> O <sub>3</sub>	204	400-550	70-100	40-95	[19]
$TiO_2/\gamma$ - $Al_2O_3$	187	360-550	70-100	50-99	[19]
SAPO-34	300	500	100	100	[28]
ZS(25)-HS-4	276	500	100	27	[28]
ZS(25)-MM-4	352	500	100	24	[28]

Moreover, there were summarized reports of catalytic ability for ethanol dehydration to ethylene over various catalysts (Table 4). It is shown that HBZ, Al-HBZ and M-Al catalysts in this work are comparable to those of typical and modified catalysts. Ramesh et al. and Duan et al. studied structure and reactivity of modified H-ZSM-5 catalysts for ethanol dehydration. They found that the highest surface area was obtained by unmodified H-ZSM-5 and testing of catalytic activity at 250-500°C. Then, the result showed that ethanol conversion and ethylene selectivity of modified H-ZSM-5 were lower than that of HBZ for this work. It can be concluded that HBZ exhibited higher catalytic activity than their catalysts [13, 28]. In addition, Chen et al. investigated the modification effects of TiO<sub>2</sub>-doped on alumina catalysts packed in microreactor. Their results showed that the catalytic activity of their catalyst was lower than that of Al-HBZ and M-Al catalysts at the same reaction temperature [19]. Thus, the HBZ is practical to be applied for the ethanol dehydration to ethylene.

# 4. Conclusion

Among all three Al-based catalysts in this study, the HBZ catalyst is the most effective to convert ethanol into ethylene with ca. 99% of ethylene yield (at high temperature, i.e. 400°C) and DEE with ca. 35.3% of DEE yield (at low temperature, i.e. 250°C). This is attributed to the high amount of weak acid sites present in the HBZ catalyst. Although, no deactivation of catalyst was found at 400°C, the stability test towards time on stream (TOS) should be further investigated in future work. Considering the production of DEE from ethanol at low temperature (250°C), it is possible to use the HBZ catalyst.

# Acknowledgement

The authors thank the Thailand Research Fund (TRF), the National Research Council of Thailand (NRCT) and Ratchadaphiseksomphot Endowment Fund (2015) of Chulalongkorn University (CU-58-027-AM) for financial support of this project.

# References

- [1] A. P. Kagyrmanova, V. A. Chumachenko, V. N. Korotkikh, V. N. Kashkin, and A. S. Noskov, "Catalytic dehydration of bioethanol to ethylene: Pilot-scale studies and process simulation," *Chemical Engineering Journal*, vol. 176-177, pp. 188-194, 2011.
- [2] J. Bedia, R. Barrionuevo, J. Rodríguez-Mirasol, and T. Cordero, "Ethanol dehydration to ethylene on acid carbon catalysts," *Applied Catalysis B: Environmental*, vol. 103, no. 3-4, pp. 302-310, 2011.
- [3] V. V. Bokade, and G. D. Yadav, "Heteropolyacid supported on montmorillonite catalyst for dehydration of dilute bio-ethanol," *Applied Clay Science*, vol. 53, no. 2, pp. 263-271, 2011.
- [4] Y. Chen, Y. Wu, L. Tao, B. Dai, M. Yang, Z. Chen, and X. Zhu, "Dehydration reaction of bio-ethanol to ethylene over modified SAPO catalysts," *Journal of Industrial and Engineering Chemistry*, vol. 16, no. 5, pp. 717-722, 2010.
- [5] Q. Sheng, K. Ling, Z. Li, and L. Zhao, "Effect of steam treatment on catalytic performance of HZSM-5 catalyst for ethanol dehydration to ethylene," *Fuel Processing Technology*, vol. 110, pp. 73-78, 2013.
- [6] L. Matachowski, M. Zimowska, D. Mucha, and T. Machej, "Ecofriendly production of ethylene by dehydration of ethanol over Ag<sub>3</sub>PW<sub>12</sub>O<sub>40</sub> salt in nitrogen and air atmospheres," *Applied Catalysis B: Environmental*, vol. 123-124, pp. 448-456, 2012.
- [7] T. Zaki, "Catalytic dehydration of ethanol using transition metal oxide catalysts," *Journal of Colloid and Interface Science*, vol. 284, no. 2, pp. 606-613, 2005.
- [8] T. K. Phung, R. Radikapratama, G. Garbarino, A. Lagazzo, P. Riani, and G. Busca, "Tuning of product selectivity in the conversion of ethanol to hydrocarbons over H-ZSM-5 based zeolite catalysts," *Fuel Processing Technology*, vol. 137, pp. 290-297, 2015.
- [9] A. Rahmanian, and H. S. Ghaziaskar, "Continuous dehydration of ethanol to diethyl ether over aluminum phosphate–hydroxyapatite catalyst under sub and supercritical condition," *The Journal of Supercritical Fluids*, vol. 78, pp. 34-41, 2013.
- [10] F. Wang, M. Luo, W. Xiao, X. Cheng, and Y. Long, "Coking behavior of a submicron MFI catalyst during ethanol dehydration to ethylene in a pilot-scale fixed-bed reactor," *Applied Catalysis A: General*, vol. 393, no. 1-2, pp. 161-170, 2011.
- [11] N. Zhan, Y. Hu, H. Li, D. Yu, Y. Han, and H. Huang, "Lanthanum–phosphorous modified HZSM-5 catalysts in dehydration of ethanol to ethylene: A comparative analysis," *Catalysis Communications*, vol. 11, no. 7, pp. 633-637, 2010.
- [12] J. Bi, X. Guo, M. Liu, and X. Wang, "High effective dehydration of bio-ethanol into ethylene over nanoscale HZSM-5 zeolite catalysts," *Catalysis Today*, vol. 149, no. 1-2, pp. 143-147, 2010.
- [13] K. Ramesh, L. Hui, Y. Han, and A. Borgna, "Structure and reactivity of phosphorous modified H-ZSM-5 catalysts for ethanol dehydration," *Catalysis Communications*, vol. 10, no. 5, pp. 567-571, 2009.
- [14] C. Meephoka, C. Chaisuk, P. Samparnpiboon, and P. Praserthdam, "Effect of phase composition between nano γ- and χ-Al<sub>2</sub>O<sub>3</sub> on Pt/Al<sub>2</sub>O<sub>3</sub> catalyst in CO oxidation," *Catalysis Communications*, vol. 9, no. 4, pp. 546-550, 2008.
- [15] K. Pansanga, J. Panpranot, O. Mekasuwandumrong, C. Satayaprasert, J. G. Goodwin, and P. Praserthdam, "Effect of mixed γ- and χ-crystalline phases in nanocrystalline Al<sub>2</sub>O<sub>3</sub> on the dispersion of cobalt on Al<sub>2</sub>O<sub>3</sub>," *Catalysis Communications*, vol. 9, no. 2, pp. 207-212, 2008.
- [16] S. Sujeerakulkai, and S. Jitkarnka, "Bio-based hydrocarbons and oxygenates from catalytic bio-ethanol dehydration: comparison between gallium and germanium oxides as promoters on HBeta zeolites with various silica to alumina ratios," *Journal of Cleaner Production*, vol. 111, pp. 51-61, 2016.
- [17] B. K. Marcus, and W. E. Cormier, "Going Green with Zeolites," *Chemical Engineering Progress*, vol. 95, no. 6, pp. 47-53. 1999.
- [18] J. Janlamool, and B. Jongsomjit, "Oxidative dehydrogenation of ethanol over AgLi–Al<sub>2</sub>O<sub>3</sub> catalysts containing different phases of alumina," *Catalysis Communications*, vol. 70, pp. 49-52, 2015.

- [19] G. Chen, S. Li, F. Jiao, and Q. Yuan, "Catalytic dehydration of bioethanol to ethylene over TiO<sub>2</sub>/γ-Al<sub>2</sub>O<sub>3</sub> catalysts in microchannel reactors," *Catalysis Today*, vol. 125, no. 1-2, pp. 111-119, 2007.
- [20] J. Nowicki, L. Mokrzycki, and B. Sulikowski, "Synthesis of novel perfluoroalkylglucosides on zeolite and non-zeolite catalysts," *Molecules*, vol. 20, no. 4, pp. 6140-52, 2015.
- [21] S. Hajimirzaee, M. Ainte, B. Soltani, R. M. Behbahani, G. A. Leeke, and J. Wood, "Dehydration of methanol to light olefins upon zeolite/alumina catalysts: Effect of reaction conditions, catalyst support and zeolite modification," *Chemical Engineering Research and Design*, vol. 93, pp. 541-553, 2015.
- [22] H. Xin, X. Li, Y. Fang, X. Yi, W. Hu, Y. Chu, F. Zhang, A. Zheng, H. Zhang, and X. Li, "Catalytic dehydration of ethanol over post-treated ZSM-5 zeolites," *Journal of Catalysis*, vol. 312, pp. 204-215, 2014.
- [23] X. Zhang, R. Wang, X. Yang, and F. Zhang, "Comparison of four catalysts in the catalytic dehydration of ethanol to ethylene," *Microporous and Mesoporous Materials*, vol. 116, no. 1-3, pp. 210-215, 2008.
- [24] W. Alharbi, E. Brown, E. F. Kozhevnikova, and I. V. Kozhevnikov, "Dehydration of ethanol over heteropoly acid catalysts in the gas phase," *Journal of Catalysis*, vol. 319, pp. 174-181, 2014.
- [25] Y. Han, C. Lu, D. Xu, Y. Zhang, Y. Hu, and H. Huang, "Molybdenum oxide modified HZSM-5 catalyst: Surface acidity and catalytic performance for the dehydration of aqueous ethanol," *Applied Catalysis A: General*, vol. 396, no. 1-2, pp. 8-13, 2011.
- [26] T. K. Phung and G. Busca, "Ethanol dehydration on silica-aluminas: Active sites and ethylene/diethyl ether selectivities," *Catalysis Communications*, vol. 68, pp. 110-115, 2015.
- [27] D. Liu, C. Yao, J. Zhang, D. Fang, and D. Chen, "Catalytic dehydration of methanol to dimethyl ether over modified γ-Al<sub>2</sub>O<sub>3</sub> catalyst," *Fuel*, vol. 90, no. 5, pp. 1738-1742, 2011.
- [28] C. Duan, X. Zhang, R. Zhou, Y. Hua, L. Zhang, and J. Chen, "Comparative studies of ethanol to propylene over HZSM-5/SAPO-34 catalysts prepared by hydrothermal synthesis and physical mixture," *Fuel Processing Technology*, vol. 108, pp. 31-40, 2013.

Hindawi Publishing Corporation Journal of Chemistry Volume 2016, Article ID 9672408, 8 pages http://dx.doi.org/10.1155/2016/9672408



# Research Article

# Effect of Mo-Doped Mesoporous Al-SSP Catalysts for the Catalytic Dehydration of Ethanol to Ethylene

# Titinan Chanchuey, Chaowat Autthanit, and Bunjerd Jongsomjit

Center of Excellence on Catalysis and Catalytic Reaction Engineering, Department of Chemical Engineering, Faculty of Engineering, Chulalongkorn University, Bangkok 10330, Thailand

Correspondence should be addressed to Bunjerd Jongsomjit; bunjerd.j@chula.ac.th

Received 14 September 2015; Revised 14 December 2015; Accepted 3 January 2016

Academic Editor: Juan M. Coronado

Copyright © 2016 Titinan Chanchuey et al. This is an open access article distributed under the Creative Commons Attribution License, which permits unrestricted use, distribution, and reproduction in any medium, provided the original work is properly cited.

The catalytic dehydration of ethanol to ethylene over the mesoporous Al-SSP and Mo-doped Al-SSP catalysts was investigated. The Al-SSP catalyst was first synthesized by the modified sol-gel method and then doped with Mo by impregnation to obtain 1% Mo/Al-SSP and 5% Mo/Al-SSP catalysts (1 and 5 wt% of Mo). The final catalysts were characterized using various techniques such as XRD,  $N_2$  physisorption, SEM/EDX, TEM, and  $NH_3$ -TPD. The catalytic activity for all catalysts in gas-phase ethanol dehydration reaction was determined at temperature range of 200°C to 400°C. It was found that the most crucial factor influencing the catalytic activities appears to be the acidity. The acid property of catalysts depended on the amount of Mo loading. Increased Mo loading in Al-SSP resulted in increased weak acid sites, which enhanced the catalytic activity. Besides acidity, the high concentration of Al at surface of catalyst is also essential to obtain high activity. Based on the results, the most suitable catalyst in this study is 1% Mo/Al-SSP catalyst, which can produce ethylene yield of ca. 90% at 300°C with slight amounts of diethyl ether (DEE) and acetaldehyde.

#### 1. Introduction

Ethylene is an important feedstock for organic chemistry industry used in the preparation of polyethylene, ethylene oxide, vinyl chloride (from ethylene dichloride), and styrene (from ethyl benzene) [1]. Conventionally, it has been commercially produced by the thermal cracking of liquefied petroleum gas (LPG) or naphtha. According to the report by Kniel et al. [2], this method continues to dominate the industry today. True [3] reported the top ethylene producing complexes by capacity in tons per year, which are all steam cracking plants. In addition, Iles and Martin [4] reported the capacities of the Braskem and Solvay Indupa regarding ethanol to ethylene plants, while Voegle [5] reported the capacity of the Dow Chemical plant, which is currently under construction [3-5]. Compared to the conventional process, the catalytic dehydration of ethanol to ethylene is attractive because it requires lower temperature (less than 600°C) [6] and it is cleaner technology. Moreover, ethanol can be produced from renewable sources including nonedible source such as molasses. At present, SynDol catalyst based on MgO-Al<sub>2</sub>O<sub>3</sub>/SiO<sub>2</sub> developed by Halcon SD has been employed

commercially, achieving 99% of ethanol conversion and 95.83% of ethylene yield at 450°C [7]. Equate Petrochemical Company's plant (Kuwait) [3] achieved 99.7% of ethylene selectivity and 100% of ethanol conversion using nanoscale HZSM-5 as the catalyst. It is known that the acid catalysts used in ethanol dehydration normally consist of silica and alumina-based catalysts. Upon the catalytic dehydration of ethanol, ethylene and diethyl ether (DEE) can be obtained using a solid acid catalyst as follows:

$$C_2H_5OH \longrightarrow C_2H_4 + H_2O$$
 (1)

$$C_2H_5OH \longrightarrow C_2H_5OC_2H_5 + H_2O$$
 (2)

$$C_2H_5OH \longrightarrow C_2H_4O + H_2$$
 (3)

The first reaction (1) has already been applied at the industrial level in the 1960s using aluminas as the catalysts [8]. The second reaction (2) occurs on the same catalysts under low temperature at moderate ethanol conversion, allowing very high selectivity and significant yields (>70%). In addition, acetaldehyde can be obtained by dehydrogenation of ethanol as seen in the third reaction (3). There are many works in

the literature related to the ethanol dehydration reaction over solid acid catalysts such as  $\gamma$ -alumina, zeolite, and silicaalumina [9, 10]. There are also research articles directed at obtaining molybdenum oxide over solid acid catalysts in various reactions, which require acid site for active site such as MoO<sub>3</sub>/Al<sub>2</sub>O<sub>3</sub>-SiO<sub>2</sub> in light olefin metathesis or partial oxidation [11, 12] and MoO<sub>3</sub>/Al<sub>2</sub>O<sub>3</sub> in hydrodesulfurization of thiophene [13]. However, there are only a few works focused on molybdenum oxide for ethanol dehydration reaction. In continuation of our interest in using alumina and silica catalysts, the SiO<sub>2</sub> is suitable as a support due to its high surface area, uniform pore size, excellent mechanical strength, and thermal stability such as hexagonal mesoporous silica, that is, spherical silica particle (SSP) [14]. Alumina is a good support due to its high metal dispersion ability and excellent mechanical properties. Moreover, the metal oxide promotes acidity in catalyst, and then this is interesting. The molybdenum oxide can enhance acidity in the catalyst. Thus, it is interesting to use molybdenum oxide with the silicaalumina acid catalysts.

In this study, the mesoporous SSP was synthesized and modified with alumina to obtain Al-SSP catalyst. Then, Mo was doped onto the Al-SSP catalysts. The relevant characterization techniques such as XRD, SEM, EDX, TEM, and NH<sub>3</sub>-TPD were carried out to reveal the physical and chemical properties of catalysts. The ethanol dehydration reaction of catalysts was performed to determine the catalytic activity and product selectivity.

#### 2. Materials and Methods

2.1. Materials. The chemicals used for preparation of the catalysts were tetraethyl orthosilicate (TEOS) (98%, Aldrich), cetyltrimethylammonium bromide (CTAB) (Aldrich), aluminium isopropoxide 98% [Al(OP $^{\rm i}$ )<sub>3</sub>] (Aldrich), ammonia 30% (Panreac), isopropanol (Merck), and ammonium heptamolybdate-tetrahydrate (Merck). Gases employed were He (99.99%, Air Liquide), H<sub>2</sub> (99.999%, Air Liquide), N<sub>2</sub> (99.9999%, Air Liquide), synthetic air (99.99%, Air Liquide), and Ar (99.9%, Air Liquide).

#### 2.2. Preparation of Catalysts

2.2.1. Synthesis of Al-SSP. First, the spherical silica particle (SSP) was synthesized following the method described by Janlamool et al. [14] with the mixture of 1 TEOS: 0.3 CTAB: 11 NH<sub>3</sub>: 58 Ethanol: 144 H<sub>2</sub>O (molar ratio). The resulting suspension was stirred at room temperature for 2 h. After that, the white precipitate was separated from solvent by centrifuge. Then, the sample was dried at 110°C overnight and calcined in air at 550°C for 6 h to obtain the SSP support. In order to prepare Al-SSP, the SSP was added into the solution of aluminium isopropoxide in isopropanol (to obtain 60 wt% of Al). The mixture was stirred for 1 h at room temperature. Then, it was added into ammonia solution for hydrolysis. Then, the mixture was stirred at room temperature for 20 h. The Al-SSP catalyst was dried at 110°C for 24 h. The dried sample was calcined in air at 650°C for 2 h [15]. The surface

area of Al-SSP catalyst obtained was  $443\,\mathrm{m}^2/\mathrm{g}$  using  $N_2$  physisorption technique.

2.2.2. Synthesis of Mo/Al-SSP. Mo/Al-SSP catalysts were prepared by impregnation of Mo precursor onto the Al-SSP obtained above. First, the desired amount of ammonium heptamolybdate-tetrahydrate was dissolved in DI water. Secondly, this solution was added into the Al-SSP. The Mo/Al-SSP catalyst was dried at  $110^{\circ}$ C for 4 h and calcined in air at  $550^{\circ}$ C for 4 h. The Mo-doped Al-SSP catalyst was denoted as X Mo/Al-SSP, where X (1 and 5 wt%) indicates the wt% of molybdenum.

2.3. Characterization of Catalysts. The bulk phase of catalyst was determined by SIEMENS D500 X-ray diffractometer (XRD), using  $\text{CuK}_{\alpha}$  radiation with Ni filter in the  $2\theta$  range of 10–90 degrees having the resolution of 0.02°.

The surface area and average pore volume of prepared catalysts were determined by  $N_2$ -physisorption using Micromeritics ChemiSorb 2750 Pulse instrument. Measurement was performed at  $-196^{\circ}$ C and calculated according to the Brunauer, Emmet, and Teller (BET) isotherm equation.

The morphology and elemental distribution over the catalysts surface were determined by scanning electron microscope (SEM) and energy X-ray spectroscopy (EDX). The SEM model was JEOL mode JSM-5800LV and Link Isis series 300 program was performed for EDX.

The molybdenum particle dispersion of all catalysts was observed by using JEOL-JEM 200CX transmission electron microscope (TEM) operated at 200 kV.

The acidity of catalysts was estimated by temperature-programmed desorption of ammonia (NH $_3$ -TPD) using Micromeritics Chemisorb 2750 pulse chemisorption system. The catalyst sample was pretreated at 400°C in a flow of helium. The sample was saturated with 15% NH $_3$ /He at 120°C for 1h. After saturation, the physisorbed ammonia was desorbed in a helium gas flow. Then, the sample was heated from 40 to 800°C at a heating rate of 10°C/min. The amount of ammonia in effluent was measured via the thermal conductivity detector (TCD) as a function of temperature [16].

2.4. Ethanol Dehydration Reaction. Activity and product distribution via gas-phase ethanol dehydration reaction of catalysts were determined using a fixed-bed microreactor (I.D. = 7 mm and length = 0.33 m, made from a borosilicate glass tube). A glass reactor was placed into a temperatureprogrammed tubular furnace. All experiments were performed under atmospheric pressure and in the temperature range of 200 to 400°C using a feed composition consisting of 99.95% of ethanol. In this experiment, about 0.05 g of catalyst obtained from Sections 2.2.1 and 2.2.2 was charged into the middle zone of reactor tube and pure ethanol as feed was stored in vaporizer. Prior to testing, the catalyst was activated at 200°C for 1h under argon. Ethanol was conveyed into reactor by argon gas flow rate of 50 mL/min. The reaction was carried out at each temperature for 1 h [17]. The reaction products were analyzed by gas chromatography using the

Catalysts	Surface area (m²/g)	Average pore diameter (nm)	Average pore volume (cm³/g)
Al-SSP	443.6	5.9	0.81
1% Mo/Al-SSP	357.7	7.2	0.59
5% Mo/Al-SSP	492.4	3.9	0.58

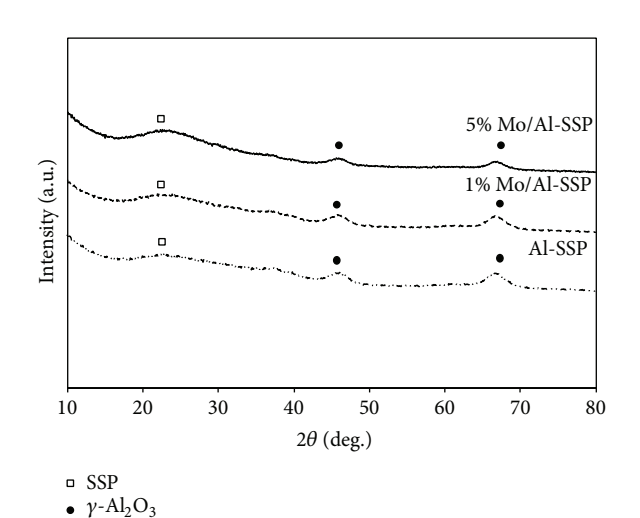


FIGURE 1: XRD patterns of all catalysts.

flame ionization detector (FID), Shimadzu GC14B equipping with DB-5 capillary column.

#### 3. Results and Discussion

3.1. Characteristics of Catalyst. The Al-SSP, 1% Mo/Al-SSP, and 5% Mo/Al-SSP catalysts were characterized using various techniques. To identify the crystalline structure of the catalysts after Mo doping, the X-ray diffraction was performed. As shown in Figure 1, it can be observed that the Al-SSP catalyst exhibited the XRD peaks at 21–24° (broad) indicating the presence of amorphous structure of silica. Besides, the more sharp peaks around 45 and 67° were also observed for this sample indicating the presence of  $\gamma$ -Al<sub>2</sub>O<sub>3</sub> crystallite [18]. However, after doping 1 and 5 wt% of Mo in Al-SSP, both Mo-doped Al-SSP catalysts still exhibited the similar XRD patterns as seen for those of Al-SSP. This revealed that the crystalline structure of the catalysts did not change with Mo doping. In addition, the Mo species cannot be detected because they are present in the highly dispersed form (the crystallite size is less than 3 nm).

The textural properties and nitrogen adsorption/ desorption isotherms of the catalysts are summarized in Table 1 and Figure 2. According to the IUPAC classification, both support and catalysts exhibit Type IV isotherms, which are typical of mesoporous materials. For Al-SSP and 1% Mo/Al-SSP, the sample presented hysteresis loop of Type H1, occurring at higher relative pressure ( $P/P_0 = 0.7$  to 0.9) compared to 5% Mo/Al-SSP catalyst. It indicates larger mesopores and broad pore size distribution with cylindrical

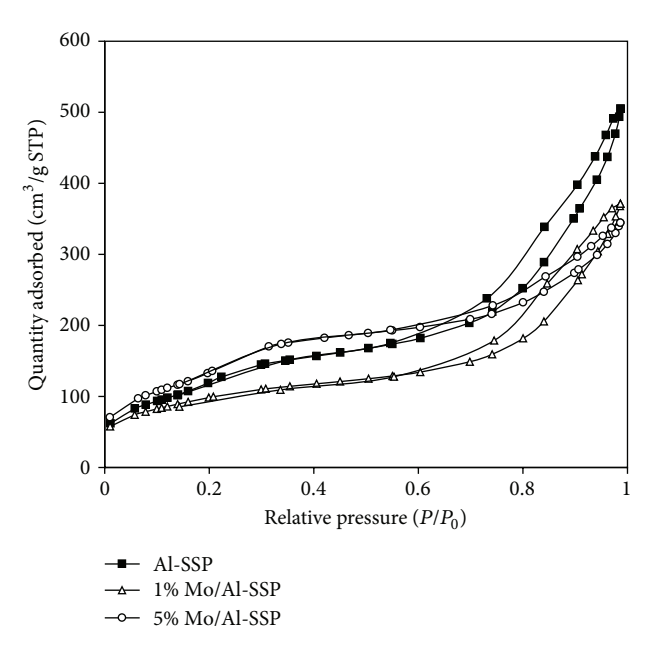


FIGURE 2: Nitrogen adsorption/desorption isotherms of all catalysts.

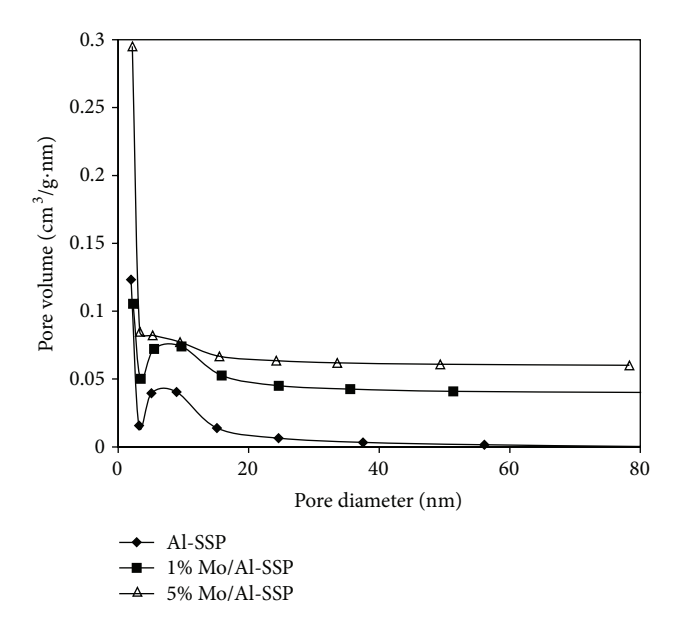


FIGURE 3: BJH pore size distribution of all catalysts.

shapes. The observation is consistent with the value of surface area and sample porosity as shown in Table 1, in which the pore volume of Al-SSP, 1% Mo/Al-SSP, and 5% Mo/Al-SSP was 0.81, 0.59, and 0.58 cm³/g, respectively. The incorporation of molybdenum into Al-SSP decreases the surface area, mainly due to the blockage of pore. Moreover, the pores of this catalyst were blocked, suggesting that the Mo at higher loading (>1 wt%) was not well dispersed in the supports. However, the surface area of 5 wt% Mo did not follow this trend. This may be because the Mo was located on the external surfaces indicating that Mo was not incorporated into the channels of Al-SSP leading to an increase in surface area. The pore size distribution (PSD) calculated by BJH method is shown in Figure 3. For all catalysts, the samples

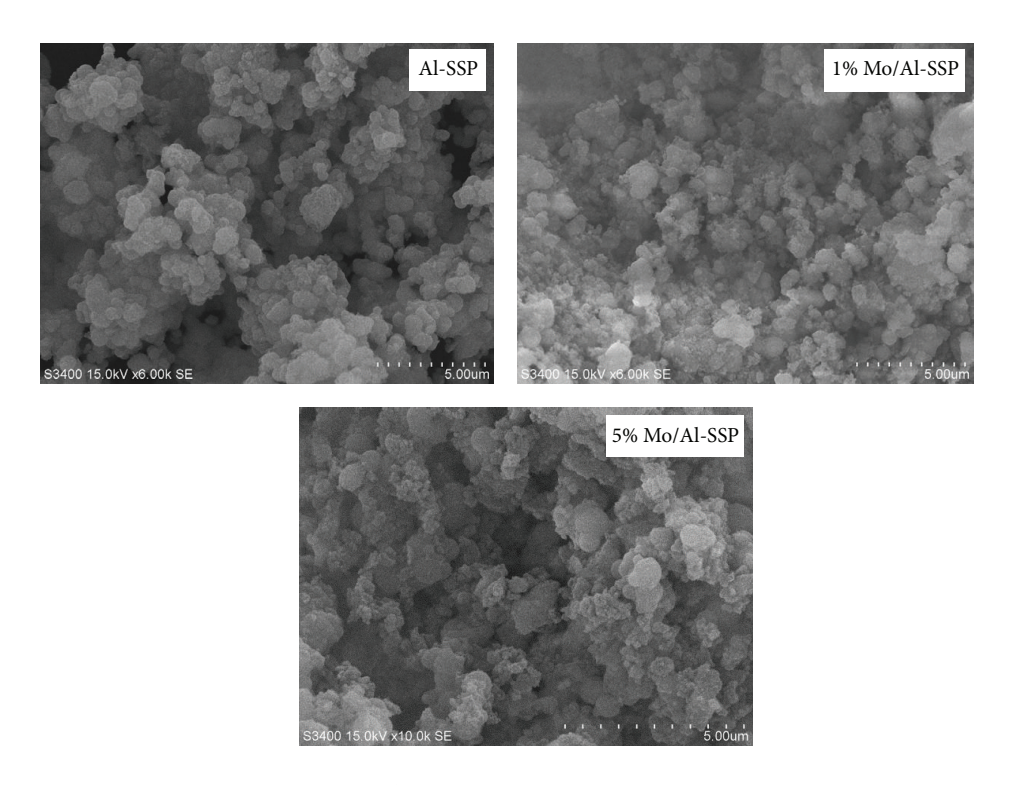


FIGURE 4: The SEM micrographs of all catalysts.

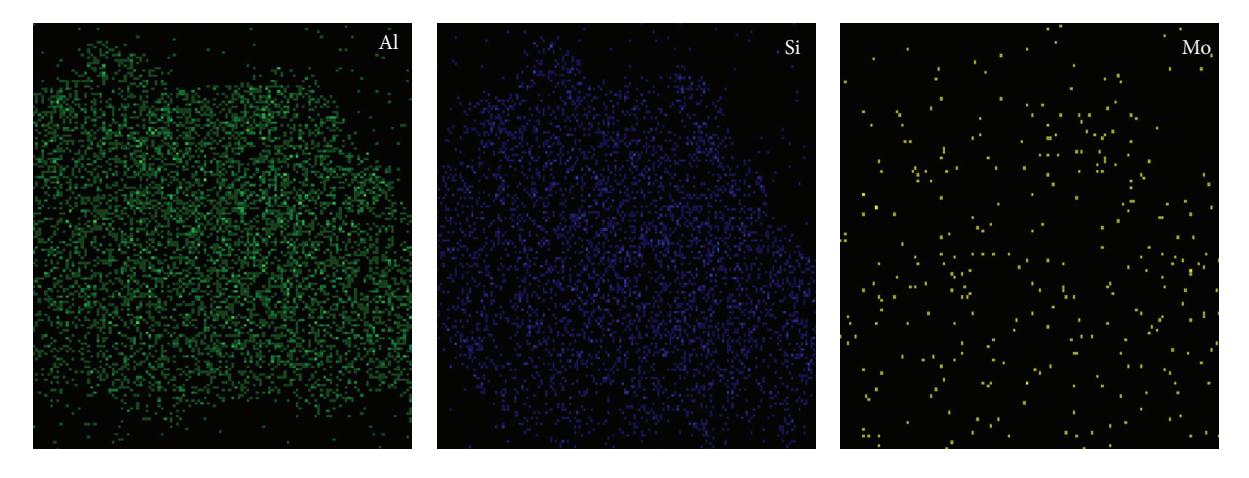


FIGURE 5: The typical EDX mapping of 1% Mo/Al-SSP catalyst.

have a narrow pore size distribution with an average pore diameter around 3.9–7.2 nm, confirming that the pore size distribution is in the mesoporous range. It can be seen that the calculated pore size distribution was in good agreement with  $N_2$  isotherm as mentioned above.

The morphology of the catalysts was determined using SEM as shown in Figure 4. The morphology of the Al-SSP catalyst was apparently spheroidal with agglomeration of particles having the average particle size around 0.5 microns. After doping the Al-SSP with Mo, it can be seen that there was no significant change in the morphology of catalysts.

The dispersive X-ray spectroscopy (EDX) was also performed to determine the elemental distribution in the catalyst granule. All elements such as Al, Si, O, and Mo can be detected using the EDX mapping mode. Hence, the location of the specified element can be illustrated by the dots. The dense of dots is related to the amount of element present. The typical EDX mapping of 1% Mo/Al-SSP catalyst is shown in Figure 5. In this figure, the distribution of Al, Si, and Mo was observed. The density of Al and Si was strongly observed because Al and Si are the main components of Al-SSP catalyst. After Mo doping, the well distribution of Mo was evident. This result

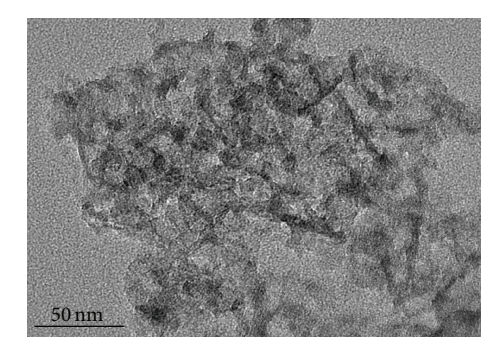


FIGURE 6: The typical TEM image of 1% Mo/Al-SSP catalyst.

TABLE 2: The amount of each element near the surface of catalyst granule obtained from EDX.

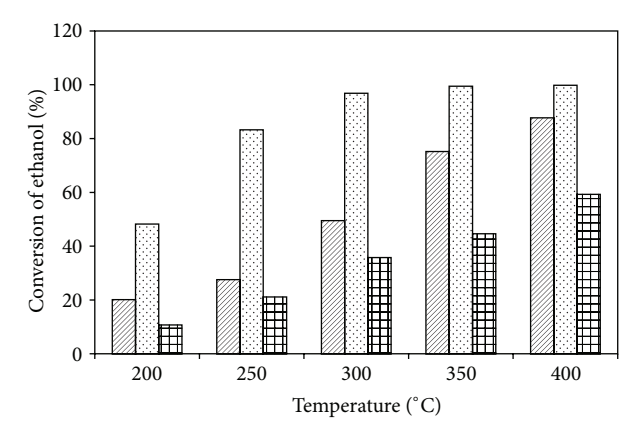
Catalysts	Amo	ount of weight	on surface (w	t%)
Catalysts	Al	Si	O	Mo
Al-SSP	40.6	7.5	51.9	0
1% Mo/Al-SSP	27.2	18.5	49.9	4.4
5% Mo/Al-SSP	13.4	29.3	49.5	7.8

is in accordance with that obtained from XRD, where the Mo species are present in the highly dispersed form, which cannot be detected by the XRD measurement.

Besides the EDX mapping, the amount of each element near the surface of catalyst granule can be determined quantitatively. The results are summarized in Table 2. The key elements to be considered are Al and Mo. It can be seen that mostly Al species (Al = 27.2%) in 1% Mo/Al-SSP catalyst were located at the catalyst surface compared to that in 5% Mo/Al-SSP catalyst (Al = 13.4%). For both Mo-doped Al-SSP catalysts, Mo species were also located at the catalyst surface since the amounts of Mo obtained from EDX were larger than those of Mo loading. The location of Al species could play an important role on the catalytic activity as well.

In order to investigate the dispersion of Mo species, the transmission electron microscope (TEM) image was obtained as shown in Figure 6. It is known that gamma alumina is present as wrinkled sheets located throughout the SSP. As seen from the figure, the dark patches represent the Mo species being dispersed in the alumina wrinkled sheets. It was found that the dispersion of Mo species observed from TEM was corresponding to the very small crystallite size (less than 3 nm) of Mo species obtained from the XRD measurement as mentioned above.

The acid properties of catalysts are crucial to determine the catalytic activity and product distribution via ethanol dehydration reaction. Hence, the  $\mathrm{NH_3}$  temperature-programmed desorption ( $\mathrm{NH_3}\text{-}\mathrm{TPD}$ ) was performed. Table 3 shows the surface acidity of all catalysts in this study. The assignment of desorption peaks between 175 and 300°C is weak acid sites and the desorption peaks occurring above 300°C refer to medium-strong acid sites [19]. It indicates that the Al-SSP catalyst exhibits the lowest amount of weak acid



- □ Al-SSP
- □ 1% Mo/Al-SSP
- 5% Mo/Al-SSP

FIGURE 7: Ethanol conversion at different temperatures of all catalysts.

TABLE 3: The surface acidity of all catalysts from NH<sub>3</sub>-TPD.

	Number of acid sites (mmole/g. cat)					
Catalysts	Weak acid sites	Medium-strong acid sites	Total acid site			
Al-SSP	0.25	1.45	1.70			
1% Mo/Al-SSP	0.33	1.37	1.70			
5% Mo/Al-SSP	0.78	1.11	1.99			

site, whereas the 5% Mo/Al-SSP contains the largest weak and total acid sites. It can be observed that the Mo doping can alter the acidity of Al-SSP catalyst. Adding more amount of Mo apparently resulted in increased significant amount of weak acid site as seen in Table 3. It should be noted that the amount of weak acid site is probably more related to the Brønsted acid site, whereas Lewis acid site is more related to the amount of strong acid site [20]. In ethanol dehydration reaction, the Brønsted acid site is preferred.

3.2. Ethanol Dehydration Reaction. In order to measure the catalytic activity and product distribution, ethanol dehydration reaction was performed over all catalysts at atmospheric pressure with temperature ranging from 200 to 400°C. The results of ethanol conversion for all catalysts are shown in Figure 7. For all catalysts, increased temperature apparently resulted in an increase in ethanol conversion. However, among all catalysts, the 1% Mo/Al-SSP exhibits the highest conversion (ca. 100% conversion at 350°C). It can be observed that the ethanol conversion obtained from 5% Mo/Al-SSP catalyst is the lowest, although this catalyst has the highest amount of weak and total acid sites (Table 3). It should be noted that the amount of Al at catalyst surface for this sample is the lowest based on the EDX result (Table 2). Hence, this is probably the main reason for the 5% Mo/Al-SSP catalyst to yield the lowest conversion.

TABLE 4: Product yield obtained from ethanol dehydration at 30	300°C	J°C
--	-------	-----

Catalysts	Yield of products (wt%)				
Catalysis	Ethylene	Diethyl ether	Acetaldehyde		
Al-SSP	49.07	0.00	0.44		
1% Mo/Al-SSP	90.11	0.68	6.06		
5% Mo/Al-SSP	29.25	1.09	5.45		

Considering the product distribution, the selectivity of ethylene is related to the reaction temperature as also reported by Zhang et al. [21]. Ethylene selectivity is shown in Figure 8. For Al-SSP catalyst, ethylene selectivity was the highest even at low temperature, while it gradually increased for the Mo-doped Al-SSP catalysts with increased temperature. It is suggested that the Mo doping could result in decreased ethylene selectivity, especially at lower temperature. However, the effect of Mo doping is less pronounced at higher temperature.

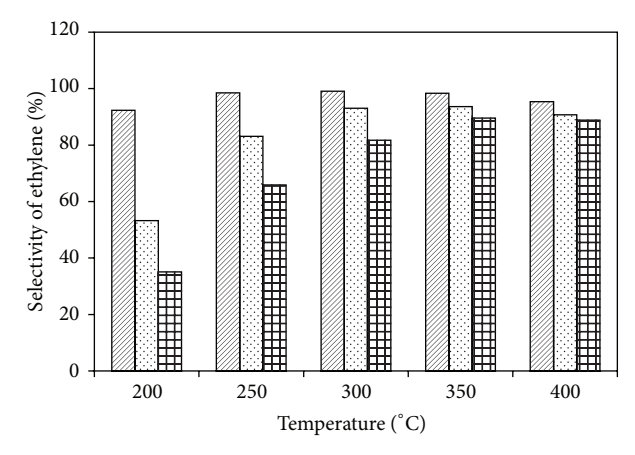
It should be noted that, during ethanol dehydration, byproducts such as diethyl ether (DEE) and acetaldehyde were also obtained. The selectivity of byproduct is shown in Figure 9. At lower temperature (ca. 200 to 300°C), DEE was significantly produced via dehydration of ethanol. At temperature above 350°C, there was no DEE obtained due to its decomposition to ethylene at high temperature. Acetaldehyde is also produced by dehydrogenation of ethanol as a side reaction. As seen from the figure, increased temperature resulted in a slight decrease in selectivity of acetaldehyde, which was also reported by Nair et al. [22].

In order to compare the catalyst performance, the ethylene yield (product of conversion and selectivity) along with other byproducts obtained from ethanol dehydration at 300°C is calculated as shown in Table 4. It was found that the 1% Mo/Al-SSP catalyst rendered the highest ethylene yield with slight amounts of DEE and acetaldehyde. This is attributed to increased weak acid sites and large amount of Al present at the catalyst surface with 1 wt% of Mo doping onto Al-SSP catalyst.

Table 5 shows a comparison of the catalytic ability for ethanol dehydration to ethylene over various catalysts reported so far. It was obvious that 1% Mo/Al-SSP is competitive among other typical and modified catalysts. Finally, it should be emphasized that, apart from their interesting intrinsic activity, the Mo/Al-SSP tested in this study was highly stable, thus making them have potential for industrial applications.

#### 4. Summary

Ethanol dehydration reaction from the temperature range of 200 to 400°C over Al-SSP, 1% Mo/Al-SSP, and 5% Mo/Al-SSP catalysts was investigated. It appears that the 1% Mo/Al-SSP catalyst exhibited the highest ethanol conversion and ethylene yield of ca. 90% (at 300°C). This can be attributed to the increased acidity and proper amount of Al at catalyst surface with Mo doping. However, too large amount of Mo



- Al-SSP
- □ 1% Mo/Al-SSP
- 5% Mo/Al-SSP

FIGURE 8: Ethylene selectivity at different temperatures of all catalysts.

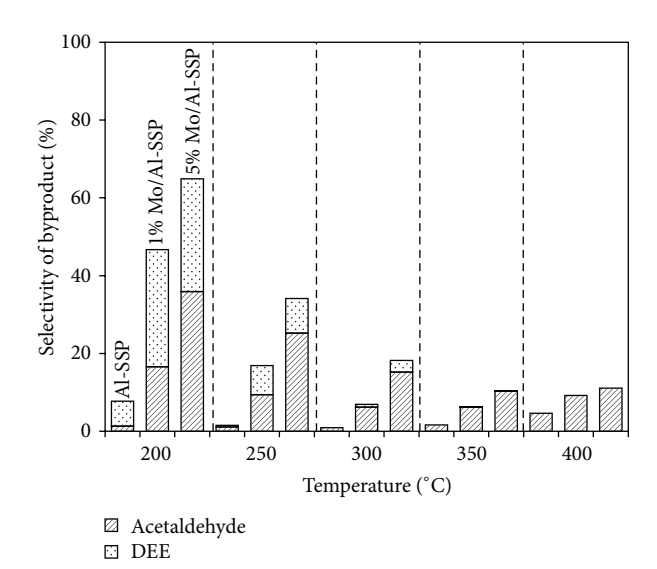


FIGURE 9: The selectivity of byproducts at different temperatures of all catalysts.

doping (i.e., 5 wt%) apparently resulted in decreased amount of Al at catalyst surface leading to low ethanol conversion.

#### **Conflict of Interests**

The authors declare that there is no conflict of interests regarding the publication of this paper.

#### **Acknowledgments**

The authors thank the Thailand Research Fund (BRG5780009 and IRG5780014), National Research University Project, Ratchadaphiseksomphot Endowment Fund (2015) of Chulalongkorn University (CU-58-027-AM), and the National

Catalysts	Surface area (m²/g)	Amount of catalyst	Reaction temperature (°C)	Space velocity (h <sup>-1</sup> )	Ethylene yield (wt%)	Ref.
1% Mo/Al-SSP	357.7	0.05 g	300	WHSV 8.4	90.11	This work
Al-SV	215	0.05 g	250-300	WHSV 8.4	53-100	[17]
$MoO_2$	6	0.15 g	300	* n.a.	19.4	[23, 24]
0.5% La-2% P-HZSM-5	194	0.50 g	200-300	WHSV 2.0	10.2-99.9	[25]
$TiO_2/\gamma$ - $Al_2O_3$	187	1.15 mL	360-550	LHSV 26-104	91.99	[26]
Commercial Al <sub>2</sub> O <sub>3</sub>	190	3.0 mL	450	LHSV 3.0	78.1	[21]

TABLE 5: A comparison of catalysts for ethylene synthesis and their catalytic ability.

Research Council of Thailand (NRCT) for the financial support of this project.

# References

- [1] D. Fan, D.-J. Dai, and H.-S. Wu, "Ethylene formation by catalytic dehydration of ethanol with industrial considerations," *Materials*, vol. 6, no. 1, pp. 101–115, 2013.
- [2] L. Kniel, O. Winter, and K. Stork, *Ethylene, Keystone to the Petrochemical Industry*, M. Dekker, New York, NY, USA, 1980.
- [3] W. R. True, "Global ethylene capacity continues to advance in 2011," December 2015, http://www.ogj.com/articles/print/vol-110/issue-07/special-report-ethylene-report/global-ethylene-capacity.html.
- [4] A. Iles and A. N. Martin, "Expanding bioplastics production: sustainable business innovation in the chemical industry," *Journal of Cleaner Production*, vol. 45, pp. 38–49, 2013.
- [5] E. Voegle, "Feeding the chemical market," Ethanol Producer Magazine, 2012, http://www.ethanolproducer.com/articles/ 8617/feeding-the-chemical-market.
- [6] T. K. Phung, L. Proietti Hernández, and G. Busca, "Conversion of ethanol over transition metal oxide catalysts: effect of tungsta addition on catalytic behaviour of titania and zirconia," *Applied Catalysis A: General*, vol. 489, pp. 180–187, 2014.
- [7] N. K. Kochar, R. Merims, and A. S. Padia, "Ethylene from ethanol," *Chemical Engineering Progress*, vol. 77, no. 6, pp. 66– 70, 1981.
- [8] P. Imhof and J. C. van der Waal, Catalytic Process Development for Renewable Materials, Wiley-VCH, Weinheim, Germany, 2013
- [9] I. Takahara, M. Saito, M. Inaba, and K. Murata, "Dehydration of ethanol into ethylene over solid acid catalysts," *Catalysis Letters*, vol. 105, no. 3-4, pp. 249–252, 2005.
- [10] J. Bedia, R. Barrionuevo, J. Rodríguez-Mirasol, and T. Cordero, "Ethanol dehydration to ethylene on acid carbon catalysts," *Applied Catalysis B: Environmental*, vol. 103, no. 3-4, pp. 302–310, 2011.
- [11] D. P. Debecker, B. Schimmoeller, M. Stoyanova et al., "Flame-made MoO<sub>3</sub>/SiO<sub>2</sub>-Al<sub>2</sub>O<sub>3</sub> metathesis catalysts with highly dispersed and highly active molybdate species," *Journal of Catalysis*, vol. 277, no. 2, pp. 154–163, 2011.
- [12] D. P. Debecker, D. Hauwaert, M. Stoyanova, A. Barkschat, U. Rodemerck, and E. M. Gaigneaux, "Opposite effect of Al on the performances of MoO<sub>3</sub>/SiO<sub>2</sub>-Al<sub>2</sub>O<sub>3</sub> catalysts in the metathesis

- and in the partial oxidation of propene," *Applied Catalysis A: General*, vol. 391, no. 1-2, pp. 78–85, 2011.
- [13] T. Kitano, S. Okazaki, T. Shishido, K. Teramura, and T. Tanaka, "Brønsted acid generation of alumina-supported molybdenum oxide calcined at high temperatures: characterization by acidcatalyzed reactions and spectroscopic methods," *Journal of Molecular Catalysis A: Chemical*, vol. 371, pp. 21–28, 2013.
- [14] J. Janlamool, P. Praserthdam, and B. Jongsomjit, "Ti-Si composite oxide-supported cobalt catalysts for CO<sub>2</sub> hydrogenation," *Journal of Natural Gas Chemistry*, vol. 20, no. 5, pp. 558–564, 2011.
- [15] W. Phongsawat, B. Netiworaruksa, K. Suriye, S. Dokjampa, P. Praserthdam, and J. Panpranot, "Role of support nature ( $\gamma$ -Al<sub>2</sub>O<sub>3</sub> and SiO<sub>2</sub>-Al<sub>2</sub>O<sub>3</sub>) on the performances of rhenium oxide catalysts in the metathesis of ethylene and 2-pentene," *Journal of Natural Gas Chemistry*, vol. 21, no. 2, pp. 158–164, 2012.
- [16] Z. Li, F. Meng, J. Ren, H. Zheng, and K. Xie, "Surface structure and catalytic performance of CuCl/SiO<sub>2</sub>-Al<sub>2</sub>O<sub>3</sub> catalysts for methanol oxidative carbonylation," *Chinese Journal of Catalysis*, vol. 29, no. 7, pp. 643–648, 2008.
- [17] M. Wannaborworn, P. Praserthdam, and B. Jongsomjit, "A comparative study of solvothermal and sol-gel-derived nanocrystalline alumina catalysts for ethanol dehydration," *Journal of Nanomaterials*, vol. 2015, Article ID 519425, 11 pages, 2015.
- [18] F. F. Madeira, N. S. Gnep, P. Magnoux, S. Maury, and N. Cadran, "Ethanol transformation over HFAU, HBEA and HMFI zeolites presenting similar Brønsted acidity," *Applied Catalysis A: General*, vol. 367, no. 1-2, pp. 39–46, 2009.
- [19] J. Handzlik, J. Ogonowski, J. Stoch, M. Mikołajczyk, and P. Michorczyk, "Properties and metathesis activity of molybdena-alumina, molybdena-silica-alumina and molybdena-silica catalysts—a comparative study," *Applied Catalysis A: General*, vol. 312, no. 1-2, pp. 213–219, 2006.
- [20] J. A. Cecilia, C. García-Sancho, J. M. Mérida-Robles, J. Santamaría-González, R. Moreno-Tost, and P. Maireles-Torres, "V and V-P containing Zr-SBA-15 catalysts for dehydration of glycerol to acrolein," *Catalysis Today*, vol. 254, pp. 43–52, 2015.
- [21] X. Zhang, R. Wang, X. Yang, and F. Zhang, "Comparison of four catalysts in the catalytic dehydration of ethanol to ethylene," *Microporous and Mesoporous Materials*, vol. 116, no. 1–3, pp. 210–215, 2008.
- [22] H. Nair, J. E. Gatt, J. T. Miller, and C. D. Baertsch, "Mechanistic insights into the formation of acetaldehyde and diethyl ether from ethanol over supported VO<sub>x</sub>, MoO<sub>x</sub>, and WO<sub>x</sub> catalysts," *Journal of Catalysis*, vol. 279, no. 1, pp. 144–154, 2011.

<sup>\*</sup>n.a. = not applicable.

[23] Y. Nakamura, T. Murayama, and W. Ueda, "Reduced vanadium and molybdenum oxides catalyze the equivalent formation of ethane and acetaldehyde from ethanol," *ChemCatChem*, vol. 6, no. 3, pp. 741–744, 2014.

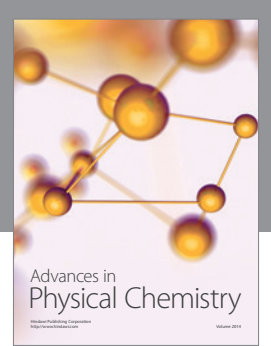
- [24] Y. Nakamura, T. Murayama, and W. Ueda, "Hydrogen-transfer dehydration between alcohols over  $\rm V_2O_3$  and  $\rm MoO_2$  catalysts for the formation of corresponding alkanes and aldehydes," *Journal of Molecular Catalysis A: Chemical*, vol. 394, pp. 137–144, 2014.
- [25] N. Zhan, Y. Hu, H. Li, D. Yu, Y. Han, and H. Huang, "Lanthanum-phosphorous modified HZSM-5 catalysts in dehydration of ethanol to ethylene: a comparative analysis," *Catalysis Communications*, vol. 11, no. 7, pp. 633–637, 2010.
- [26] G. Chen, S. Li, F. Jiao, and Q. Yuan, "Catalytic dehydration of bioethanol to ethylene over  ${\rm TiO_2/\gamma\text{-}Al_2O_3}$  catalysts in microchannel reactors," *Catalysis Today*, vol. 125, no. 1-2, pp. 111–119, 2007.

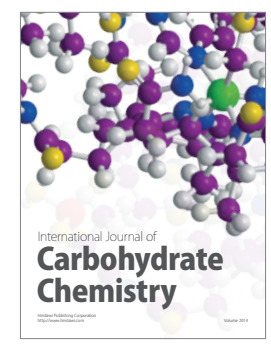
















Submit your manuscripts at http://www.hindawi.com

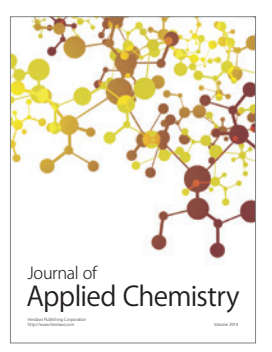


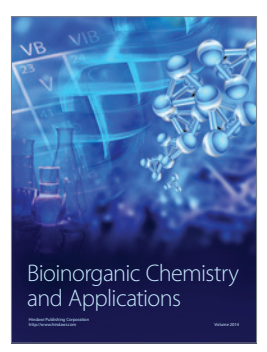




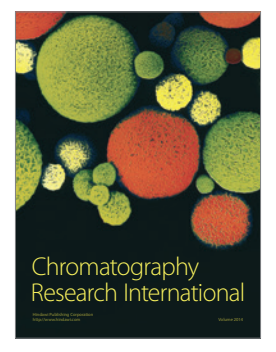






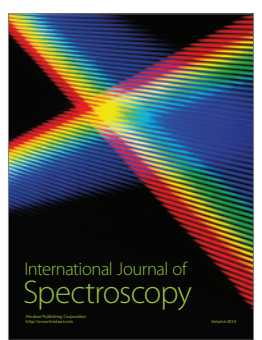












Hindawi Publishing Corporation Journal of Nanomaterials Volume 2017, Article ID 5018384, 9 pages https://doi.org/10.1155/2017/5018384



# Research Article

# Effect of Calcination Temperatures and Mo Modification on Nanocrystalline $(\gamma-\chi)$ -Al<sub>2</sub>O<sub>3</sub> Catalysts for Catalytic Ethanol Dehydration

# Tharmmanoon Inmanee, Piriya Pinthong, and Bunjerd Jongsomjit

Center of Excellence on Catalysis and Catalytic Reaction Engineering, Department of Chemical Engineering, Faculty of Engineering, Chulalongkorn University, Bangkok 10330, Thailand

Correspondence should be addressed to Bunjerd Jongsomjit; bunjerd.j@chula.ac.th

Received 9 August 2016; Revised 15 December 2016; Accepted 22 December 2016; Published 12 January 2017

Academic Editor: Pedro D. Vaz

Copyright © 2017 Tharmmanoon Inmanee et al. This is an open access article distributed under the Creative Commons Attribution License, which permits unrestricted use, distribution, and reproduction in any medium, provided the original work is properly cited.

The mixed gamma and chi crystalline phase alumina (M-Al) catalysts prepared by the solvothermal method were investigated for catalytic ethanol dehydration. The effects of calcination temperatures and Mo modification were elucidated. The catalysts were characterized by X-ray diffraction (XRD),  $N_2$  physisorption, transmission electron microscopy (TEM), and  $NH_3$ -temperature programmed desorption ( $NH_3$ -TPD). The catalytic activity was tested for ethylene production by dehydration reaction of ethanol in gas phase at atmospheric pressure and temperature between 200°C and 400°C. It was found that the calcination temperatures and Mo modification have effects on acidity of the catalysts. The increase in calcination temperature resulted in decreased acidity, while the Mo modification on the mixed phase alumina catalyst yielded increased acidity, especially in medium to strong acids. In this study, the catalytic activity of ethanol dehydration to ethylene apparently depends on the medium to strong acid. The mixed phase alumina catalyst calcined at  $600^{\circ}$ C (M-Al-600) exhibits the complete ethanol conversion having ethylene yield of 98.8% (at  $350^{\circ}$ C) and the Mo-modified catalysts promoted dehydrogenation reaction to acetaldehyde. This can be attributed to the enhancement of medium to strong acid with metal sites of catalyst.

#### 1. Introduction

Ethylene is intermediate in the petroleum industry and used as feedstocks to produce a variety of polymers in petrochemical industry such as polyethylene, polyvinyl chloride, and polystyrene. Therefore, the demand of ethylene continually increases. The total consumption of ethylene and other light olefins was around 174 millions of tons in 2004. It continuously increased up to 205 million tons in 2010 and it is predicted to grow up to 259 million tons in 2016 [1]. Moreover, ethylene is used as the precursor for synthesis of ethylene oxide, ethylene dichloride, ethylbenzene, and so on [2-5]. Traditionally, ethylene is obtained from the thermal catalytic cracking of petroleum and natural gas upon an endothermic reaction requiring high temperatures (600°C-1000°C) [2]. Since petroleum is nonrenewable resource, the new suitable way to produce ethylene from renewable resource is considered [6]. Hence, the dehydration of ethanol has been considered as a promising alternative approach to produce ethylene instead of using petroleum as feedstock.

Dehydration of ethanol over solid acid catalysts requires lower temperature compared to the thermal cracking, leading to the reduction of energy cost. Therefore, many researchers have developed the ethanol dehydration for producing ethylene using solid catalysts. The main product from this reaction is ethylene, whereas diethyl ether, acetaldehyde, and light olefins are byproducts. The acid nature of solid catalyst has direct influence on the dehydration activity. The common solid catalysts such as zeolites [2, 7, 8] and alumina ( $Al_2O_3$ ) [3, 9] have been applied to study the effect of acidity of catalyst on the dehydration ability. Lu et al. (2011) [7] found that HZSM-5 zeolite catalyst exhibits the highest selectivity of ethylene when it was carried out at low temperature (200°C-300°C). However, HZSM-5 zeolites have too high acidity, which can be rapidly deactivated by coke formation. The formation of coke on the catalyst causes lower stability. Previous works

have been reported that acidity not only strongly affected the dehydration ability but also influenced the reaction stability of catalyst. For  $\gamma\text{-Al}_2\mathrm{O}_3$  catalyst, the dehydration reaction must be applied at higher temperature (400–450°C) to achieve high activity. Therefore, many attempts have been tried to modify  $\gamma\text{-Al}_2\mathrm{O}_3$  by adding metal oxide on solid support such as iron oxide and titanium oxide [10, 11]. Chen et al. (2007) [11] found that the modification of  $\gamma\text{-Al}_2\mathrm{O}_3$  with TiO $_2$  can improve acidity. The conversion of ethanol is reached to 99.96%, whereas ethylene selectivity is about 99.4% at 440°C. Although the modified  $\gamma\text{-Al}_2\mathrm{O}_3$  catalyst required higher temperature than HZSM-5 zeolite catalyst, it is easy to synthesize and the stability of modified  $\gamma\text{-Al}_2\mathrm{O}_3$  catalyst is better.

 $\gamma$ -Al<sub>2</sub>O<sub>3</sub> catalyst is interesting because of its excellent thermal stability, fine particle size, high surface area, and side reaction inhibition. Khom-in et al. (2008) [12] studied the synthesis of mixed  $\gamma$ - and  $\chi$ -phase Al<sub>2</sub>O<sub>3</sub> catalysts and applied for methanol dehydration. They reported that the acidity of mixed  $\gamma$ - and  $\chi$ -phase  $Al_2O_3$  is higher than  $\gamma$ - $Al_2O_3$  and  $\chi$ - $Al_2O_3$  [13, 14]. The mixed  $\gamma$ - and  $\chi$ -phase  $Al_2O_3$ catalysts can be directly synthesized via solvothermal method by using the suitable solvent in order to control structures, grain sizes, and morphologies by varying process conditions. In this research, we focused on the development of the alumina-based solid acid catalysts for ethanol dehydration. The catalysts were synthesized, characterized, and tested at a specified reaction condition. The synthesis parameters, such as calcination temperature and Mo modification influencing dehydration reaction, were varied in order to explore the suitable catalysts for ethanol dehydration.

# 2. Experimental

- 2.1. Preparation of Mixed Phase Alumina Catalyst. The mixed  $\gamma$  and  $\chi$ -crystalline phase alumina (M-Al) were prepared by the solvothermal method as reported by Janlamool and Jongsomjit [15]. The obtained powders were calcined in a tube furnace at different temperatures including 400°C (M-Al-400), 600°C (M-Al-600), 800°C (M-Al-800), and 1000°C (M-Al-1000) with a heating rate of 10°C/min in air for 6 h.
- 2.2. Preparation of Mo-Modified M-Al Catalysts. The Momodified M-Al catalysts were prepared by impregnation of the mixed phase alumina with an aqueous solution of ammonium heptamolybdate-tetrahydrate [(NH<sub>4</sub>)<sub>5</sub>Mo<sub>7</sub>O<sub>34</sub>·4H<sub>2</sub>O] with various loadings of Mo (5, 10, 15, and 20 wt%). The procedure for preparation catalyst as mentioned above was calculated based on 1g of catalyst used. First, ammonium heptamolybdate-tetrahydrate was dissolved in 0.6 mL of deionized water. Then, the solution was added dropwise into approximately 1 g of dried solid catalyst. The obtained catalyst was dried in air at room temperature for 24 h, dried in oven at 110°C for 6 h, and calcined in air at 500°C for 2 h.

#### 2.3. Catalyst Characterization

*2.3.1. X-Ray Diffraction (XRD).* The X-ray diffraction (XRD) patterns relating to bulk crystal structure of the catalysts were

determined by the SIEMENS D5000 X-ray diffractometer. The experiment was carried out using Cu  $K_{\alpha}$  radiation source ( $\lambda = 1.54439 \text{ Å}$ ) with Ni filter in the  $2\theta$  range of 20 to  $80^{\circ}$  with a resolution of  $0.02^{\circ}$ .

- 2.3.2. Nitrogen Physisorption. The BET surface area, pore volume, and pore diameter of catalysts were determined by nitrogen gas adsorption at liquid nitrogen temperature (-196°C) using Micromeritics ChemiSorb 2750 Pulse chemisorption system instrument.
- 2.3.3. Transmission Electron Microscopy (TEM). The morphology and crystallite size of all catalysts were observed by using JEOL-JEM 200CX transmission electron microscope operated at 100 kV.
- 2.3.4. Temperature Programmed Adsorption (NH<sub>3</sub>-TPD). The acid properties of catalysts were investigated by temperature-programmed desorption of ammonia (NH<sub>3</sub>-TPD) equipment using Micromeritics ChemiSorb 2750 Pulse Chemisorption System. 0.1g of catalyst was loaded in a quartz tube and pretreated at 500°C under helium flow. The sample was saturated with 15% NH<sub>3</sub>/He. After saturation, the physisorbed ammonia was desorbed under helium gas flow about 30 min, and then it was heated from 40°C to 800°C at heating rate of 10°C/min.
- 2.4. Reaction Test. The dehydration of ethanol was carried out in a fixed-bed continuous flow reactor with an inner diameter of 7 mm. In the experiment, 0.05 g of catalyst was loaded into the reactor and pretreated in argon (50 mL/min) at 200°C for 1h under atmospheric pressure. To start the reaction, ethanol was delivered by bubbling argon as a carrier gas through the saturator at 45°C to control the vapor pressure of ethanol with WHSV of 8.4 ( $g_{ethanol}g_{cat}^{-1}\cdot h^{-1}$ ). The reaction was carried out in temperature ranging from 200°C to 400°C. The products were analyzed by a Shimadzu GC8A gas chromatograph with FID using capillary column (DB-5) at 150°C.

#### 3. Results and Discussion

#### 3.1. Effect of Calcination Temperature

3.1.1. Characteristics. The mixed phase alumina catalysts, calcined at different temperatures, were confirmed by XRD results (Figure 1). It was found that the XRD patterns of M-Al-400, M-Al-500, M-Al-600, M-Al-700, M-Al-800, and M-Al-900 (calcined at 400°C to 900°C) were similar. These patterns indicated the presence of  $\gamma$ -crystalline (32°, 37°, 39°, 45°, 61°, and 66°) and  $\chi$ -crystalline (37°, 40°, 43°, 46°, 60°, and 67°) phases of alumina [12]. However, the M-Al-1000 catalyst (calcined at 1000°C) exhibits the different XRD pattern due to phase transformation to delta and theta phases [16].

BET surface area, pore volume, and pore size diameter of catalysts with various calcination temperatures are summarized in Table 1. The BET surface area slightly decreased with increasing calcination temperature. Surface area decreased

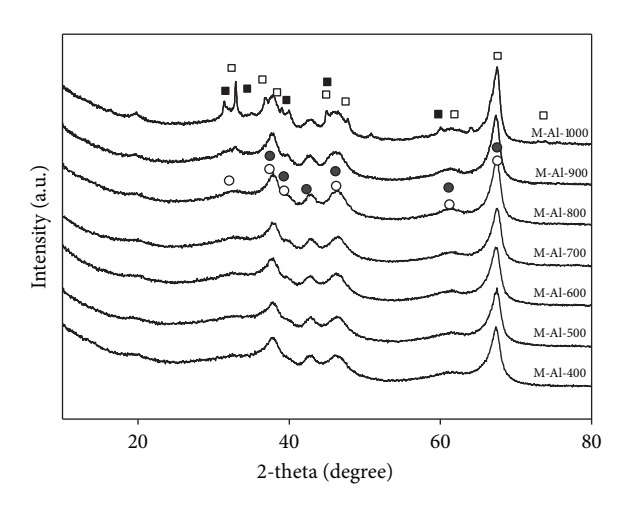


FIGURE 1: XRD patterns of mixed  $\gamma$ - and  $\chi$ -crystalline phase alumina catalysts with various calcination temperatures; ( $\bigcirc$ ) gamma-alumina, ( $\bigcirc$ ) chi-alumina, ( $\square$ ) theta-alumina, and ( $\blacksquare$ ) delta-alumina.

Table 1: BET surface area, pore volume, and pore size diameter of the mixed  $\gamma$ - and  $\chi$ -crystalline phase alumina.

Sample	BET surface area (m²/g)	Pore volume (cm <sup>3</sup> /g)	Pore size diameter (nm)
M-Al-400	233	0.53	5.94
M-Al-500	191	0.54	7.29
M-Al-600	187	0.57	8.09
M-Al-700	157	0.51	8.39
M-Al-800	149	0.51	8.51
M-Al-900	142	0.49	8.98
M-Al-1000	114	0.42	9.41

from 233 to  $144\,\mathrm{m^2/g}$  with calcination temperature from  $400^\circ\mathrm{C}$  to  $1000^\circ\mathrm{C}$ . The pore volume of alumina catalysts seems to be constant with an increase in the calcination temperature. The M-Al-600 shows the highest pore volume  $(0.57\,\mathrm{cm^3/g})$ . All catalysts exhibited increased pore size diameter from 5.9 to 9.1 nm with increasing calcination temperature. It is suggested that an increase in calcination temperature aggregated the catalyst resulting in losing the surface area, increasing the pore sizes diameter, and decreasing the pore volume.

From the previous work, it was suggested that an increase of calcination temperature insignificantly affects the morphologies of mixed  $\gamma$ - and  $\chi$ -crystalline phase alumina catalysts. However, Pansanga et al. [13] reported the morphology of mixed phase alumina, which was obtained by transmission electron microscopy (TEM) technique. They found that the morphology of alumina with different phases presented different structure. The morphologies of mixed  $\gamma$ - and  $\chi$ -crystalline-phase alumina exhibited wrinkled sheets and spherical particles of  $\gamma$ - and  $\chi$ -crystalline phase alumina, respectively.

Figure 2 shows the TEM micrographs of the M-Al-400 and M-Al-1000. It confirms that the obtained catalysts

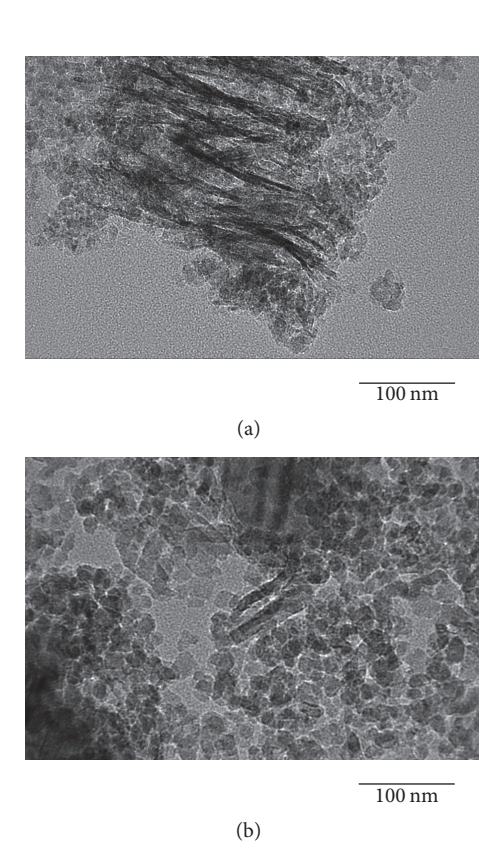


FIGURE 2: TEM micrographs of the (a) M-Al-400 and (b) M-Al-1000.

contain the mixed  $\gamma$ - and  $\chi$ -crystalline-phase alumina indicating wrinkled sheets and spherical particles, according to Pansanga et al. [13]. The calcination temperature significantly affects the phase transformation as seen from XRD and TEM. Figure 2(a) shows two types of morphologies, which is mixed phase of  $\gamma$ - and  $\chi$ -alumina calcined at 400°C. When the calcination temperature was increased to 1000°C, XRD suggested that the phase transformation occurred. It was proven by TEM as seen in Figure 2(b) that it appears as spherical particles and scarcely wrinkled sheets. It is suggested that the wrinkled sheets (γ-phase alumina) were transformed to other phase, while the spherical particles ( $\chi$ phase alumina) remain unchanged. It is in good agreement with the XRD result as seen for the peaks of M-Al-1000 at 43°. This indicated that  $\chi$ -phase alumina was still observed. On the other hand, the peaks of  $\gamma$ -phase alumina were observed differently.

The total acidity was significantly decreased with increasing the calcination temperature (Table 2). This is because the hydroxyl group on catalyst surface was released with increasing the calcination temperature, leading to lower acidity. Besides, the total acidity can be divided into two types of acidic sites: weak acid sites and medium to strong acid sites. For weak acid sites, the position of weak acid sites exhibited the amount of NH $_3$  desorption in the range from 215 to 109  $\mu$ mol NH $_3$ /g cat. The M-Al-400 exhibited the highest acidity. However, the position of medium to strong acid sites was presented in the range from 705 to 337  $\mu$ mol NH $_3$ /g cat.

Table 2: The amount of acidity of mixed $\gamma$ - and $\chi$ -crystalline-phase
alumina catalysts with various calcination temperatures.

Sample	NH <sub>3</sub> desorption ( $\mu$ mol NH <sub>3</sub> /g cat.)		Total acidity
1	Weak	Medium to strong	(μmol NH <sub>3</sub> /g cat.)
M-Al-400	215	489	705
M-Al-500	195	494	689
M-Al-600	148	513	661
M-Al-700	155	387	542
M-Al-800	109	364	473
M-Al-900	172	230	402
M-Al-1000	146	191	337

3.1.2. Reaction Study. The catalytic performance of all catalysts was tested in ethanol dehydration. The reaction was carried out in the temperature ranging from 200°C to 400°C. The catalytic activity depends on the operating temperature, according to previous reports [7, 8, 10]. The results of catalytic activity were reported in terms of conversion and selectivity versus temperature profile. Besides the operating temperature, the catalyst acidity is an important factor influencing the conversion and selectivity of ethanol.

The acidity results are summarized in Table 2. The M-Al-600 exhibited the highest medium to strong acidity, followed by the M-Al-500 and M-Al-400. This result is in agreement with the previous report [17], in which the dehydration of ethanol over acid catalyst was studied and it was found that the products of ethanol dehydration reaction are ethylene (main product), diethyl ether, and acetaldehyde. The ethylene formation is favored by medium to strong acid sites, whereas diethyl ether requires only weak acid sites. At low temperature, diethyl ether is the major product, while, at high temperature, ethylene prevails. For the M-Al-1000, it exhibited the lowest medium to strong acidity.

The ethanol conversion increased with increasing reaction temperature (Figure 3). Similar trend was observed for all catalysts. The M-Al-400, M-Al-500, and M-Al-600 catalysts showed good performance with near complete ethanol conversion. However, at temperature higher than 400°C, deactivation can occur and products can be further converted to other products [16]. Considering the relationship between acidity and ethanol conversion, it was found that the medium to strong acidity plays an important role in the ethanol conversion. At high temperature, the selectivity of ethylene for all catalysts was higher than that at low temperature as shown in Figure 4.

On the contrary, the selectivity of diethyl ether apparently decreased with increasing temperature as seen in Figure 5. This result can be ascribed by thermodynamic properties. The reaction of ethanol to ethylene is endothermic reaction. Thus, it requires high temperature. On the other hand, the reaction of ethanol to diethyl ether is exothermic reaction; therefore diethyl ether is favored at the lower temperature. For the selectivity of acetaldehyde, it is presented in Figure 6. It was found that acetaldehyde selectivity was almost similar for all catalysts except for the M-Al-900 and M-Al-1000. In

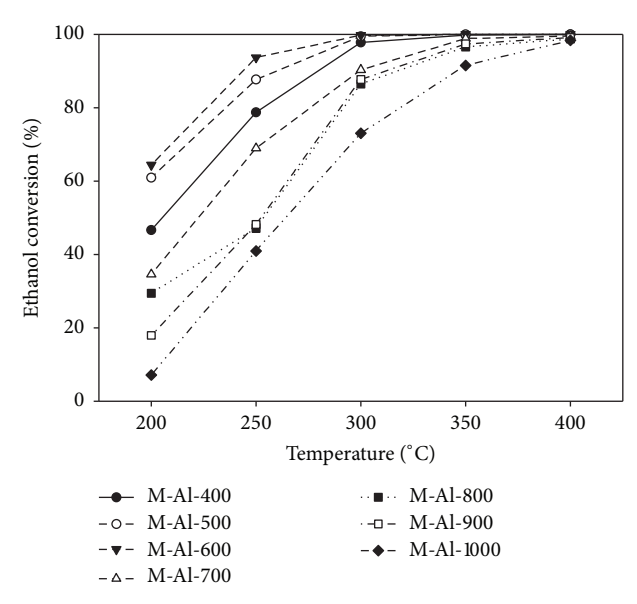


FIGURE 3: Ethanol conversion profiles in ethanol dehydration at different temperatures.

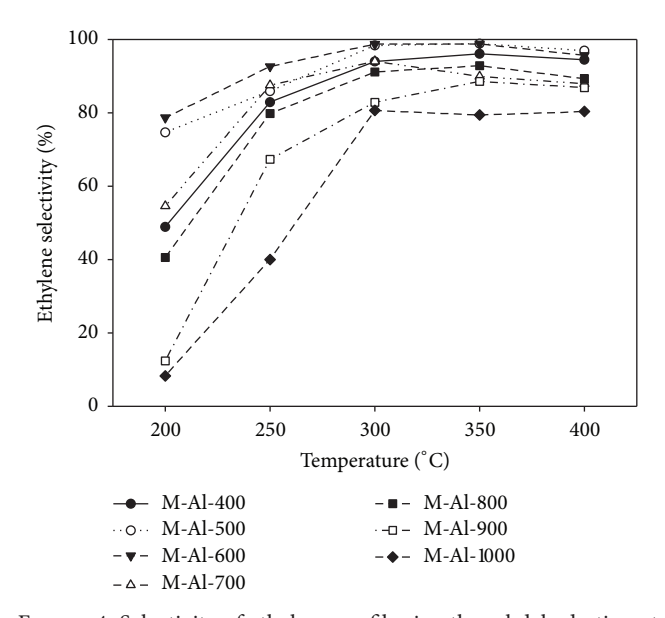


FIGURE 4: Selectivity of ethylene profiles in ethanol dehydration at different temperatures.

summary, the M-Al-600 catalyst shows the highest ethanol conversion (99.98%) and ethylene selectivity of 98.76% at 350°C having the ethylene yield of 98.75% (Table 3) at this temperature.

#### 3.2. Effect of Mo Modification

3.2.1. Characteristics. X-ray diffraction patterns of Momodified M-Al-600 catalyst are shown in Figure 7. It can be seen for 5Mo/M-Al-600 and 10Mo/M-Al-600 that no distinguishable peaks of Mo species were observed in XRD

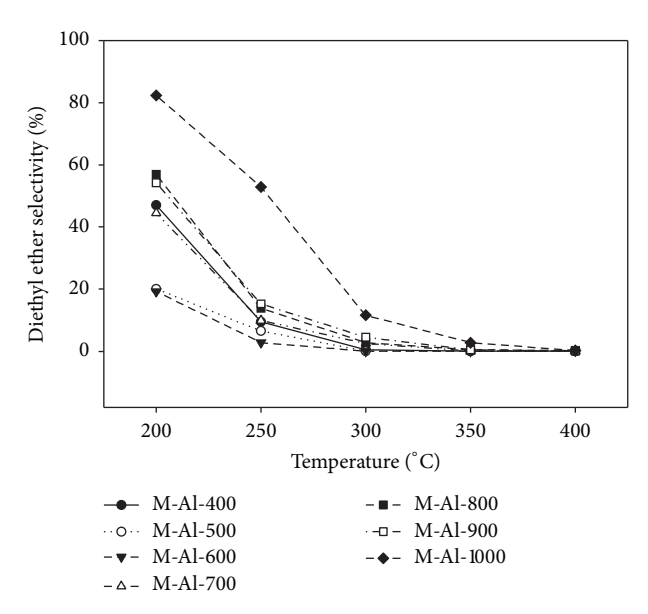


FIGURE 5: Selectivity of diethyl ether profiles in ethanol dehydration at different temperatures.

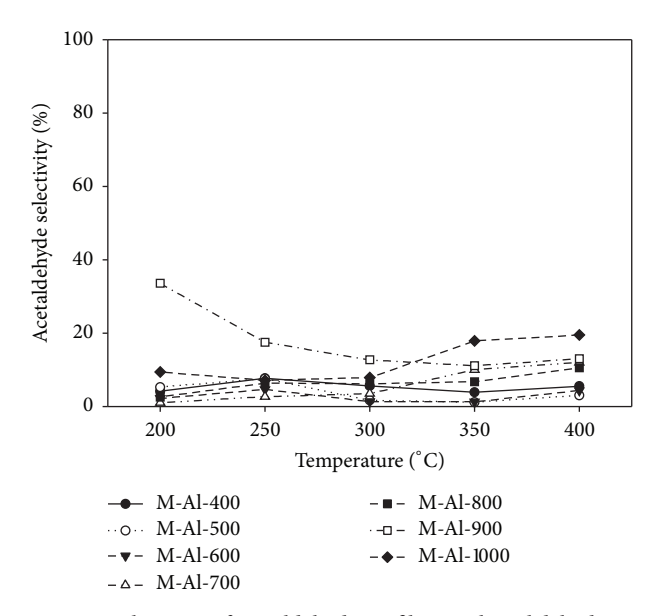


FIGURE 6: Selectivity of acetaldehyde profiles in ethanol dehydration at different temperatures.

Table 3: The yield of ethylene of M-Al-600 catalyst.

Reaction	Ethanol	Ethylene	Ethylene yield
temperature (°C)	conversion (%)	selectivity (%)	(%)
200	64.38	78.65	50.63
250	93.68	92.59	86.74
300	99.74	98.67	98.41
350	99.98	98.76	98.75
400	100.00	95.57	98.57

patterns. Only XRD peaks for the mixed  $\gamma$ - and  $\chi$ -crystalline-phase alumina were observed. It indicates that, at low Mo loading (<10 wt%), Mo was well dispersed on alumina surface. The sample with high amount of Mo (15 wt%–20 wt%),

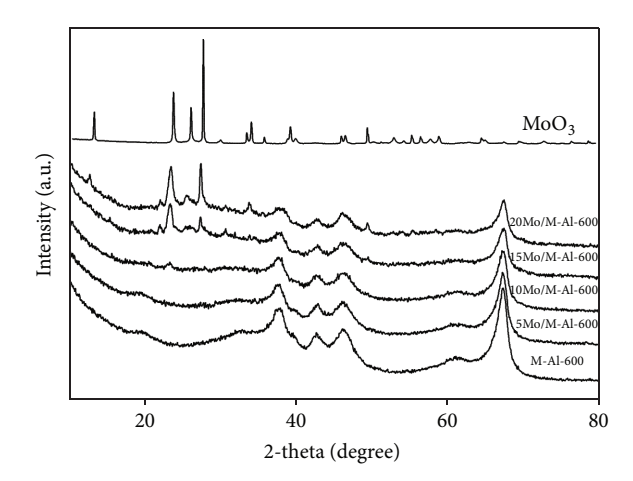


FIGURE 7: XRD patterns of mixed  $\gamma$ - and  $\chi$ -crystalline phase alumina, MoO<sub>3</sub>-modified alumina, and MoO<sub>3</sub>.

TABLE 4: BET surface area, pore volume, and pore size diameter of the MoO<sub>3</sub>-modified catalysts.

Sample	BET surface area (m <sup>2</sup> /g)	Pore volume (cm <sup>3</sup> /g)	Pore size diameter (nm)
	( / 8/	(**** 787	
M-Al-600	187	0.57	8.09
5Mo/M-Al-600	185	0.45	6.88
10Mo/M-Al-600	164	0.43	7.20
15Mo/M-Al-600	134	0.35	7.12
20Mo/M-Al-600	131	0.35	6.74

showed XRD peaks at  $2\theta$  of  $27.3^{\circ}$ ,  $25.7^{\circ}$ , and  $23.3^{\circ}$ , which are characteristics of MoO<sub>3</sub> [12]. The intensity of the diffraction peak can be attributed to an increase of MoO<sub>3</sub> species indicating the formation of crystalline MoO<sub>3</sub> on alumina surface.

BET surface area, pore volume, and pore size diameter of Mo-modified catalysts are summarized in Table 4. The BET surface area and pore volume were decreased with an increase of MoO<sub>3</sub> loading. This may be due to the accumulation of the MoO<sub>3</sub> on alumina surface. Although the 5Mo/M-Al-600 and 10Mo/M-Al-600 did not reveal the MoO3 species, the BET surface area, pore volume, and pore size diameter of both catalysts were decreased. In addition, from Table 4, the impregnation with MoO<sub>3</sub> apparently lowered BET surface area and pore volume of support but did not significantly change the porous structure. The reduction of surface area was caused by blockage of smaller pore by MoO<sub>3</sub> particles, while it did not affect the larger pore. As a result, the average pore size diameter of modified catalyst was not significantly changed. It was in the range of 6.74 to 7.20 nm. This indicated that, at lower loading, MoO<sub>3</sub> was well dispersed on the support surface probably as the monolayer [18]. However, at higher MoO<sub>3</sub> loading (20Mo/M-Al-600), the decrease of the BET surface area and pore volume because the formation of MoO<sub>3</sub> crystallites obstructs the small pores and/or surface of catalysts is clearly seen. The pore size diameter of modified catalyst was in the range of 6.74 to 7.20 nm, which was lower

Sample	NH <sub>3</sub> desorp	ption (μmol NH <sub>3</sub> /g cat.)	Total acidity (µmol NH <sub>3</sub> /g cat.)
	Weak	Medium to strong	Total acidity (µmol N113/g cat.)
M-Al-600	148	513	661
5Mo/M-Al-600	289	634	923
10Mo/M-Al-600	249	727	977
15Mo/M-Al-600	220	795	1015
20Mo/M-Al-600	263	851	1114

TABLE 5: The amount of acidity of MoO<sub>3</sub>-modified catalysts.

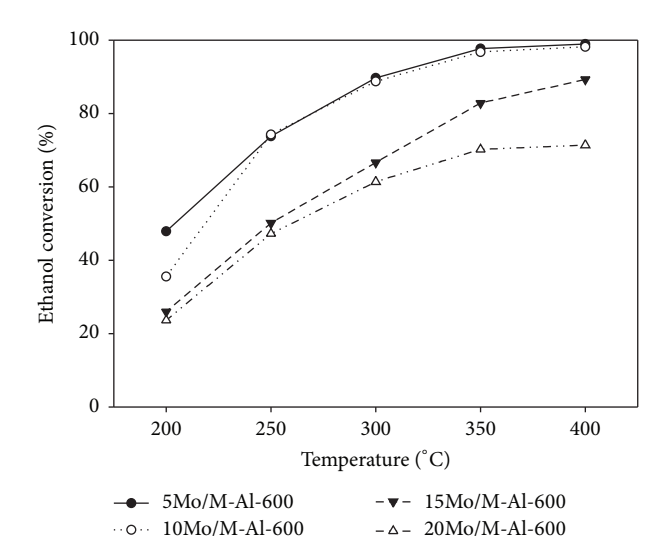


FIGURE 8: Ethanol conversion profiles in ethanol dehydration of the MoO<sub>3</sub> over mixed  $\gamma$ - and  $\chi$ -crystalline phase alumina catalysts.

than M-Al-600. This result is due to the covering of MoO<sub>3</sub> crystallites on surface and pore of catalysts.

The total acidity was enhanced explicitly with an increase in the  $MoO_3$  loading (Table 5), especially the medium to strong acid sites  $(634\,\mu\mathrm{mol}\ \mathrm{NH_3/g}\ \mathrm{cat.}$  for the  $5\mathrm{Mo/M}$ -Al-600 compared to  $851\,\mu\mathrm{mol}\ \mathrm{NH_3/g}\ \mathrm{cat.}$  for the  $20\mathrm{Mo/M}$ -Al-600). This is suggested that the addition of  $MoO_3$  has a significant effect on the acidity of the mixed phase alumina catalysts. Although, the increased acidity with the  $MoO_3$  loading cannot be identified in terms of Lewis and Brønsted acidity, Heracleous et al. [19] suggested that the new acid sites generated from the introduction of Mo are of Brønsted species, while only Lewis acid sites were identified on the alumina support [20–22].

3.2.2. Reaction Study. The Mo-modified M-Al-600 catalysts with various Mo loadings were tested in ethanol dehydration reaction. The ethanol conversion over different catalysts is shown in Figure 8. It displays the similar trend to the ethanol conversion of the M-Al-600, where it increased with increasing operating temperatures. When comparing the Mo-modified alumina series with the unmodified catalysts (M-Al-600), it was found that the ethanol conversion of modified alumina was lower than that of the M-Al-600, although the modified alumina had more amount of acidity

TABLE 6: Turnover frequency of the acid and Mo sites.

	Turnover frequency (s <sup>-1</sup> )	
Acid sites <sup>a</sup>		Mo sites <sup>b</sup>
84.4		$4.70 \times 10^{-3}$

 $<sup>^{\</sup>rm a} \rm Based$  on dehydration reaction of ethanol to ethylene of the M-Al-600 at 200  $^{\circ} \rm C$  .

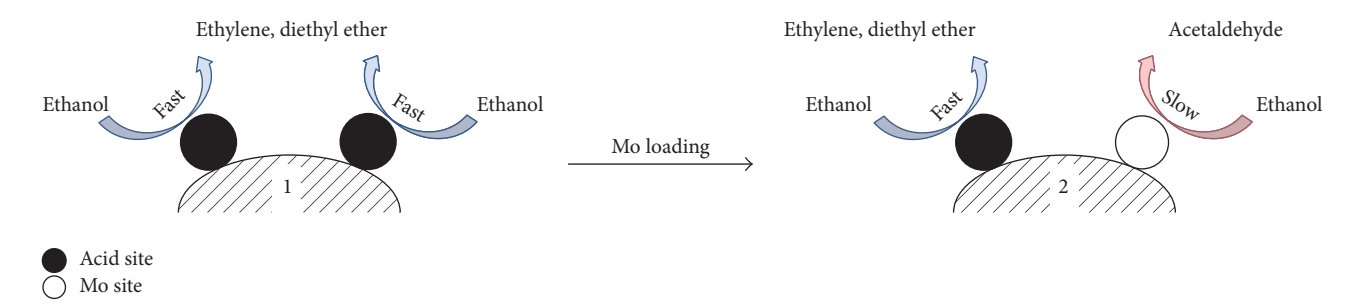
than the M-Al-600 catalyst. The reason why the higher total acidity did not render high ethanol conversion can be proposed upon Scheme 1. From Scheme 1, it is assumed that the acid site converts the ethanol molecule faster than the Mo site resulting in ethanol consumption of 1 > 2. The catalysts without MoO3 consist of acid sites acting as active phase on surface, while, for the Mo-modified catalysts, some acid sites had taken place by MoO<sub>3</sub>. Thus, the surface of catalysts actually contains two types of active phase (acid sites and Mo sites). According to previous study, it suggests that the acid site plays an important role for the dehydration reaction (ethanol to ethylene and diethyl ether). Ethanol was consumed very fast by acid site. In contrast, the Mo sites dominantly acted as the active site for dehydrogenation of ethanol to acetaldehyde. The rate of ethanol consumption was slower than the acid site.

As mentioned above, the ethanol conversion of modified catalyst would be causes from the Mo site. To confirm the rate of ethanol consumption by acid site and Mo site, the turnover frequency (TOF) or turnover number, which describes in the number of molecules reacting per active site per time, was calculated as shown in Table 6.

As seen in Table 6, the TOF of acid site was  $84.4\,\mathrm{s}^{-1}$ . It means that the 84.4 ethanol molecules were converted to ethylene on each acid site per second. However, only  $4.70\times10^{-3}$  molecules of ethanol are converted to acetaldehyde on each Mo site per second. The TOF of acid sites was higher than that of Mo sites. Therefore, when the MoO<sub>3</sub> was added, the acid site and generated new sites (Mo sites) were formed in catalyst. The Mo slowly converted the ethanol molecule resulting in decreasing of overall ethanol consumption.

The selectivity of ethylene, diethyl ether, and acetaldehyde of all catalysts is shown in Figures 9–11, respectively. Both ethylene and diethyl ether selectivity showed the similar trend as seen from M-Al-600 catalysts. Ethylene favors high temperature, whereas diethyl ether requires lower temperature.

 $<sup>^{</sup>m b}$ Based on dehydrogenation reaction of ethanol to acetal dehyde of the 5Mo/M-Al-600 at 200  $^{\circ}$  C.



SCHEME 1: Ethanol consumption phenomena on active site.

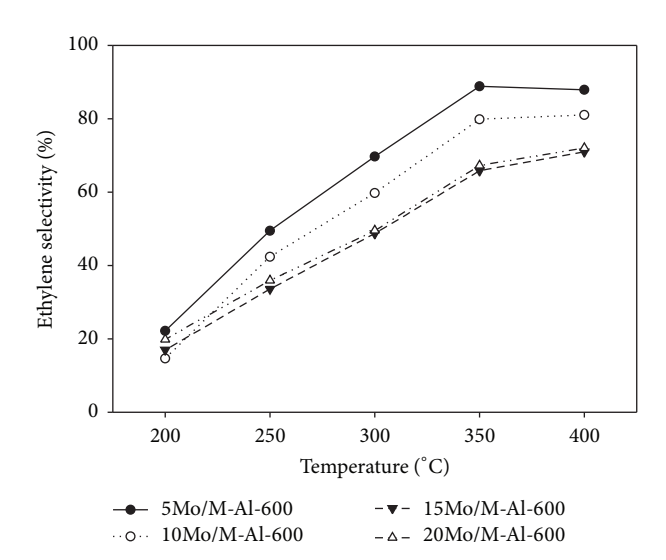


FIGURE 9: Selectivity of ethylene profiles in ethanol dehydration at different temperatures.

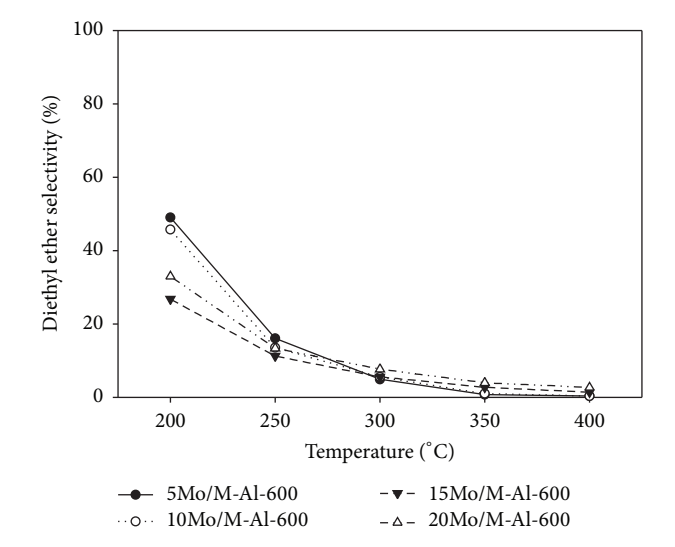


FIGURE 10: Selectivity of diethyl ether profiles in ethanol dehydration at different temperatures.

An enhancement in acetaldehyde selectivity was observed with introduction of MoO<sub>3</sub>. The increase in selectivity of acetaldehyde was due to the fact that Mo species promoted dehydrogenation pathway. The MoO<sub>3</sub> added into the mixed phase alumina substituted the acid sites on catalyst surface, resulting in formation of new sites. This result is corresponding to the NH<sub>3</sub>-TPD data, which explained that the acidity on surface of catalysts consists of two types (conventional acid sites and new sites from Mo species). Ethylene and diethyl ether were produced from the conventional acid sites on catalyst surface, whereas the acetaldehyde results from dehydrogenation reaction generated from Mo species.

The selectivity of ethylene was decreased with an increase of Mo loading as shown in Figure 9. In contrast, the selectivity of acetaldehyde was increased with an increase of Mo loading as shown in Figure 10. Although the 20Mo/M-Al-600 exhibits higher amount of the MoO<sub>3</sub> than the 15Mo/M-Al-600, the selectivity of ethylene is not the lowest or the selectivity of acetaldehyde is not the highest. This was due to the fact that accumulation in catalyst pores was observed when Mo loading is more than 15 wt%. Thus, it leads to loss of Mo species. For the selectivity of ethylene, the 5Mo/M-Al-600 exhibited the highest ethylene selectivity (88.85% selectivity of ethylene at 350°C). However, it was lower compared to

the M-Al-600 (98.76% selectivity of ethylene at 350°C). The 15Mo/M-Al-600 had the highest selectivity of acetaldehyde and the selectivity of acetaldehyde was enhanced up to 56.35% at 200°C. In order to compare the catalyst performance in this study with other researches, the ethanol conversion and ethylene yield of various catalysts are summarized in Table 7. It was found that the mixed phase alumina (M-Al-600) is quite competitive among other catalysts and promising for further study in ethanol dehydration to ethylene.

#### 4. Conclusion

It reveals that the calcination temperature has significant effect on acidity of alumina catalysts. The acidity was decreased with increasing calcination temperature especially for medium to strong acid. Moreover, at  $1000^{\circ}$ C, the mixed  $\gamma$ - and  $\chi$ -crystalline phase alumina catalysts exhibited significant phase transformation.  $\gamma$ -phase was transformed, while  $\chi$ -phase remains stable. In the ethanol conversion reaction, both ethanol conversion and ethylene selectivity depend on medium to strong acid. In this study, the mixed  $\gamma$ - and  $\chi$ -crystalline phase alumina catalyst, which was calcined at  $600^{\circ}$ C (M-Al-600), exhibited the highest catalytic activity. It shows the highest ethylene yield of 98.75% at  $350^{\circ}$ C. In

Catalyst	Reaction temperature (°C)	Ethanol conversion (%)	Ethylene yield (%)	Ref.
M-Al-600	350	99.98	98.75	This work
5Mo/M-Al-600	300	97.64	86.75	This work
$Fe/Al_2O_3$	350	75.2	34.29	[9]
$Fe_2O_3$	350	82.18	28.76	[10]
$Mn_2O_3$	350	68.16	15.00	[10]
$Fe_2O_3/Mn_2O_3$ (1:1)	350	76.00	30.40	[10]
TiO <sub>2</sub> /γ-Al <sub>2</sub> O <sub>3</sub> (microreactor)	360-550	95-99.96	91-99.30	[11]
$SiO_2$	350	2.5	0.89	[23]
${\rm MgO\text{-}Al_2O_3}$	350	11.2	4.62	[23]
$ZrO_2$	350	45.4	36.00	[23]
${ m TiO_2}$	350	80.1	11.29	[23]
Commercial Al <sub>2</sub> O <sub>2</sub>	450	85	66.90	[24]

Table 7: Comparison of catalytic activity of various catalysts for ethanol dehydration to ethylene.

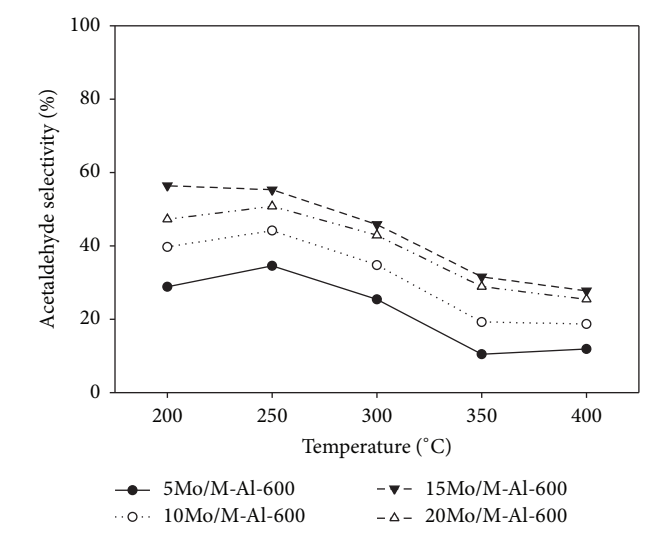


FIGURE 11: Selectivity of acetaldehyde profiles in ethanol dehydration at different temperatures.

addition, with Mo modification, it was found that enhancement of acetaldehyde was observed. However, it is proposed that the active site to produce acetaldehyde was much lower compared with those to produce ethylene.

#### **Competing Interests**

8

The authors declare that there is no conflict of interests regarding the publication of this paper.

# Acknowledgments

The authors thank the Thailand Research Fund (BRG5780009 and IRG5780014) and Grant for International Research Integration: Chula Research Scholar, Ratchadaphiseksompot Endowment Fund, for financial support of this project.

#### References

- [1] J. P. Bortolozzi, E. D. Banús, N. L. Courtalón, M. A. Ulla, V. G. Milt, and E. E. Miró, "Flexible NiZr-based structured catalysts for ethylene production through ODH of ethane: catalytic performance enhancement," *Catalysis Today*, vol. 273, pp. 252–258, 2015.
- [2] J. Bedia, R. Barrionuevo, J. Rodríguez-Mirasol, and T. Cordero, "Ethanol dehydration to ethylene on acid carbon catalysts," *Applied Catalysis B: Environmental*, vol. 103, no. 3-4, pp. 302–310, 2011.
- [3] R. A. Zotov, V. V. Molchanov, A. M. Volodin, and A. F. Bedilo, "Characterization of the active sites on the surface of Al2O3 ethanol dehydration catalysts by EPR using spin probes," *Journal of Catalysis*, vol. 278, no. 1, pp. 71–77, 2011.
- [4] D. Fan, D.-J. Dai, and H.-S. Wu, "Ethylene formation by catalytic dehydration of ethanol with industrial considerations," *Materials*, vol. 6, no. 1, pp. 101–115, 2013.
- [5] M. Zhang and Y. Yu, "Dehydration of ethanol to ethylene," Industrial & Engineering Chemistry Research, vol. 52, no. 28, pp. 9505–9514, 2013.
- [6] A. Takahashi, W. Xia, I. Nakamura, H. Shimada, and T. Fujitani, "Effects of added phosphorus on conversion of ethanol to propylene over ZSM-5 catalysts," *Applied Catalysis A: General*, vol. 423-424, pp. 162–167, 2012.
- [7] J. Lu, Y. Liu, and N. Li, "Fe-modified HZSM-5 catalysts for ethanol conversion into light olefins," *Journal of Natural Gas Chemistry*, vol. 20, no. 4, pp. 423–427, 2011.
- [8] J. Ouyang, F. Kong, G. Su, Y. Hu, and Q. Song, "Catalytic conversion of bio-ethanol to ethylene over La-modified HZSM-5 catalysts in a bioreactor," *Catalysis Letters*, vol. 132, no. 1-2, pp. 64–74, 2009.
- [9] M. Wannaborworn, P. Praserthdam, and B. Jongsomjit, "A comparative study of solvothermal and sol-gel-derived nanocrystalline alumina catalysts for ethanol dehydration," *Journal of Nanomaterials*, vol. 2015, Article ID 519425, 11 pages, 2015.
- [10] T. Zaki, "Catalytic dehydration of ethanol using transition metal oxide catalysts," *Journal of Colloid and Interface Science*, vol. 284, no. 2, pp. 606–613, 2005.
- [11] G. Chen, S. Li, F. Jiao, and Q. Yuan, "Catalytic dehydration of bioethanol to ethylene over TiO2/γ-Al2O3 catalysts in microchannel reactors," *Catalysis Today*, vol. 125, no. 1-2, pp. 111– 119, 2007.

[12] J. Khom-in, P. Praserthdam, J. Panpranot, and O. Mekasuwandumrong, "Dehydration of methanol to dimethyl ether over nanocrystalline Al2O3 with mixed  $\gamma$ - and  $\chi$ -crystalline phases," *Catalysis Communications*, vol. 9, no. 10, pp. 1955–1958, 2008.

- [13] K. Pansanga, J. Panpranot, O. Mekasuwandumrong, C. Satayaprasert, J. G. Goodwin, and P. Praserthdam, "Effect of mixed γ- and χ-crystalline phases in nanocrystalline Al<sub>2</sub>O<sub>3</sub> on the dispersion of cobalt on Al<sub>2</sub>O<sub>3</sub>," *Catalysis Communications*, vol. 9, no. 2, pp. 207–212, 2008.
- [14] C. Meephoka, C. Chaisuk, P. Samparnpiboon, and P. Praserth-dam, "Effect of phase composition between nano γ- and χ-Al2O3 on Pt/Al2O3 catalyst in CO oxidation," *Catalysis Communications*, vol. 9, no. 4, pp. 546–550, 2008.
- [15] J. Janlamool and B. Jongsomjit, "Oxidative dehydrogenation of ethanol over AgLi-Al<sub>2</sub>O<sub>3</sub> catalysts containing different phases of alumina," *Catalysis Communications*, vol. 70, pp. 49–52, 2015.
- [16] T. J. Webster, E. L. Hellenmeyer, and R. L. Price, "Increased osteoblast functions on theta+delta nanofiber alumina," *Biomaterials*, vol. 26, no. 9, pp. 953–960, 2005.
- [17] F. F. Madeira, N. S. Gnep, P. Magnoux, S. Maury, and N. Cadran, "Ethanol transformation over HFAU, HBEA and HMFI zeolites presenting similar Brønsted acidity," *Applied Catalysis A: General*, vol. 367, no. 1-2, pp. 39–46, 2009.
- [18] F. Y. A. El Kady, S. A. Shaban, and A. O. Abo El Naga, "Catalytic dehydrogenation of cyclohexene over MoO3/γ- Al2O3 catalysts," *Transition Metal Chemistry*, vol. 36, no. 2, pp. 237–244, 2011.
- [19] E. Heracleous, A. A. Lemonidou, and J. A. Lercher, "Mechanistic features of the ethane oxidative dehydrogenation by in situ FTIR spectroscopy over a MoO<sub>3</sub>/Al<sub>2</sub>O<sub>3</sub> catalyst," *Applied Catalysis A: General*, vol. 264, no. 1, pp. 73–80, 2004.
- [20] Y. Han, C. Lu, D. Xu, Y. Zhang, Y. Hu, and H. Huang, "Molybdenum oxide modified HZSM-5 catalyst: surface acidity and catalytic performance for the dehydration of aqueous ethanol," *Applied Catalysis A: General*, vol. 396, no. 1-2, pp. 8– 13, 2011.
- [21] E. Heracleous, A. F. Lee, I. A. Vasalos, and A. A. Lemonidou, "Surface properties and reactivity of Al<sub>2</sub>O<sub>3</sub>-supported MoO<sub>3</sub> catalysts in ethane oxidative dehydrogenation," *Catalysis Letters*, vol. 88, no. 1, pp. 47–53, 2003.
- [22] F. E. Kiviat and L. Petrakis, "Surface acidity of transition metal modified aluminas. Infrared and nuclear magnetic resonance investigation of adsorbed pyridine," *The Journal of Physical Chemistry*, vol. 77, no. 10, pp. 1232–1239, 1973.
- [23] T. K. Phung, L. P. Hernández, and G. Busca, "Conversion of ethanol over transition metal oxide catalysts: effect of tungsta addition on catalytic behaviour of titania and zirconia," *Applied Catalysis A: General*, vol. 489, pp. 180–187, 2015.
- [24] X. Zhang, R. Wang, X. Yang, and F. Zhang, "Comparison of four catalysts in the catalytic dehydration of ethanol to ethylene," *Microporous and Mesoporous Materials*, vol. 116, no. 1–3, pp. 210–215, 2008.

















Submit your manuscripts at https://www.hindawi.com

